20000728018   ARO 17039.1-A-EL

FINAL REPORT
PROJECT NO. A-2516

AD A105893

CHAFF THEORETICAL/ANALYTICAL CHARACTERIZATION
AND VALIDATION PROGRAM

By

E. F. Knott, D. J. Lewinski and S. D. Hunt

Prepared for

U. S. ARMY RESEARCH OFFICE
P. O. BOX 12211
RESEARCH TRIANGLE PARK, NORTH CAROLINA 27709

Under

Contract No. DAAG29-80-C-0009

DTIC
ELECTE
OCT 21 1981
D

30 September 1981

GEORGIA INSTITUTE OF TECHNOLOGY

A Unit of the University System of Georgia
Engineering Experiment Station
Atlanta, Georgia 30332

10 10 19

REPORT DOCUMENTATION PAGE		READ INSTRUCTIONS BEFORE COMPLETING FORM
1. REPORT NUMBER	2. GOVT ACCESSION NO. AD-A105 893	3. RECIPIENT'S CATALOG NUMBER
4. TITLE (and Subtitle) CHAFF THEORETICAL/ANALYTICAL CHARACTERIZATION VALIDATION PROGRAM		5. TYPE OF REPORT & PERIOD COVERED Final Report
		6. PERFORMING ORG. REPORT NUMBER
7. AUTHOR(s) E. F. Knott, D. J. Lewinski, and S. D. Hunt		8. CONTRACT OR GRANT NUMBER(s) DAAG29-80-C-0009
9. PERFORMING ORGANIZATION NAME AND ADDRESS Engineering Experiment Station Georgia Institute of Technology Atlanta, Georgia 30332		10. PROGRAM ELEMENT, PROJECT, TASK AREA & WORK UNIT NUMBERS
11. CONTROLLING OFFICE NAME AND ADDRESS U.S. Army Research Office P.O. Box 12211 Research Triangle Park, N.C.		12. REPORT DATE September 1981
		13. NUMBER OF PAGES 113 + v
14. MONITORING AGENCY NAME & ADDRESS(If different from Controlling Office)		15. SECURITY CLASS. (of this report) UNCLASSIFIED
		15a. DECLASSIFICATION/DOWNGRADING SCHEDULE

16. DISTRIBUTION STATEMENT (of this Report)

Approved for public release; distribution unlimited.

17. DISTRIBUTION STATEMENT (of the abstract entered in Block 20, if different from Report)

18. SUPPLEMENTARY NOTES

THE VIEW, OPINIONS, AND/OR FINDINGS CONTAINED IN THIS REPORT ARE THOSE OF THE AUTHOR(S) AND SHOULD NOT BE CONSTRUED AS AN OFFICIAL DEPARTMENT OF THE ARMY POSITION, POLICY, OR DECISION, UNLESS SO DESIGNATED BY OTHER DOCUMENTATION.

19. KEY WORDS (Continue on reverse side if necessary and identify by block number)

20. ABSTRACT (Continue on reverse side if necessary and identify by block number)

This report describes the modeling of radar returns from chaff. The dipoles are allowed to follow helical paths as they fall, and the signal scintillation characteristics of the entire chaff cloud are assumed to be the same as those of a small collection of up to 1000 dipoles. The dipole motion model is based upon the solution of the aerodynamic force equations over small time intervals. The scintillation signal is normalized with respect to the contribution of a single dipole.

DD FORM 1 JAN 73 1473 EDITION OF 1 NOV 65 IS OBSOLETE

The mean amplitude of the return from the entire cloud is computed assuming a bivariate Gaussian distribution for the dipole number density in a plane transverse to the axis of a plume of chaff. The computation of the amplitude requires a numerical integration of the product of the radar antenna radiation pattern and the dipole density in a spherical shell centered on the radar. When this is done for several concentric shells, the range dependence of the return can be displayed. The antenna need not be pointed at the cloud.

Unfortunately, the numerical integration consumes large blocks of CPU time and the program was used to study a limited sample of test dipoles. The bandwidth of the signal received from collections of 16 to 1024 dipoles was less than 150 Hz and was essentially independent of the number of dipoles. It is, in fact, the dipole motion characteristics, and not the dipole spacing, that influences the signal bandwidth. Local wind turbulence will expand the spectrum somewhat.

Because of the long running time, adequate running time needs to be allocated for the evaluation of tactical situations. The program is useful for diagnostic applications but future efforts need to be given to improving the dipole concentration description: Empirical descriptions could be devised if adequate measurement data were available.

FINAL REPORT

GIT/EES PROJECT A-2516

CHAFF THEORETICAL/ANALYTICAL CHARACTERIZATION
AND VALIDATION PROGRAM

By

E. F. KNOTT, D. J. LEWINSKI AND S. D. HUNT

CONTRACT NO. DAAG29-80-C-0009

Submitted to

U. S. Army Research Office
P.O. Box 12211
Research Triangle Park, North Carolina 27709

September 1981

GEORGIA INSTITUTE OF TECHNOLOGY
Engineering Experiment Station
Atlanta, Georgia 30332

TABLE OF CONTENTS

LIST OF FIGURES

LIST OF TABLES

SECTION 1
INTRODUCTION

This report covers the period 1 November 1979 through 31 July 1981 and describes Georgia Tech's approach to the construction of a chaff model. That approach, which is described in the next section, was ambitious because the intent was to trace the detailed aerodynamic and electromagnetic behavior of the chaff dipoles and, at the same time, to model the propagation of received signals through a radar system. Some of the goals were achieved and some were not.

The objective was to devise a tool that could be used to evaluate the effectiveness of chaff in a variety of situations. Unfortunately, "effectiveness" has nearly as many meanings as there are individuals working in chaff concepts: some people are interested in chaff performance only for the first few seconds after dispersal, some are concerned with tracking errors due to chaff and others are interested only in the near field fuzing problem. Many of the agencies involved have developed chaff models to suit their own evaluation requirements, hence it is perhaps not unexpected that the generation of yet another model raises the question if duplication has occurred.

Duplication in some areas cannot be avoided, but in the main, where previous work has been identified, Georgia Tech drew upon it. In the Georgia Tech model, for example, the scattering patterns of dipoles of arbitrary length are computed using the numerical scheme devised by Kuo and Strait at Syracuse University [1]. Most chaff packages, even roll chaff, contain from four to seven different dipole lengths and we sought to account for the distribution in length. As far as can be determined, there are no chaff models that include this degree of detail. Another sophistication in the model is the weighting of the chaff returns

according to the angular location of the dipoles within the antenna radiation pattern, another detail not often accounted for in chaff models.

This report covers the first two phases of a four-phase effort. The proposed phases were:

Phase I: Initial Chaff Model Development
Phase II: Data Analysis
Phase III: Collection of Data (Measurements),
             Upgrading and Validation of the Chaff
             Model
Phase IV: Development and Integration of a Complete
             Systems Model

The data analysis implied in Phase II was for the purpose of establishing dipole density distributions within a chaff cloud, which presupposes that such data already existed. Unfortunately, the only data that were available were for a test run for which cloud mapping was not the primary objective of the test. Other data were desired to verify the power spectral signatures of chaff, but these were not available.

As a result of some of the studies conducted in Phase I, Georgia Tech determined the characteristics of an instrumentation system that could acquire the desired information. The radar should be a coherent, multiple polarization, scanning system. The coherence would yield information about the spectrum of the received signals, the polarization capability would help verify dipole orientation distributions, and the scanning capability could be used to assess volume distributions. It is not known if such a system has been employed for chaff evaluation; to the best of our knowledge, it has not.

Phases III and IV have not been funded and are not discussed in this report, but Georgia Tech has proposed further integration of the efforts of others into the chaff model for Phase III. Specifically, the dispersal model worked out by Traci, et al., [2] was suggested as a means for describing the space/time

2

history of dipole volume density distributions, and the radar model devised by Bogusch, et al., [3] was suggested as a means for tracing the received signals thorugh a generic radar receiver.

Georgia Tech's approach to the problem was to develop a quasi-deterministic description. Since it is impossible to trace the motion history and, consequently, the time-varying radar return of a million or more dipoles, we dealt with a smaller number. This was done deterministically using the aerodynamic properties reported by Brunk, et al. [4]. It was assumed that the signature characteristics of elemental volumes of the cloud matched those of a finite collection, and we thus invoked sampling theory. The returns were normalized with respect to the number of dipoles in the finite collection, making it possible to assign an amplitude to any volume within the cloud, providing the number density of that volume is known.

A subroutine was developed to account for the spatial dispersion of a collection of falling dipoles and, when used in conjunction with the electromagnetic scattering properties of dipoles mentioned above, it was possible to compute the composite return from the dipoles. This is because the complex return of each dipole and the relative phase due to its position in space was included. The exercising of this part of the program with progressively more dipoles in the sample collection suggested that it is not the number nor the density of the dipoles that influences the scintillation of the return, but the dipole motion itself.

The plan was then to estimate the dipole density function in the cloud and to weight the net return from an elemental volume according to the dipole number density and the position of the elemental volume within the antenna radiation pattern. At first it was asumed that the dipole number density followed a trivariate Gaussian distribution (as might be representative of a single "puff" of chaff), but the integral could not be evaluated

3

analytically. The decision to resort to a numerical integration scheme produced a subroutine that is impractical because of the time required to count dipoles.

Consequently, the model is incomplete. An attempt was made in Phase II of the effort to fit bivariate Gaussian functions in the transverse plane to experimental data, but the data proved insufficient for this purpose. If future work is conducted using this approach, it will be necessary to have better measurement data or to use procedures such as those reported by Traci, et al., to generate the volumetric dipole number density distributions within a chaff cloud.

Furthermore, our work shows that numerical volume integration is very time consuming on a computer, as is the tracing of the motion history of all but a small handful of individual dipoles. Future efforts should be devoted to approximations of the volume integral and the development of empirical descriptions of the dipole density variation in a chaff cloud. The latter requires more controlled experiments than have been conducted to date.

SECTION 2
MODEL OVERVIEW

Development of a chaff model involves at least four separate kinds of considerations, two of them purely mechanical in nature and two of them electrical. The former seeks to trace the evolution of the chaff cloud and its subsequent motion, while the latter traces the generation, scattering, and reception of radar signals. The four parts of the model should address

1. Dispersal or distribution methods,
2. Cloud dynamics and environmental conditions,
3. Particle and aggregate scattering characteristics,
4. Victim radar characteristics.

The importance of each part of the model may be illustrated by working backward through the list, commencing with the characteristics of the victim radar. The signal output from the receiver may be a visual display, or it may drive a processor which delivers commands to a control system. This signal, along with its effect on an operator or a control system, ultimately forms the basis of a performance evaluation. The signal characteristics depend on the receiver input signal, receiver characteristics (such as gain, bandwidth, and noise figure), and any signal conditioning or signal processing that is performed.

The receiver input signal arises from returns due to clutter, multipath, desired and undesired targets, and the chaff cloud itself. The relative strengths of these returns depend on the radar scattering characteristics of each source of return and in which parts of the antenna pattern they may be found. Clutter signals are due to direct terrain reflections that occur at the same effective range as the target, and multipath signals are due to indirect reflections from the terrain between the target and

radar. Multipath returns are common when the target is at low altitudes and clutter returns may become significant in the presence of ground vegetation viewed at nongrazing angles of incidence.

The return from the chaff cloud depends on how much of the cloud lies in the antenna main beam, and, of course, even the signal received via the sidelobes can be significant for the large radar cross sections normally presented by chaff. Because the radar waves penetrate the cloud with little attenuation, the dipole density (number per unit volume) and the spatial disposition of the cloud with respect to the radar beam must be known. This implies a knowledge or estimate of the cloud size, shape and position, and the distribution of particles within it. Thus, the effect of the environment on the cloud particles should be estimated.

The orientation of the dipoles depends on their aerodynamic properties, and the electromagnetic scattering from the cloud is influenced by the orientation and size of the dipoles. As far as can be determined, there is only one study of the motion and orientation history of thin dipoles falling through the air [4]. That study showed that dipoles tend to follow helical paths as they fall and that they tend to maintain the initial angle of attack. It should be noted that the dipoles were dropped individually in still air for that study.

Finally, the growth and evolution of the cloud depend on the initial conditions of dispersal. Several deployment methods can be postulated, ranging from continuous seeding from an aircraft moving at constant velocity at a given altitude to the bursts of several chaff munitions cannisters launched from the ground. The dipole density distribution within the cloud obviously varies with time and with the method of dispersal, and the fall rate and cloud drift depend on local wind and turbulence conditions.

Thus it can be seen that several mechanical and electrical processes must be analyzed, and the approach proposed by Georgia

Tech was to develop a modular program. The modular approach allows various portions of the model to be changed as the need arises without disturbing the remaining portions of the model. This also makes it possible to introduce or to "inject" test parameters directly into the program for testing and debugging purposes, and permit parallel (simultaneous) development of the modules.

The conceptual form of the chaff model is shown in Figure 1, where it is assumed that all pertinent input parameters have been delivered to the program and have been appropriately stored. The main flow of computation is downward through the center of the diagram, with inputs called from either side of the diagram as needed. Note that environmental parameters are called early in the computations to establish the statistics of chaff cloud growth and motion, and that certain particle dipole factors are called at one stage while others are called later. Certain victim radar characteristics are similarly required for the scattering computations while others are needed later to calculate the effect of signal processing at the output stage. The final module in the diagram computes the action of any servo loops in the radar and simulates the information normally displayed by the radar to an operator.

For the initial development of the chaff model, it was felt that clutter and multipath effects were small enough to be neglected. This is typically the case for a ground-based radar whose antenna is pointed a few degrees or more above the horizon. If it later turns out that clutter and multipath effects are significant, these can be embedded in modules that feed the scattering module near the center of the diagram of Figure 1. Similarly, if it appears useful to add (nonchaff) radar target returns, a target module may be developed and added to the model. However, it is felt that these were ancillary to the main effort of the initial model development.
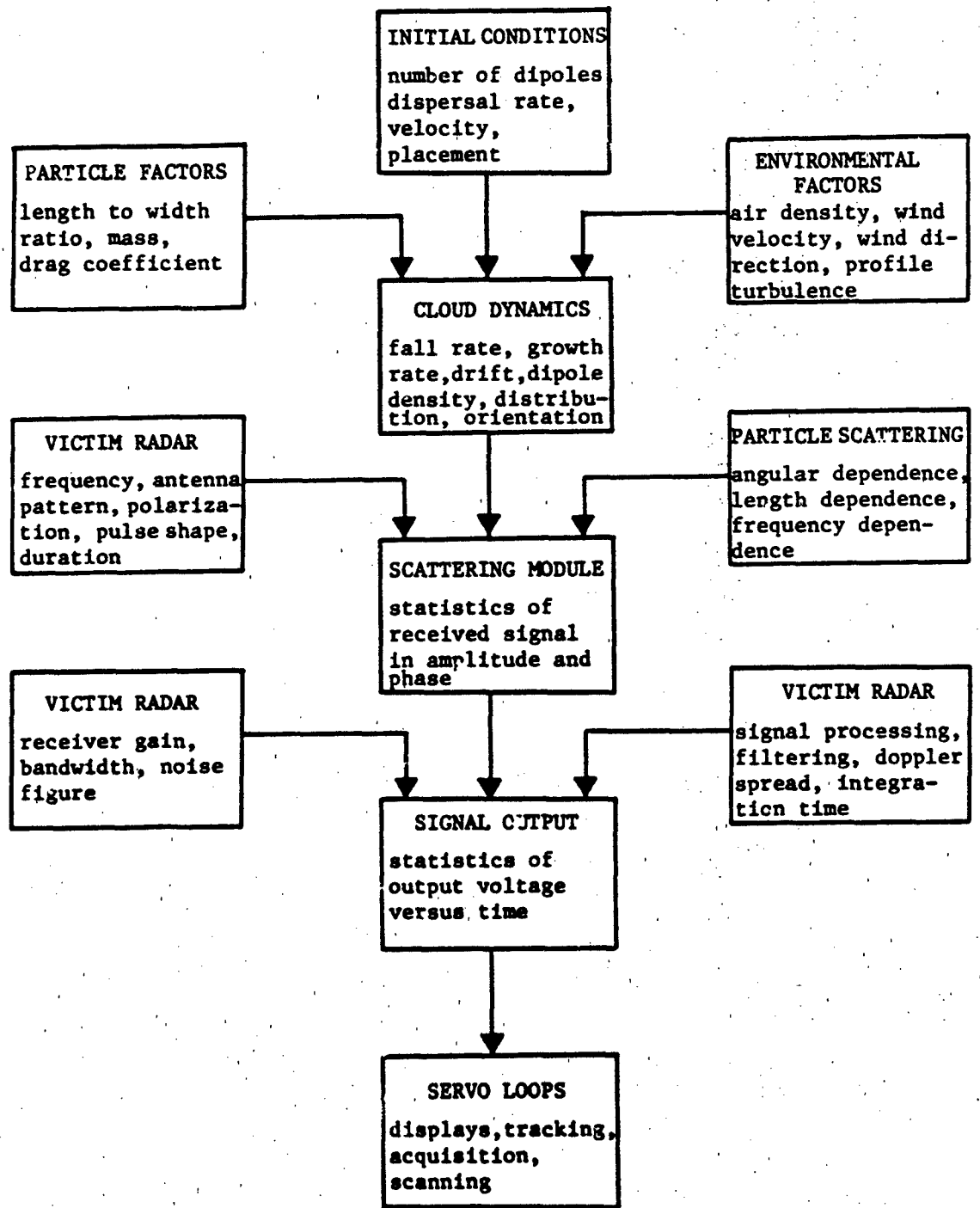
Figure 1. Conceptual form of the complete chaff model.

For the purposes of initial model development, not all the features displayed in Figure 1 were included. For example, dispersal was assumed to be the default case of corridor chaff, and chaff puffs per se were not included. Although some work was undertaken on the characteristics of four classes of radar (see Section 7), the radar receiver characteristics remain to be modeled.

The configuration of the initial model is shown in Figure 2. The input to the radar receiver consists of a mean signal amplitude and a normalized time signature which, when combined, describe the instantaneous complex signal in time. The mean signal amplitude was to be generated by an integration routine which evaluates the returns from dipoles in a thin spherical shell at constant range from the radar.

These returns involve the product of the antenna radiation pattern in space and the dipole density distribution within the cloud, and we sought to accommodate the general case in which the antenna is not necessarily pointed directly at the cloud. Unfortunately, this portion of the program was not completed before the end of the contract had been reached. The output from the integration scheme was to have been the mean signal amplitude for each of several contiguous range bins, much as is recorded during chaff tests conducted by Office of Missile Electronic Warfare Systems (OMEWS) and other agencies.

The dipole motion model shown at the left side of Figure 2 was developed on the basis of the study by Brunk, et al. [4], and it includes a turbulence model and a steady wind drift component. The motion model is based on an approximate solution of the aerodynamic forces on a slender fiber and it commences with the generation of initial positions and orientations of a collection of a finite number of dipoles. The change in position and orientation of each dipole over a small interval of time is computed under the assumptions that the air density, projected area of the dipole and the aerodynamic drag force remain constant

9
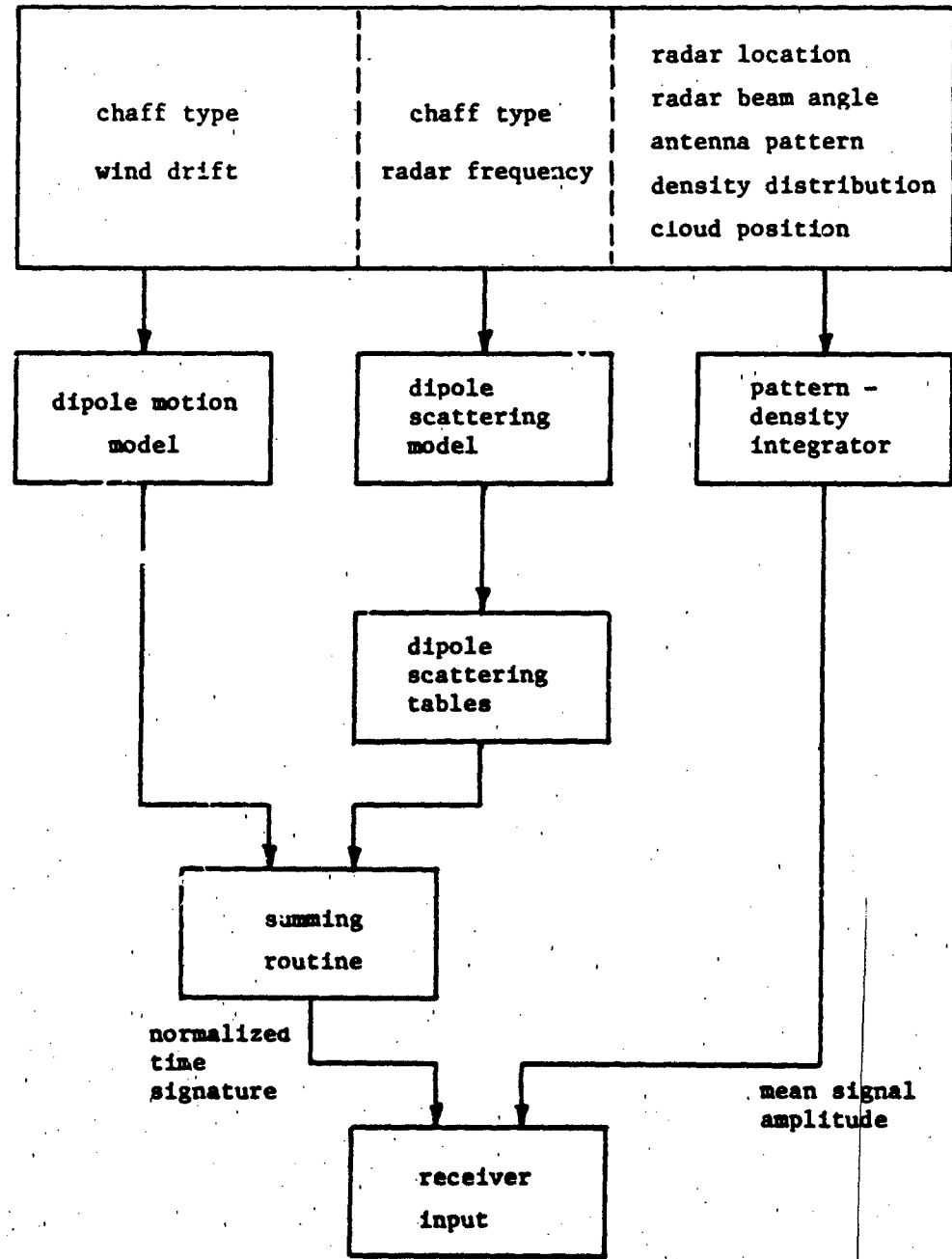
Figure 2. Initial chaff model.

over the time interval. It turns out that the time interval must be less than about 10 ms in order for the approximations to hold, hence it would require many small increments to index time for a complete cloud duration of 30 minutes. For this reason, time signatures only 60 seconds long are generated by the subroutine. The dipole positions and orientations are updated on the basis of the small changes during the interval.

The dipole scattering model makes use of the exact solution for the currents induced along the dipole by the incident wave. The numerical procedure is known as the method of moments, and the subroutine is largely a modification of a program devised elsewhere [1]. The subroutine generates the complex scattering pattern (i.e., phase and amplitude) of a dipole of given electrical length and stores the pattern in tabular form. This is performed for each dipole length (not each dipole) in a given chaff package and needs to be done only once for each length. Whenever the scattering amplitude is needed by other subroutines, a value is extracted from the table using a linear interpolation scheme.

Since the return from a collection of dipoles is the coherent sum of individual contributions, the motion model is used in conjunction with the tables produced by the electromagnetic scattering model. The summation of the individual returns generates a normalized time signature which can be transformed to the time domain if desired. Indeed, this transformation was envisioned to be used in modeling the radar receiver and the processing that takes place there, but as with the volume integration module, this portion of the model was not completed. Section 7 outlines the kinds of signal processing that takes place in four different kinds of radar systems.

SECTION 3
ELECTROMAGNETIC MODEL

In addition to a dozen or more different chaff designs in the U.S. Army inventory, there may be experimental designs that need to be evaluated. Hence it was necessary to develop a way to compute the return from a dipole of arbitrary length at an arbitrary frequency. The return from a single dipole depends only on the orientation of the dipole with respect to (a) the incident electric polarization and (b) the aspect angle. The return from many dipoles depends on the spacing between dipoles as well as upon the orientation. These features are included in the program modules as described in the following sub-sections.

3.1   SCATTERING FROM A SINGLE DIPOLE

As can be seen from Table 1, most chaff loads contain more than one length of dipole, and since the radar frequency is allowed to be arbitrary, we must have a way of calculating the scattering pattern of a dipole of arbitrary length. To do so, we used a program developed at Syracuse University [1]. The program was modified slightly to suit our particular requirements; although the user must be aware of an error in the original program [5], the error had no impact on our own application.

The program makes use of the method of moments, whose principal exponent was Harrington [6]. The basic approach is to write the integral equation for the currents induced on a wire of finite length and to reduce the equation to a system of homogeneous linear equations. It is assumed that the wire is small enough that there are no significant circumferential currents, implying that the wire must be much smaller in diameter than the incident wavelength, typically less than $\lambda/50$. For practical radar frequencies and chaff dipoles, this condition is almost always satisfied.

The excitation of the wire may be due to one or more voltage sources inserted at gaps along the wire, or it may be due

12

TABLE 1. CHAFF LOAD PARAMETERS

Type	Designation	Cut No.	Length, Inches	Number, Millions
Cartridge	RR-129T/AL	1	2.00	0.75
	RR-144/AL	1	0.66	5.25
	RR-163/AL	1	1.20	0.079
		2	0.60	0.5925
	RR-171/AL Roll 1	1	1.99	0.034
		2	1.12	0.034
		3	0.82	0.102
		4	0.71	0.136
Roll		5	0.61	0.136
	RR-171/AL Roll 2	6	1.74	0.032
		7	1.12	0.032
		8	0.82	0.032
		9	0.45	0.227
		10	0.36	0.390
	RR-125/AL	1	0.75	0.36
		2	0.63	0.72
		3	0.59	0.18
		4	0.56	0.72
		5	0.39	0.36
		6	0.36	0.72
		7	0.31	0.18
	RR-146/AL	1	0.70	2.25
		2	0.60	3.00
		3	0.51	1.50
		4	0.45	2.25
		5	0.39	3.75
	RR-147/AL	1	0.70	1.5
		2	0.64	3.0
Package		3	0.62	4.5
		4	0.59	1.5
	RR-153/AL	1	1.84	1.50
		2	1.61	0.54
		3	1.07	0.75
		4	0.63	1.50
		5	0.55	1.50
	RR-153 A/AL	1	1.84	1.50
		2	1.61	0.75
		3	1.07	0.75
		4	0.63	1.50
		5	0.55	2.25
	RR-178 (XN-2)	1	1.60	0.375
		2	1.34	0.375
		3	0.97	0.750
		4	0.64	0.750
		5	0.54	1.250
		6	0.34	1.500

13

to an incident plane wave. The reduction of the integral equation to a system of homogeneous equations is accomplished by dividing the wire into a collection of subsections. The current supported by any subsection is due to the incident wave as well as to the fields radiated by other subsections of the wire. The problem amounts to determining the current strength on each subsection such that the resulting distribution satisfies the boundary conditions, namely that the current must be continuous and that it vanish at the wire ends.

The solution to the problem obviously requires the computation of a finite collection of matrix elements. These elements are computed (in the Syracuse program) under the assumption that the current distribution along a wire subsection has a triangular shape, rising linearly from zero at either end to a peak at the midpoint. A matrix inversion is required. When the inverted matrix is multiplied by the excitation vector (a column matrix), the current distribution along the complete wire is determined.

The smaller the subsections, the more accurate the solution. For generally acceptable precision, the subsections should be no more than $\lambda/20$ in length, but since the memories of modern computers typically limit the matrix to about 200 x 200 = 40,000 matrix elements at most, wires more than 10λ long cannot be handled accurately.

Once the currents have been computed via the matrix inversion, they can be summed in a "discretized" version of the radiation integral. This yields the far scattered field which, when normalized to the incident field strength, is a direct measure of the radar cross section of the wire.

It is much easier to compute the bistat' field in several directions for a single direction of incidence than it is to compute the backscattered field for several directions of incidence. This is because each new direction of incidence requires a new matrix inversion. In the program implementation of this computation, the lengths of the individual dipole cuts are

14

fetched from a table of chaff information not unlike Table 1. For example, 5 different lengths would be fetched for the RR-146/AL chaff. These are normalized with respect to the incident wavelength, and the modified Syracuse program (which is called SCAT in the Georgia Tech program and is embedded as a subroutine) is called.

Subroutine SCAT computes the backscattering cross section for each dipole length at 91 aspect angles ranging from broadside to end-on (i.e., at one-degree increments) and returns these values to the main program. The main program stores the values in a look-up table acccessed by other subroutines. In the case of RR-146/AL, five such tables would be created and saved.

Figures 3 through 6 are comparisons of the backscattering patterns predicted by SCAT and the measured patterns reported by Chang and Liepa [7]. The computed data are shown as solid lines and the measured data as dashed lines, and the amplitudes are in decibels with respect to a square wavelength. The amplitudes of the broadside and near broadside lobes generally agree within about 1 dB for the shorter dipoles, but this deteriorates to as much as 6 dB for some of the narrow lobes in Figure 6. The locations of the major lobes agree better for the shorter dipoles than for the longer ones; the misalignment between measured and predicted lobe locations ranges from about 3 degrees in Figure 6 to none in Figure 3. The traveling wave lobes (the large ones near the sides of the patterns) seem to be the hardest ones to match with any degree of consistency, being overestimated by about 3 dB in Figure 3 and underestimated by 2 dB to 4 dB in Figures 4 through 6.

The fact that the predicted lobe locations always lie closer toward the center of the pattern than the measured ones suggests one of two possibilities, or perhaps both. For one, the theory may not account for the small but finite charge that accumulates at the wire ends. For another, the dipoles measured by Chang and Liepa may be fatter than those used in the model. In
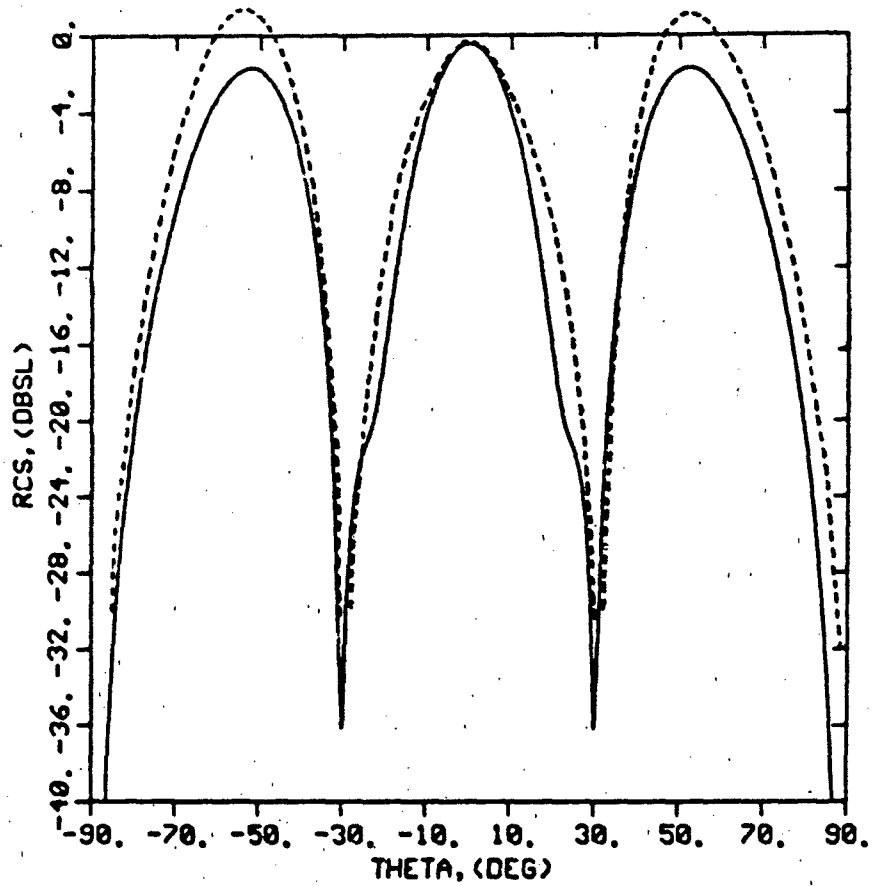
Figure 3. Comparison between predicted and measured
dipole scattering for a dipole 1.857 λ long.
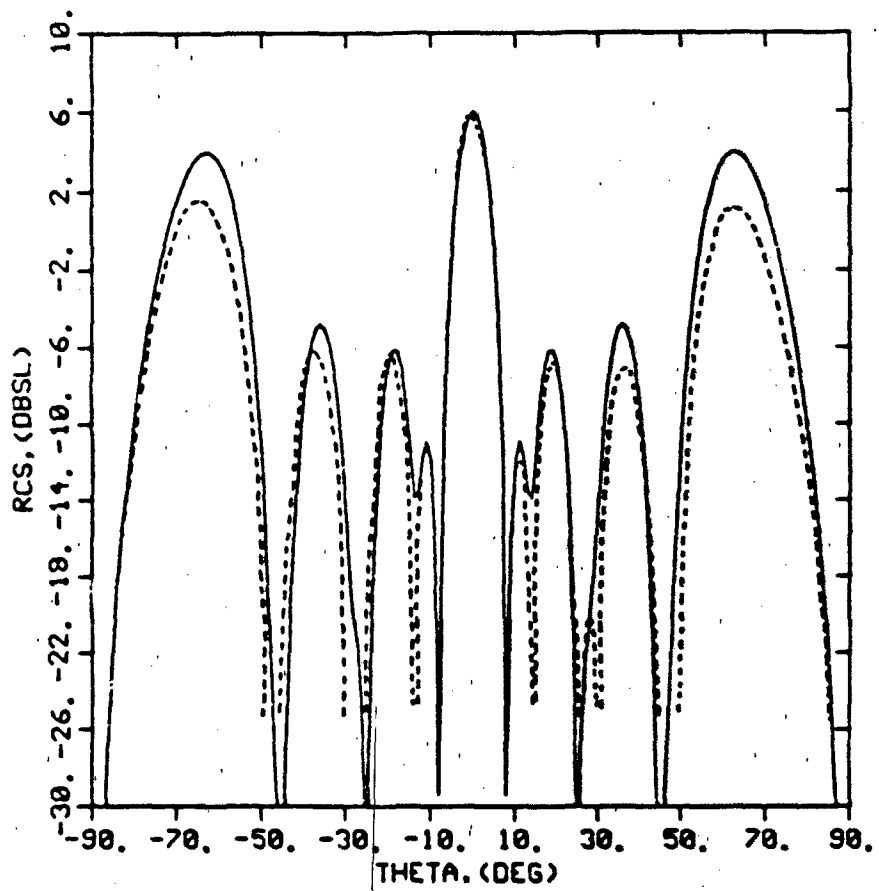
Figure 4. Comparison between predicted and measured
dipole scattering for a dipole 3.614 λ long.

17
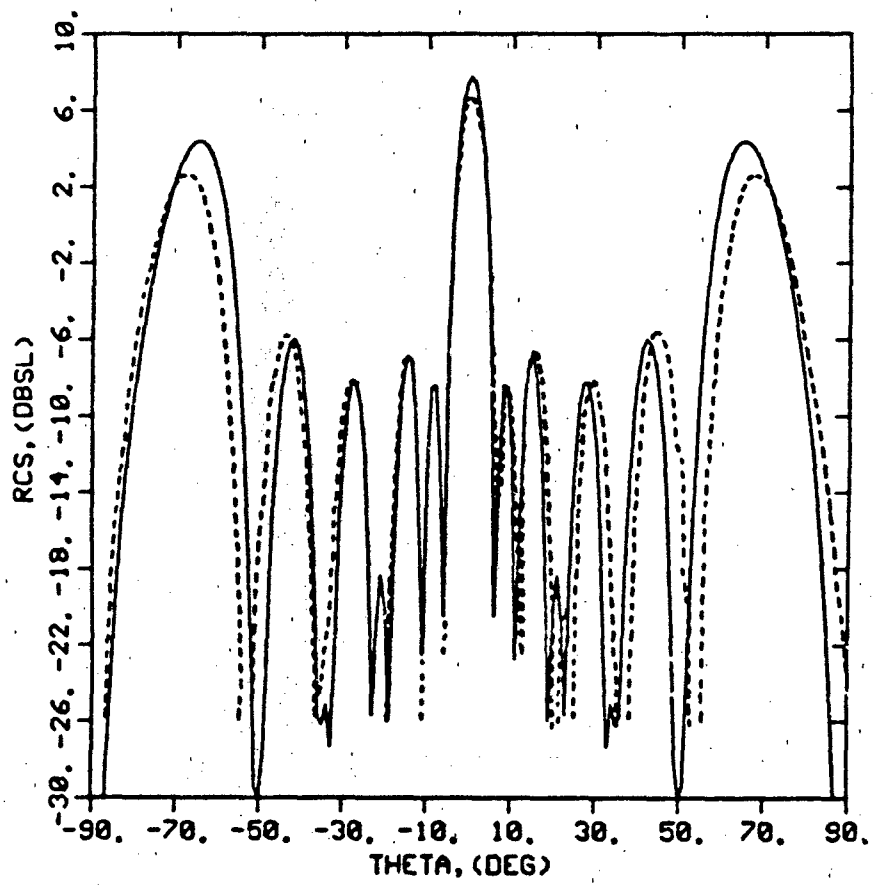
Figure 5. Comparison between predicted and measured
dipole scattering for a dipole 4.87 λ long.
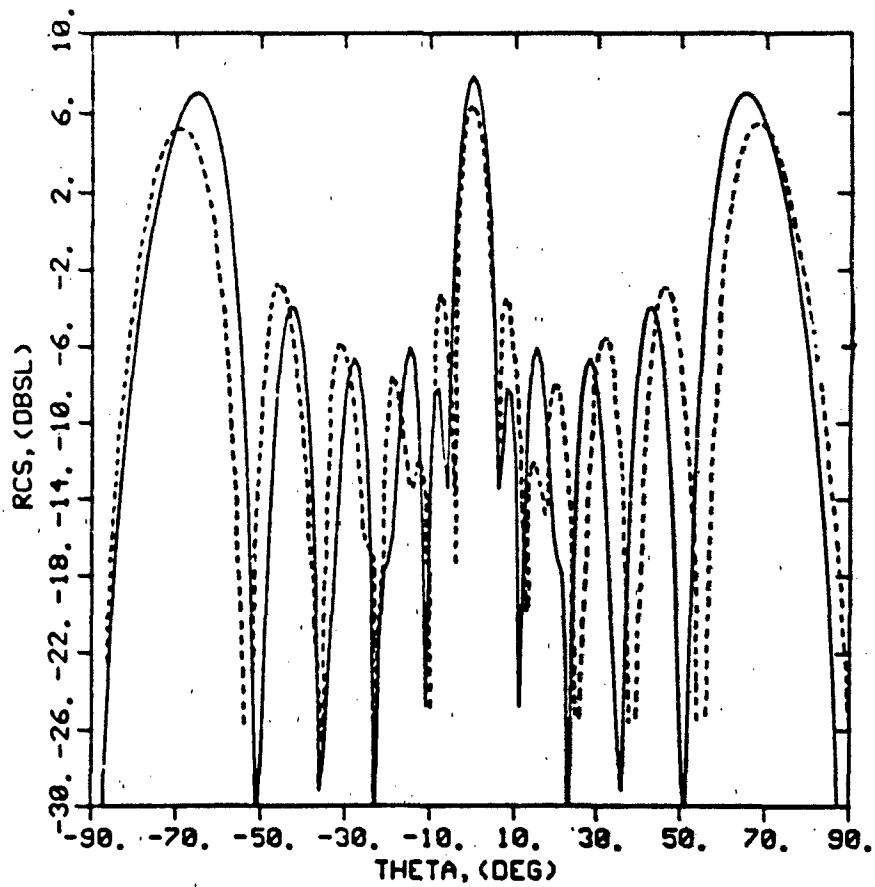
Figure 6. Comparison between predicted and measured
dipole scattering for a dipole 5.02 λ long.

19

any event, the discrepancies between theory and measurement shown in these figures are not considered serious.

3.2   SCINTILLATION CHARACTERISTICS OF MANY DIPOLES

One of the objectives of the model is to simulate the signal scintillation as thousands of dipoles change position with respect to each other. The dominant cause of scintillation is due to the rate of change of dipole position -- not the spacing between the dipoles. In a deterministic synthesis of scintillation, we can use only a small number of dipoles to model a cloud of millions, and the question comes to mind how small a sample is adequate.

In an attempt to answer that question, we conducted a series of simple numerical tests on a finite collection of half-wave dipoles. The dipoles were allowed to fall along helical paths as suggested by the study of Brunk, et al. [4], and the phasor sum of their returns was computed at closely spaced time intervals. This was performed for as few as 8 and as many as 1024 dipoles. The resulting time histories were transformed to the frequency domain so that the power spectral densities could be examined.

The radar cross section of a half-wave dipole can be expressed as [8]

$$\sqrt{\sigma} = \sqrt{\sigma_0} \; (\hat{p} \cdot \hat{e})^2 \tag{1}$$

where, σ_0 = the broadside radar cross section of the dipole, approximately $1.23 \; \lambda^2$,

$\hat{p}$ = unit vector aligned along the dipole axis,

$\hat{e}$ = unit vector aligned along the incident electric vector.

Since there are many dipoles whose returns are to be summed vectorially, we must keep track of their positions. If the distance from the dipole to some origin is $\bar{r}$,

$$\sqrt{\overline{\sigma}} = \sqrt{\overline{\sigma_0}} \ (\hat{p} \cdot \hat{e})^2 \ e^{i2k\overline{r}\cdot\hat{i}} \tag{2}$$

where $\hat{i}$ is a unit vector along the direction of propagation of the incident wave. The time dependent quantities in Equation (2) are the dipole orientation $\hat{p}$ and its position $\overline{r}$.

According to the Brunk team, freely falling dipoles follow spiral trajectories. This was determined from photographic records of more than 300 individual "drops" in a quiescent chamber. The dipoles tend to maintain their initial pitch angle. The parameters of the motion are the spiral rate Ω, the radius of gyration a, the pitch angle γ of the spiral path, and the angle of attack α with respect to the spiral path. Figure 7 illustrates these parameters.

For simplicity, we allow the incident wave to propagate in the direction $\hat{i} = -\hat{x}$ in the coordinate system of Figure 8. Allowing the axis of the helical trajectory to be displaced from the origin, we designate its location by (x_0, y_0). Consequently, the exponent in Equation (2) is

$$-i2k\left[x_0 + a \ \cos(\Lambda + \Omega t)\right]$$

where Λ is the initial angular position around the path. Finally, we assume, as suggested by the Brunk study, that the dipole maintains its initial orientation with respect to the horizontal. Call this angle $\theta = \gamma - \alpha$. Therefore, Equation (2) becomes

$$\sqrt{\overline{\sigma}} = \sqrt{\overline{\sigma_0}} \ \sin^2\theta \ \exp\left\{-i2k\left[x_0 + a \ \cos(\Lambda + \Omega t)\right]\right\} \tag{3}$$

For a collection of dipoles, we used a random number generator to establish the distributions listed in Table 2. Then, using an assumed radar frequency of 10.5 GHz, we computed the return for each dipole using Equation (3) and summed them

21
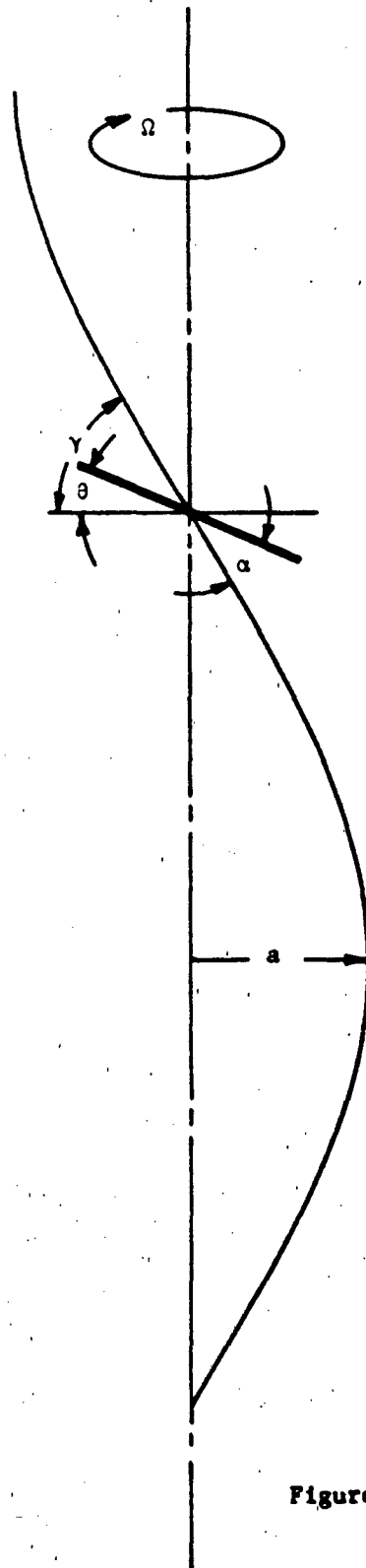
Figure 7. Geometry of the helical path followed by a falling dipole.
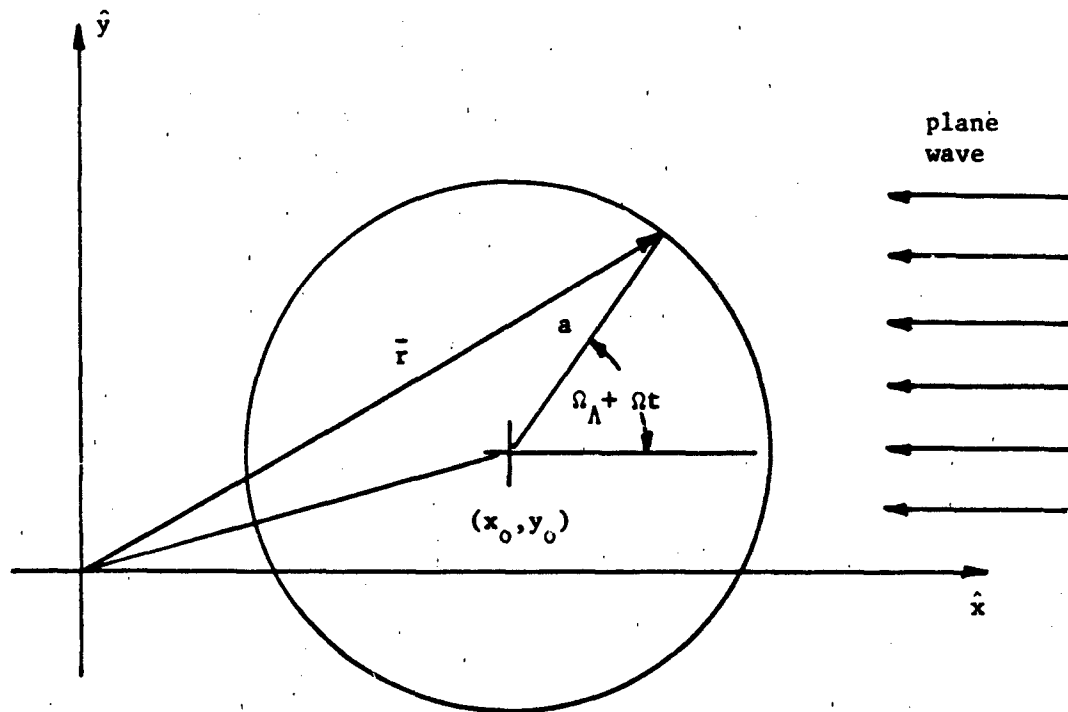
Figure 8.   Geometry of spiral motion.

TABLE 2. STATISTICS OF THE MOTION DISTRIBUTIONS

Variable	Symbol	Distribution	Mean	Standard Deviation	Lower Limit	Upper Limit
initial angle	Ω_o	uniform	--	--	0	--
angular rate	Ω	Gaussian	3 rad/sec	1 rad/sec	--	--
initial angle	θ	Gaussian	1.22 rad	0.175 rad	--	--
radius	a	Gaussian	6"	2"	--	--
initial position	x_o	uniform	--	--	0	200"

vectorially. A selection of time histories and power spectra are displayed in Figures 9 through 15. The amplitudes on these figures are with respect to an arbitrary level, hence absolute values cannot be inferred from them.

Figure 9 shows the phase and amplitude of the return from 20 dipoles computed at 0.5 millisecond intervals. The maximum rate of change of phase is about 60,000 degrees per second, or 167 Hz. The closest spacing between nulls is at the left of the diagram and is about 4 ms, implying that frequencies as high as 250 Hz may be expected in the spectrum.

Figure 10 is the time history for 32 dipoles for a duration of 1 second, a much longer period than for Figure 9. Figure 11 is the power spectrum as obtained from a Fourier transformations of the signal of Figure 10 to the frequency domain. The phase information was retained in performing this transformation and a Hanning weighting function was used. Figure 11 would imply that the highest significant frequency is about 50 Hz, somewhat less than the values deduced from the 20-dipole data in Figure 9.

The time history of the return from 512 dipoles is given in Figure 12; in comparison of this history to the history for 32 dipoles in Figure 10, it is difficult to detect much difference in the scintillation. The power spectrum (Figure 13) is somewhat broader, however, with significant frequencies as high as 75 Hz. The results for 1024 dipoles are shown in Figures 14 and 15; the spectrum is slightly narrower than that of Figure 13.

These comparisons suggest that a small number of dipoles, perhaps as few as 50 or 100, are adequate for modeling the scintillation characteristics of a much larger number of dipoles. There appears to be a slight trend toward greater bandwidths for greater numbers of dipoles, but this trend is weak at best. For a radar frequency of 10.5 GHz, the maximum signal bandwidth appears to be about 150 Hz (from -75 Hz to +75 Hz).

Figure 9. Amplitude and phase of the return from 20 dipoles.

NUMBER OF DIPOLES: 20
WAVELENGTH,(INCHES): 1.125
T-ZERO,(MSEC): 100000.0

NUMBER OF DIPOLES: 32
WAVELENGTH, (INCHES): 1.125
T-ZERO, (MSEC): 100000.0
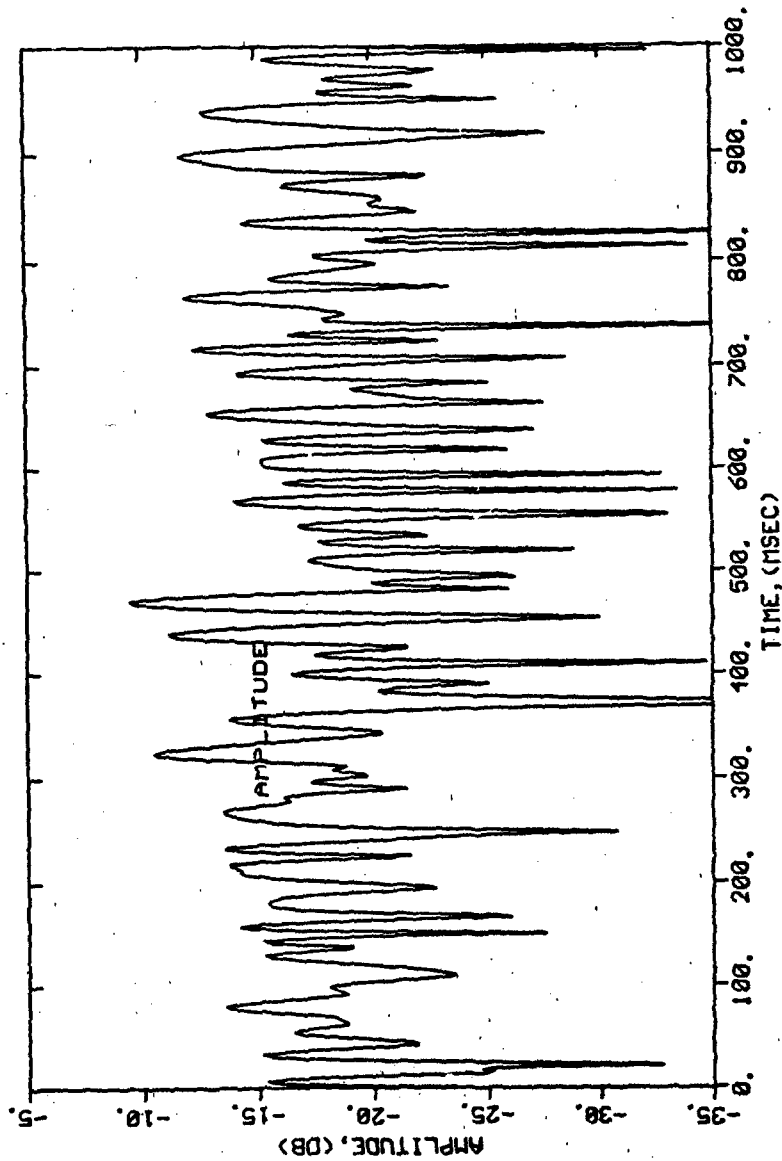
Figure 10. Amplitude of the return from 32 dipoles.
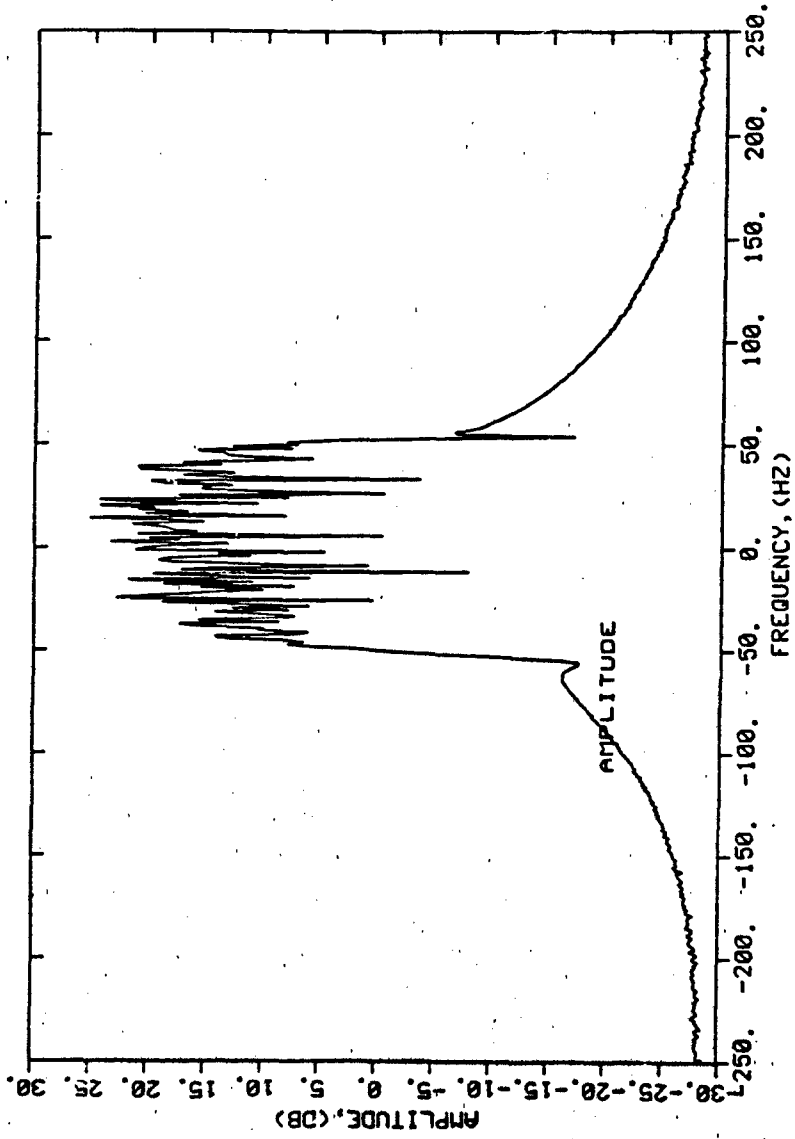
Figure 11. Power spectrum of the signal of Figure 10.

28
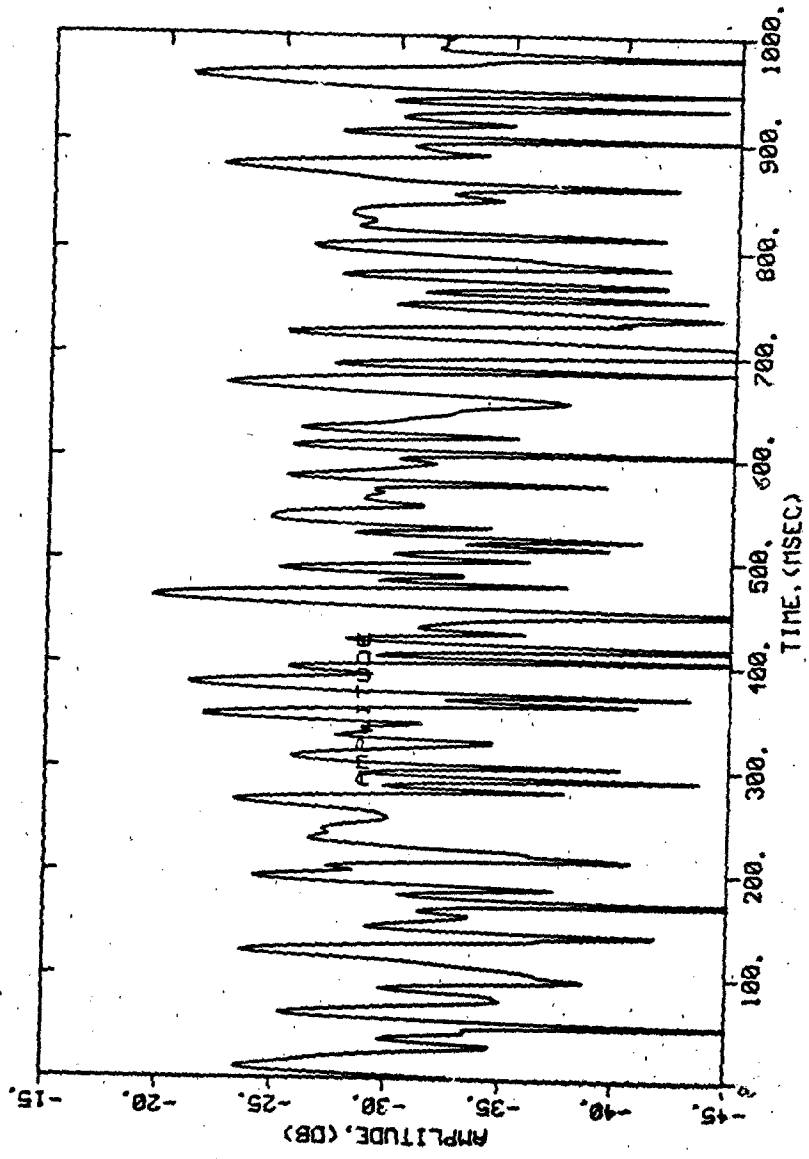
NUMBER OF DIPOLES: 512
WAVELENGTH,(INCHES): 1.125
T-ZERO,(MSEC): 100000.0

Figure 12. Amplitude of the return from 512 dipoles.

NUMBER OF DIPOLES: 512
WAVELENGTH, (INCHES): 1.125
T-ZERO, (MSEC): 100000.0

AMPLITUDE, (DB)

TIME, (MSEC)
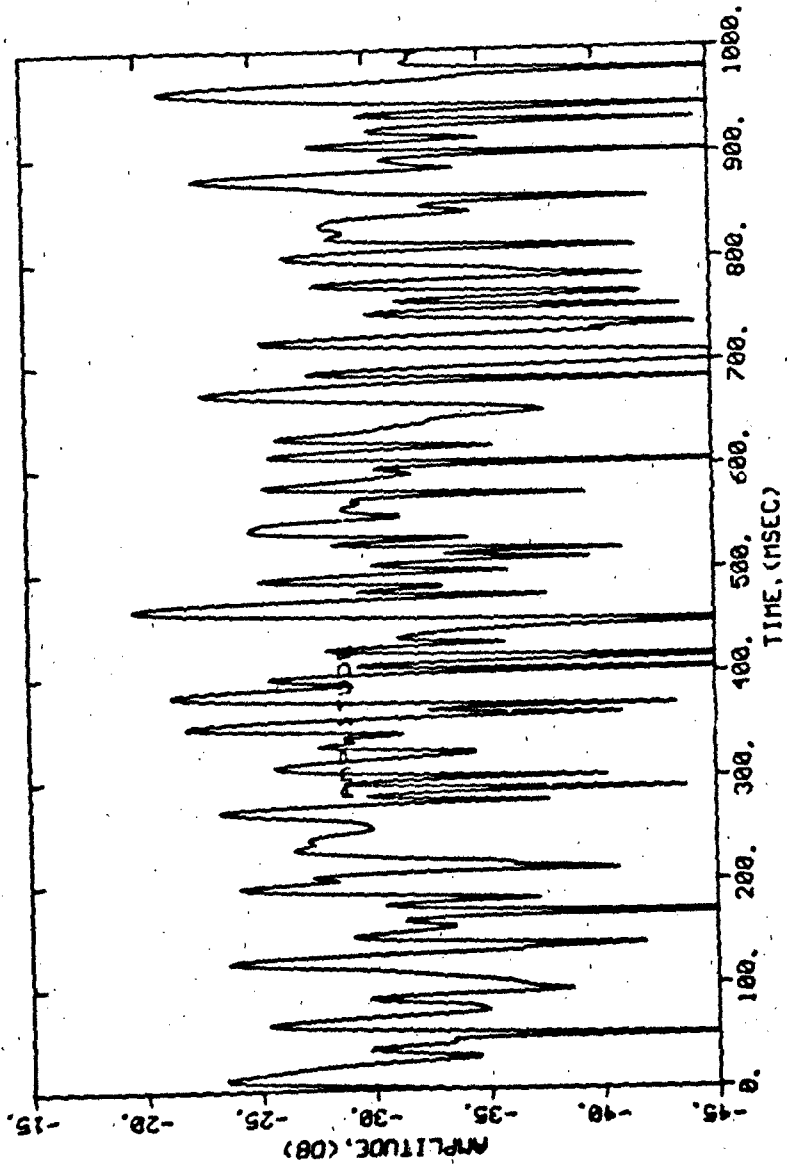
Figure 12. Amplitude of the return from 512 dipoles.

NUMBER OF DIPOLES: 512
WAVELENGTH,(INCHES): 1.125
T-ZERO,(MSEC): 100000.0
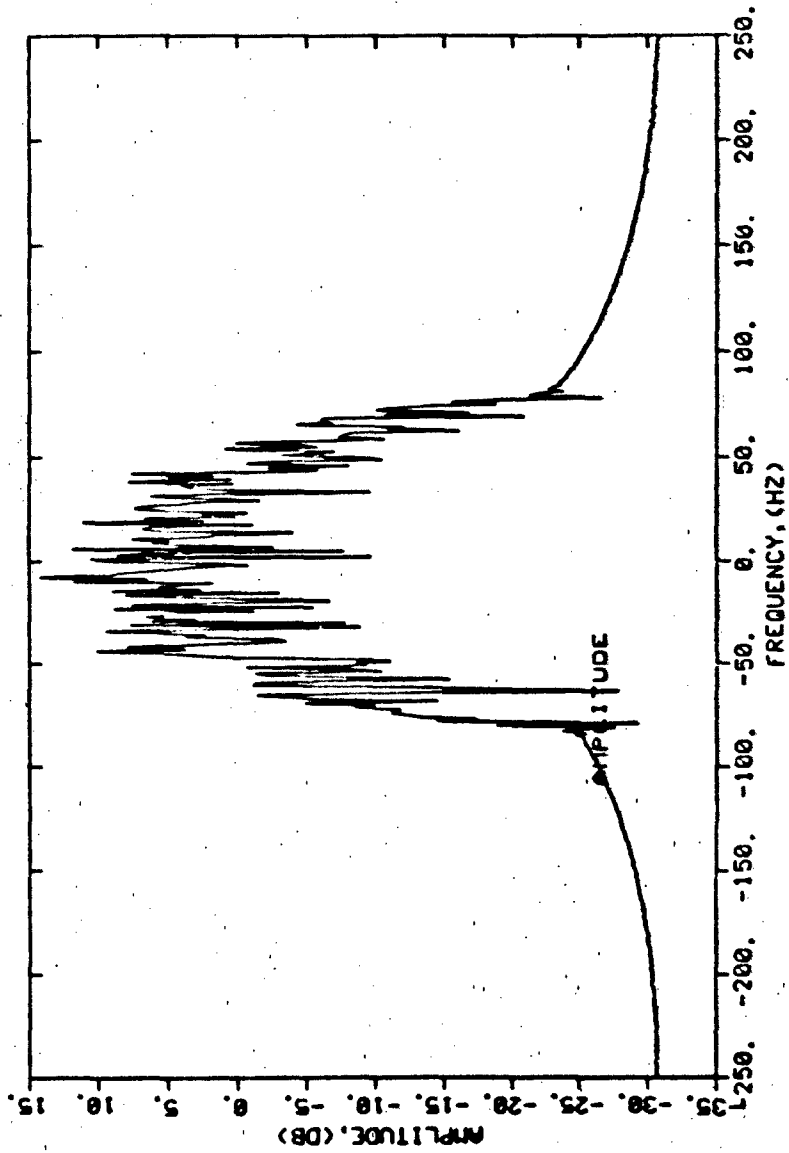
Figure 13. Power spectrum of the signal of Figure 12.

30

NUMBER OF DIPOLES: 1024
WAVELENGTH, (INCHES): 1.125
T-ZERO, (MSEC): 100000.0
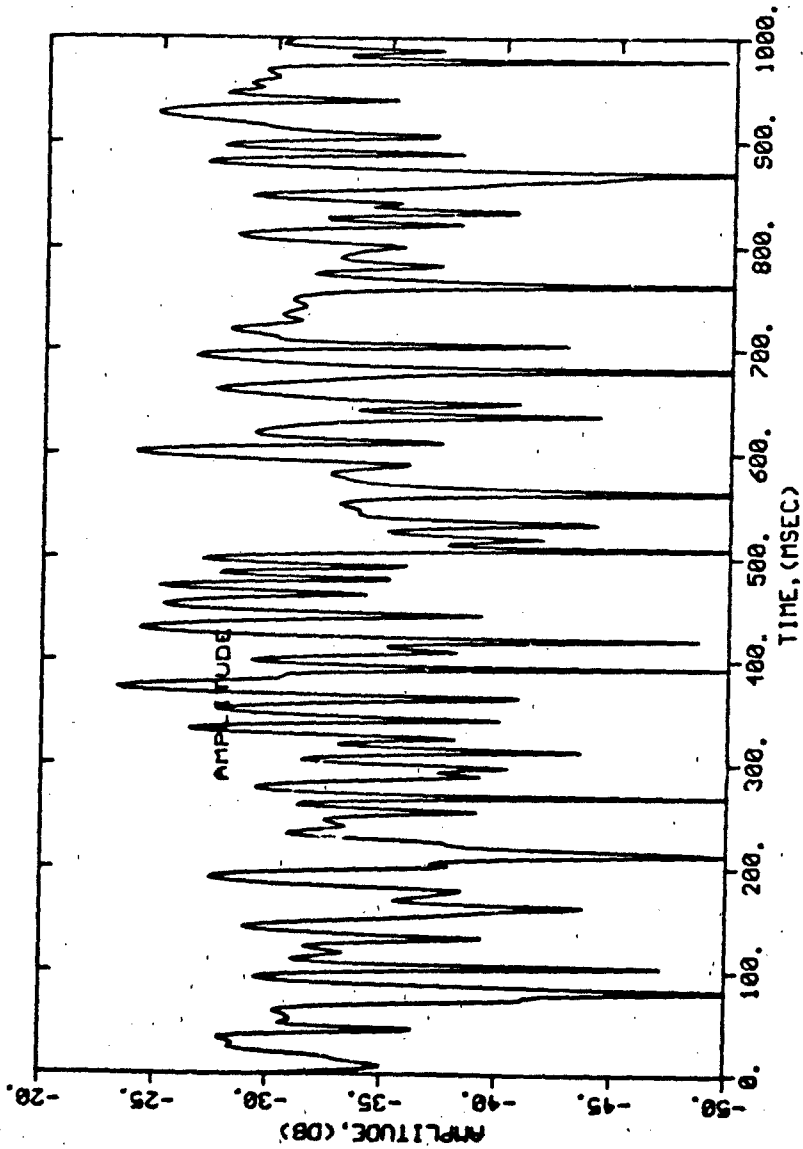
Figure 14. Amplitude of the return from 1024 dipoles.

31

NUMBER OF DIPOLES: 1024
WAVELENGTH, (INCHES): 1.125
T-ZERO, (MSEC): 100000.0
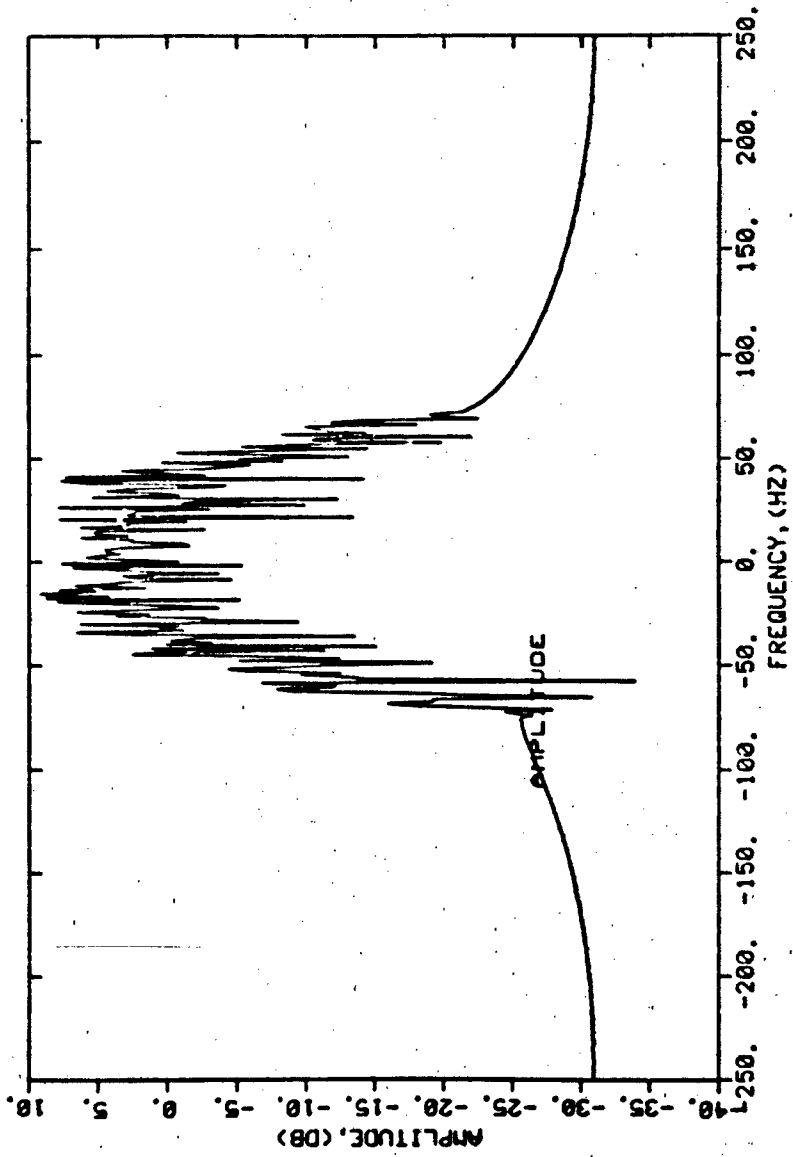
Figure 15. Power spectrum of the signal of Figure 14.

The bandwidth does not seem to be related to the dipole number density. Since the dipoles in Figures 9 through 15 were all uniformly distributed over the same horizontal distance, 1024 dipoles were much more concentrated than 32 dipoles. Thus, the bandwidth is fixed by the dipole motion properties -- not by their concentration. This fact makes it possible to separate the scintillation characteristics from the absolute dipole concentration levels in the cloud.

SECTION 4
DIPOLE MOTION MODEL

The simple model presented in Section 3.2 was only for the purpose of selecting a large enough number of dipoles to ensure that the cloud signal scintillation characteristics could be simulated using a small enough number of dipoles that the computer running time could be minimized. The effects of turbulence were ignored; for the purpose of accounting for local turbulence, a more sophisticated motion model is needed. Such a model is developed below.

The general, first order equation of motion for a chaff particle is

$$m \frac{d\bar{v}}{dt} = \frac{1}{2} \rho A_p C_D (\bar{u} - \bar{v}) |(\bar{u} - \bar{v})| + \bar{B} \qquad (4)$$

where

m = mass of the particle,

ρ = atmospheric density,

A_p = surface area of the particle projected onto the plane normal to $\bar{v}$,

C_D = drag coefficient,

$\bar{u}$ = atmospheric velocity, the instantaneous sum of steady and turbulent components,

$\bar{v}$ = particle velocity,

$\bar{B}$ = $-mg\hat{z}$ = the body force,

g = acceleration due to gravity,

$\hat{z}$ = unit vector in the upward direction.

The motion history can be determined by solving Equation (4) for $\bar{v}$, but this cannot be done analytically due to the random and unpredictable components of $\bar{u}$. To simplify the integration

34

of Equation (4), therefore, we shall assume that a time interval can be chosen small enough that ρ, A_p, C_D, and the turbulent components of $\bar{u}$ are sensibly constant during the interval. This time interval should be less than about 10 milliseconds.

We represent the atmospheric velocity as

$$\bar{u} = \hat{x}(u'_x + u''_x) + \hat{y}(u'_y + u''_y) + \hat{z}(u'_z + u''_z) \tag{5}$$

where the single primes denote the steady velocity components and the double primes denote the turbulent components. Equation (4) can be split into three equations, each corresponding to motion along one of the three Cartesian coordinates,

$$\frac{dv_x}{dt} = \epsilon \, (u_x - v_x)^2 \tag{6}$$

$$\frac{dv_y}{dt} = \epsilon \, (u_y - v_y)^2 \tag{7}$$

$$\frac{dv_z}{dt} = \epsilon \, (u_z - v_z)^2 - g \tag{8}$$

where

$$\epsilon = \pm \frac{\rho \, A_p \, C_D}{2m} \tag{9}$$

The ($\pm$) sign option is necessary to preserve the vector sense of the velocity difference $(\bar{u} - \bar{v})$ in Equation (4), and we shall assume that whichever option is required, it is known, thereby fixing the value of ϵ.

Equations (6) and (7) can be rewritten as

$$\frac{dv}{(u - v)^2} = \epsilon dt$$

where the subscripts have been omitted for convenience. Integrating, we have

$$\frac{1}{(u - v)} \left| \begin{matrix} v(t) \\ v_o \end{matrix} \right. = \epsilon t \left| \begin{matrix} t_o + \Delta t \\ t_o \end{matrix} \right.$$

35

Solving for v,

$$v(t) = u - \frac{u - v_o}{1 + \epsilon \, \Delta t(u - v_o)} \tag{10}$$

where Δt is the time interval and v_o is the velocity at the be-
ginning of that interval.

The displacement P over the time interval can be found by
integrating Equation (10), with the result

$$P(t) = P_o + u\Delta t - \frac{1}{\epsilon} \ln\left[1 + \epsilon \Delta t(u - v_o)\right] \tag{11}$$

where P_o is the particle position at the beginning of the inter-
val. This is a pure translation due to the horizontal components
of the atmospheric velocity. To this must be added the horizon-
tal components of the spiral motion mentioned in Subsection
3.2. These added components can be represented by

$$x = x_o + a \, \cos(\Lambda + \Omega t) \tag{12}$$

$$y = y_o + a \, \sin(\Lambda + \Omega t) \tag{13}$$

Consequently, the horizontal positions are given by

$$x(t) = x_o + (u'_x + u''_x)\Delta t + a \, \cos(\Lambda + \Omega t)$$
$$+ \frac{1}{\epsilon} \ln\left[1 + \epsilon \Delta t(u'_x + u''_x - v_{ox})\right] \tag{14}$$

$$y(t) = y_o + (u'_y + u''_y)\Delta t + a \, \sin(\Lambda + \Omega t)$$
$$+ \frac{1}{\epsilon} \ln\left[1 + \epsilon \Delta t(u'_y + u''_y - v_{oy})\right] \tag{15}$$

and the velocity components are

36

$$v_x(t) = (u'_x + u''_x) - \frac{u'_x + u_x - v_{ox}}{1 + \varepsilon \Delta t(u'_x + u''_x - v_{ox})} \qquad (16)$$

$$v_y(t) = (u'_y + u''_y) - \frac{u'_y + u''_y - v_{oy}}{1 + \varepsilon \Delta t(u'_y + u''_y - v_{oy})} \qquad (17)$$

The solution for the vertical direction is more complicated because of the gravity term. Equation (8) can be written as

$$\frac{dV}{V^2 - \frac{g}{\varepsilon}} = - \varepsilon \, dt \qquad (18)$$

where we have again ignored subscripts and where $V = u - v$. The integral of Equation (18) has two different forms depending on the sign of ε. These forms are

$$\int \frac{dx}{x^2 + c^2} = \frac{1}{c} \tan^{-1}(\frac{x}{c})$$

$$\int \frac{dx}{x^2 - c^2} = \frac{1}{2c} \ln \frac{x - c}{x + c}$$

Thus, for $\varepsilon < 0$, which corresponds to $u_z < v_z$,

$$\tan^{-1} \left[\frac{u - v(t)}{c}\right] - \tan^{-1} \left[\frac{u - v_o}{c}\right] = - c\varepsilon \Delta t$$

or

$$v_z(t) = (u'_z + u''_z) - c \tan \left\{ \tan^{-1} \left[\frac{u'_z + u''_z - v_o}{c} \right] - c\varepsilon \Delta t \right\} \qquad (19)$$

where

$$c = \left\{ \frac{2mg}{\rho \, A_p \, C_D} \right\}^{1/2} \qquad (20)$$

Equation (19) must be integrated to find the displacement:

$$\int_{z_o}^{z(t)} dz = \int_{t_o}^{t_o+\Delta t} (u'_z + u''_z)dt - c\int_{t_o}^{t_o+\Delta t} \tan(\xi - c\epsilon\Delta t)dt$$

where

$$\tan\xi = \frac{u'_z + u''_z - v_{oz}}{c} \tag{21}$$

The result is

$$z(t) = z_o + (u'_z + u_z)\Delta t - \frac{1}{\epsilon}\ln\left\{\cos(c\epsilon\Delta t) + \frac{u'_z + u''_z - v_{oz}}{c}\sin(c\epsilon\Delta t)\right\} \tag{22}$$

When $\epsilon > 0$, corresponding to $u_z > v_z$, the integration of Equation (18) yields

$$\ln\left\{\frac{u - v(t) - c}{u - v(t) + c} \cdot \frac{u - v_o + c}{u - v_o - c}\right\} = -2c\epsilon\Delta t$$

which, when solved for $v(t)$, gives

$$v_z(t) = (u'_z + u''_z) - c\frac{(u'_z + u''_z - v_{oz}) + c\tanh(c\epsilon\Delta t)}{c + (u'_z + u''_z - v_{oz})\tanh(c\epsilon\Delta t)} \tag{23}$$

In order to integrate Equation (23) to find the displacement, we can express Equation (23) as

$$\int_{z_o}^{z(t)} dz = \int_{t_o}^{t_o+\Delta t} u\, dt + c\int_{t_o}^{t_o+\Delta t} \frac{1 + de^{pt}}{1 - de^{pt}}\, dt \tag{24}$$

where

$$d = \frac{u - v_{oz} + c}{u - v_{oz} - c}e^{-2c\epsilon t_o} \tag{25}$$

$$p = 2c\epsilon \tag{26}$$

38

The integral of the last term in Equation (24) is

$$t - \frac{2}{p} \ln(1 - de^{pt})$$

hence the solution is

$$z(t) = z_o + (u + c)\Delta t - \frac{2c}{p} \ln \frac{1 - de^{pt}}{1 - de^{pt_o}}$$

Inserting the values of d and p,

$$
\begin{aligned}
z(t) = z_o &+ \left[(u'_z + u''_z) + c \right] \Delta t \\
&- \frac{1}{\varepsilon} \ln \left\{ \frac{1}{2c} \left[(u'_z + u_z'') + (c - v_o) \right] e^{2c\varepsilon\Delta t} \right. \\
&\left. - \frac{1}{2c} \left[(u'_z + u''_z) - (c + v_o) \right] \right\}
\end{aligned}
\tag{27}
$$

In summary, Equations (14) and (15) give the displacements in the horizontal plane and Equations (16) and (17) are the velocities. Depending on the sign of Equation (9), the displacement and velocity in the vertical plane are given by Equations (19) and (22) or by Equations (23) and (27).

In the implementation of these motion equations, the new particle positions and velocities are updated from the previous ones, and Δt is the time interval over which the updates are made. The parameters required to generate a time history are

1. Particle characteristics (length, diameter and mass),
2. Initial position,
3. Initial orientation,
4. Spiral characteristics (rate, radius and sense)
5. Drag coefficient of the particle,
6. Atmospheric characteristics (density and velocity)
7. Turbulence components, and
8. Time increment.

The particle characteristics are available in a table stored internally. When a given chaff load is specified, the length, diameter and mass of the chaff dipole types are retrievable. The initial positions and orientations of the dipoles are randomly generated; typically they are uniformly distributed throughout a relatively small cube. Once the chaff is released, the time is incremented and the motion for each dipole is computed according to the equations derived above.

The sequence is started by randomly generating the initial angle of attack and the Reynolds number. Since these two variables determine other properties of the motion via the solutions of transcendental equations, an iterative procedure is used to establish the remaining initial conditions. The starting values for the angle of attack and the Reynolds number are used as inputs to a look-up table which returns the axial and normal force coefficients C_N and C_A. This pair of coefficients is used to compute the drag coefficient,

$$C_D = C_A \cos\alpha + C_N \sin\alpha \tag{28}$$

Also, the projected area is

$$A_p = \frac{\pi}{4} D^2 + L\, D \sin\alpha \tag{29}$$

where D and L are the dipole diameter and length.

We now have the values necessary to compute the dipole velocity along the helical path,

$$v = \left\{ \frac{2mg \sin\gamma}{\rho\, C_D A_p} \right\}^{1/2} \tag{30}$$

The vertical velocity component is

$$v_z = v \sin\gamma \tag{31}$$

and, for the purposes of establishing the initial conditions, we will choose the angle of attack, α, such as to force Equation (31) to take on a specified value, typically 1 or 3 feet per second, depending on the chaff type. Using the value computed from Equation (30), this angle is

$$\alpha = \text{arc sin} \left\{ \frac{2mg \; v_z^2}{\rho \; A_p \; C_D} \right\}^{1/3} - \theta \tag{32}$$

The Reynolds number depends on the velocity,

$$R_e = \rho v \; L/\mu \tag{33}$$

where μ is the kinematic viscosity of the air. The value of R_e is computed using Equation (33) and is compared with the value initially generated randomly. If the value computed from Equation (33) is close enough to the generated value, the initial conditions for the dipole are regarded as being established. If not, the new value of α i used with the remaining parameters to compute a new Reynolds nu... , and the process is iterated until a Reynolds number is computed that matches the one generated. We have now established the initial conditions.

The spiral rate is then computed using

$$\Omega = \frac{2v}{L \; \cos\theta} \cdot \frac{C_{SM}}{C_{NR}} \tag{34}$$

where C_{SM} is the side moment coefficient and C_{NR} is the damping derivative for the side moment plane. Both coefficients are tabulated as functions of the angle of attack and the Reynolds number. The spiral radius is

$$a = \frac{v}{\Omega} \cos\gamma \tag{35}$$

where $\gamma = \alpha + \theta$ is the helical pitch angle. Having computed these quantities, we can now determine the motion history by

41

indexing through time and using the horizontal and vertical velocity and position equations derived above.

In stepping through time, the angle of attack and the orientation angle θ are deliberately "jiggled" by the addition of small random changes. Turbulence is induced in the velocity vector $\bar{u}$ by use of the description given by Brunk, et al., in which a new (updated) velocity component is formed from a weighted sum of the old (previous) component and a random component. This weighting uses correlation coefficients that are, in general, different for the three components of the atmospheric wind velocity.

In the z direction, the appropriate correlation coefficient is

$$R_z(u'_z, \Delta t) = \exp \left\{ -\Delta t \left[\frac{1}{\tau^2} + \left(\frac{u'_z}{L_z} \right)^2 \right]^{1/2} \right\} \tag{36}$$

where τ is the correlation time and L_z is a length parameter. The correlation time can be computed from

$$\tau = \frac{\exp(2.2 - 6.5i)}{\left| \dfrac{dw}{dz} \right| + \dfrac{\sigma_w}{L_z}} \tag{37}$$

where

$\dfrac{dw}{dz}$ = the derivative of the mean wind velocity with altitude

i = an intensity,

σ_w = the standard deviation of the intensity distribution.

L_z, σ_w, $\dfrac{dw}{dz}$, and i are tabulated functions of altitude for a "standard" atmosphere. Thus, τ varies with altitude.

A new turbulent wind velocity can be generated from the old one by the formula

42

$$u"_z \big|_{new} = R_z u"_z \big|_{old} + (1 - R_z^2)^{1/2} J_m \qquad (38)$$

where J_m is a Gaussian velocity distribution with zero mean and a standard deviation σ_w. Computation of the turbulent components in the horizontal directions requires another pair of correlation coefficients,

$$R_x = \exp\left\{ -\Delta t \left[A + \frac{1}{2A} \left(\frac{u'_x}{2L_x} \right)^2 \right] \right\} \qquad (39)$$

$$R_y = \exp\left\{ -\Delta t \left[B + \frac{1}{2B} \left(\frac{u'_y}{2L_y} \right)^2 \right] \right\} \qquad (40)$$

where

$$A = \left[\frac{1}{\tau^2} + \left(\frac{u'_x}{2L_x} \right)^2 \right]^{1/2} \qquad (41)$$

$$B = \left[\frac{1}{\tau^2} + \left(\frac{u'_y}{2L_y} \right)^2 \right]^{1/2} \qquad (42)$$

The length parameters are related by $L_z = 2L_x = 2L_y$. Finally, the updated wind velocity components in the horizontal directions are

$$u"_x \big|_{new} = R_x u"_x \big|_{old} + (1 - R_x^2)^{1/2} J_m \qquad (43)$$

$$u"_y \big|_{new} = R_y u"_y \big|_{old} + (1 - R_y^2)^{1/2} J_m \qquad (44)$$

In these expressions, one should be careful to distinguish the mean velocity components bearing single primes from the double primed turbulent components.

Figures 16 through 18 are examples of how the position history behaves for a collection of 16 dipoles. These figures represent the projections of the dipole positions onto the three coordinate planes for 55 seconds of free fall in a turbulent
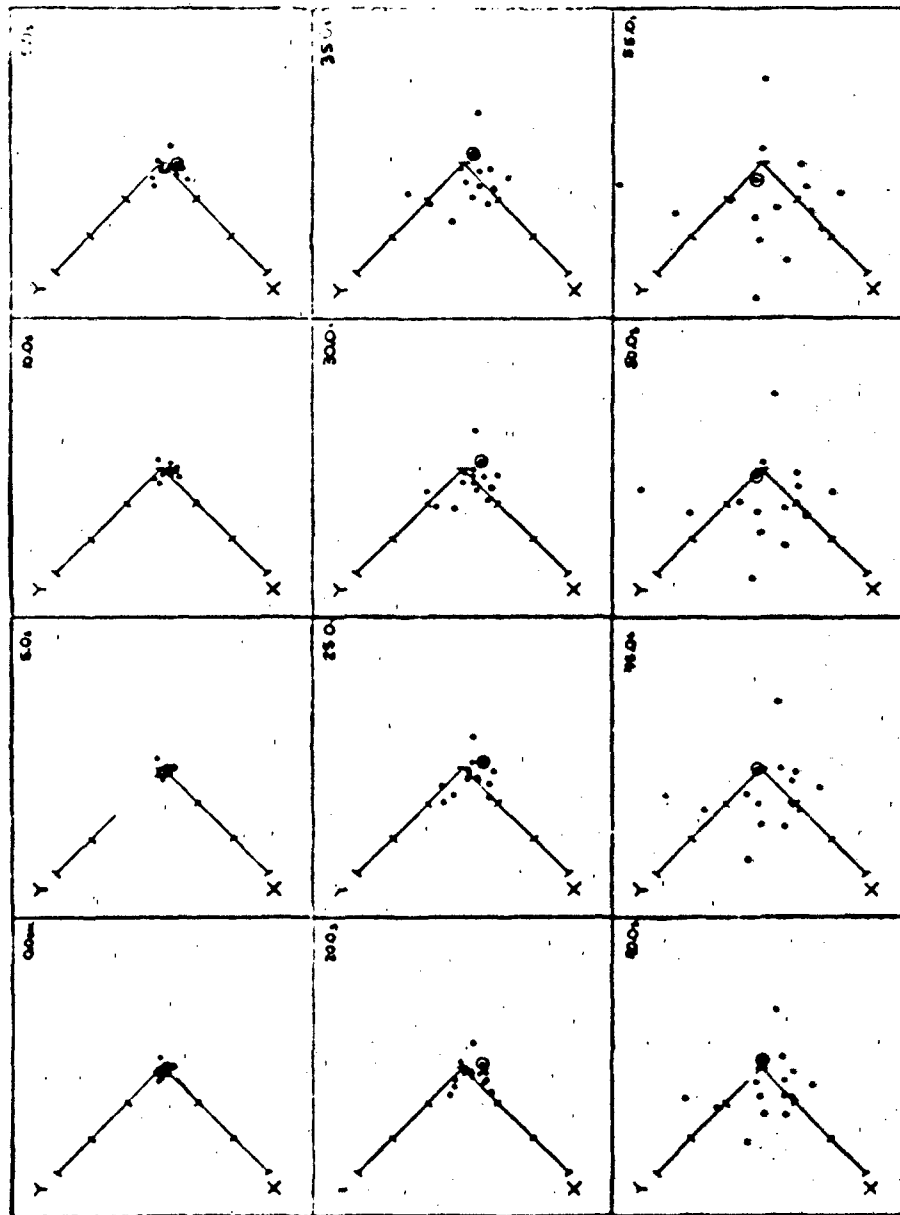
Figure 16. Position history of 16 dipoles in the horizontal direction for 55 seconds.

44
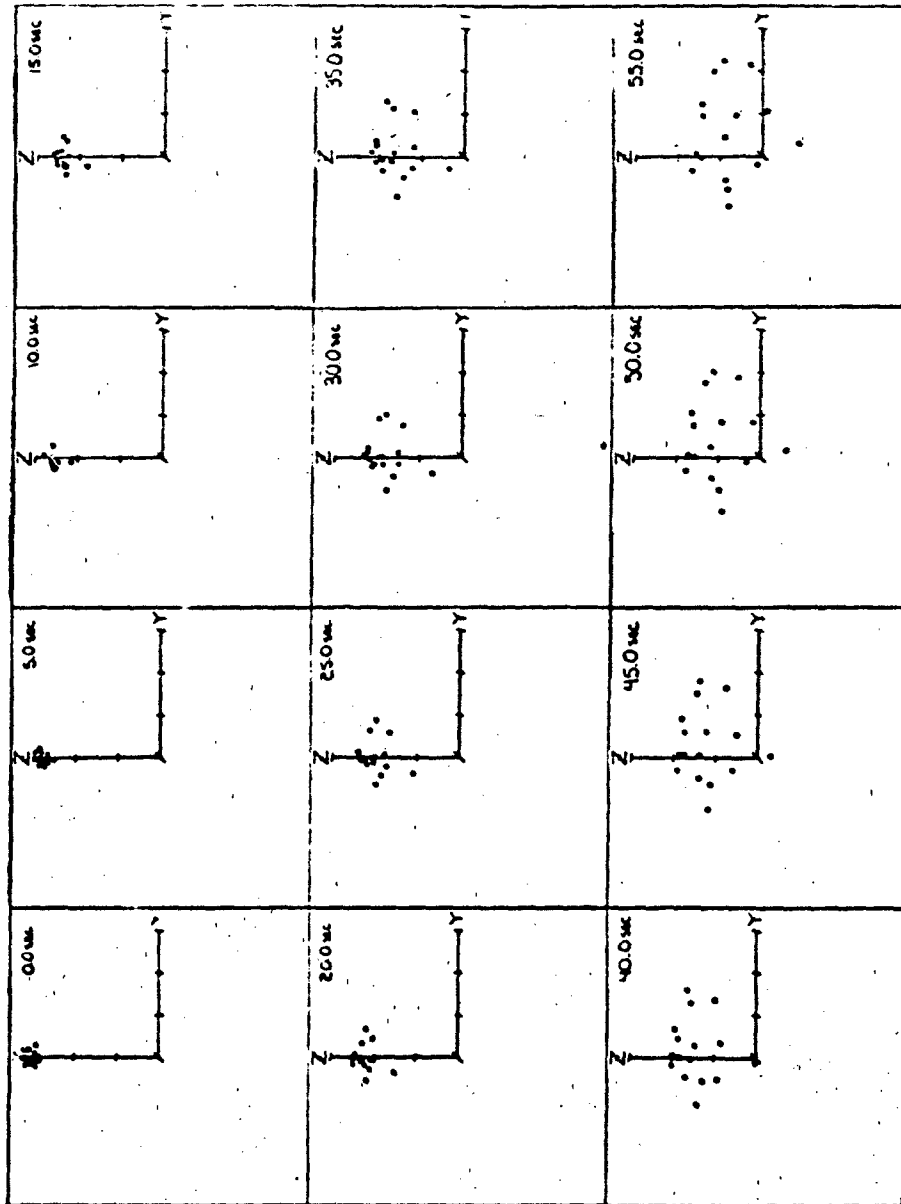
Figure 17. Position history of 16 dipoles in a vertical direction for 55 seconds.
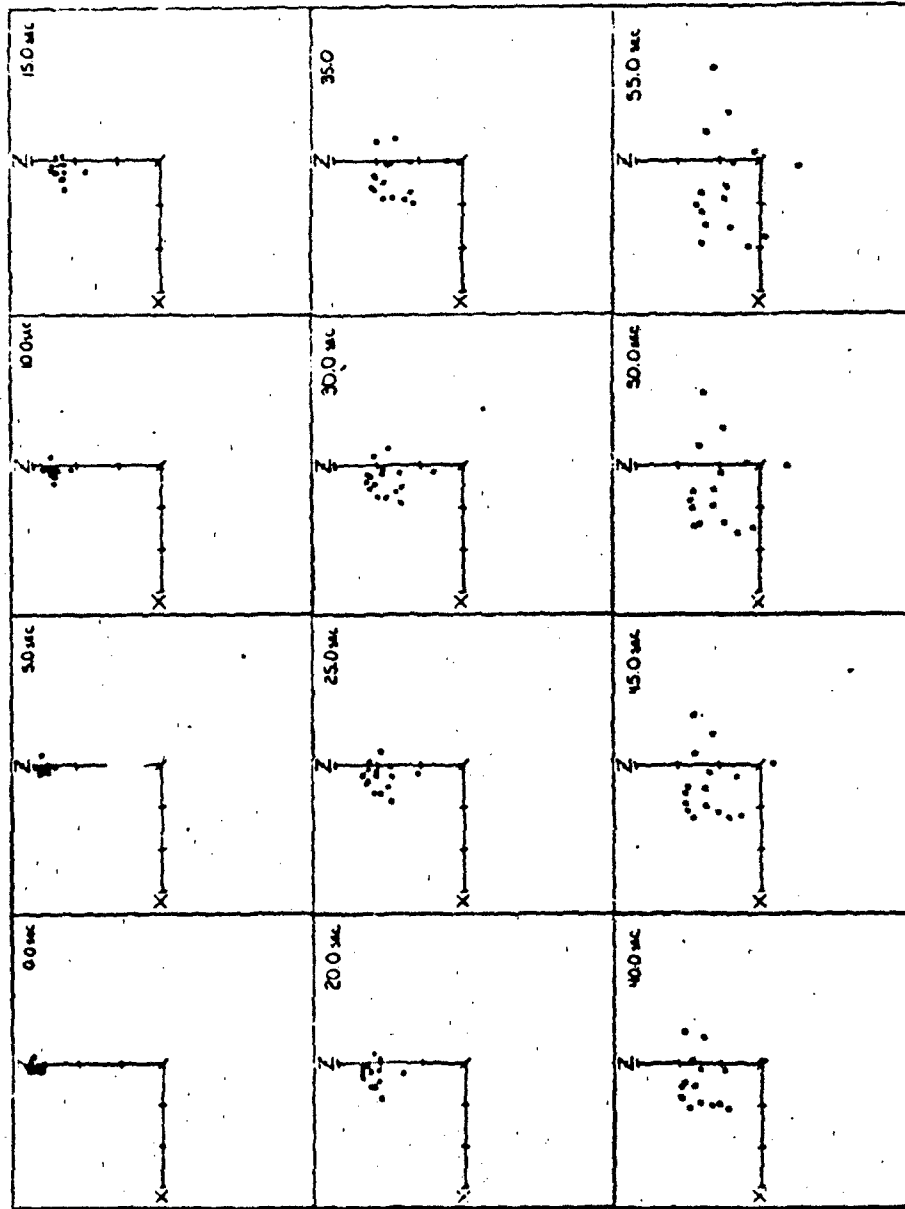
Figure 18. Position history of 16 dipoles in a vertical plane for 55 seconds.

atmosphere. The position axes are marked off at 50-foot intervals and the dipoles were initially placed in a cube 25 feet along a side.

Figure 16 shows how the dipoles spread out in the horizontal plane. At the end of 55 seconds, some dipoles are as much as 150 feet away from their initial position, suggesting drift rates as high as 3 feet/second. Once in motion horizontally, the dipoles tend to maintain that velocity. However, careful examination of the 12 frames shows that some of the paths have a distinct curvature that could represent spiral trajectories of very large radius. A typical spiral should be less than 2 or 3 feet in diameter.

A position history in a vertical plane is shown in Figure 17. The spreading out in the vertical plane is not as great as in the horizontal plane. After 55 seconds, the centroid of the cloud appears to be about 100 feet lower than it was at the beginning, implying a fall rate of less than 2 feet per second. Figure 18 shows the spreading in the other vertical plane. Observe that one dipole broke away from the main group and fell about 40% faster than the others. This particular dipole executed more than half a revolution around its spiral path during the 55-second history, suggesting a rate of about 0.1 radian per second. (The dipole is ringed by a small circle in Figure 16 for identification.) Note that there seems to be general drift along the x-axis, implying a steady wind component of about a foot per second, which was, in fact, specified on input.

SECTION 5
DIPOLE DISTRIBUTION MODEL

5.1 PLUME DISTRIBUTION

To estimate the radar return from the cloud, we need to know where the cloud is, what its shape is, the dipole density distribution within the cloud, the radar location, the radar pointing direction, and the antenna radiation pattern. An integration of the product of the dipole density function and the antenna pattern function over the extent of the cloud will give a number proportional to the mean radar return. The fine-grain time varying signature can be described by separately exercising the turbulence and scattering models already developed. Let us focus for the time being on the amplitude only, and let the cloud be "corridor chaff" dispensed continuously by an aircraft moving at constant altitude and velocity.

A possible model of the dispensed chaff cloud is a truncated conical plume, as shown in Figure 19. Since the aircraft velocity is much greater than the dipole settling rate, the plume axis will be essentially horizontal. If we now conceive of the plume as being attached to the aircraft, it will be "pulled" at a velocity equal to the vector sum of the aircraft and wind velocities. For simplicity, we assume the wind velocity (direction and speed) to be constant. Then the cloud will move as shown in Figure 19, and we can predict where the plume axis will be at any point in time. We now need to determine the dipole density distribution within the cloud.

The work of Traci, et al., suggests that the dipole density distribution in a plane transverse to the plume axis is a bivariate Gaussian function. Although the Traci team dealt only with chaff puffs (not plumes), their data may be used to estimate the expansion rate of the cloud.

First let us assign a coordinate system to the plume, as in Figure 19, where the plume axis coincides with one axis of a right-handed Cartesian system. The distance u is measured up-

48

earth
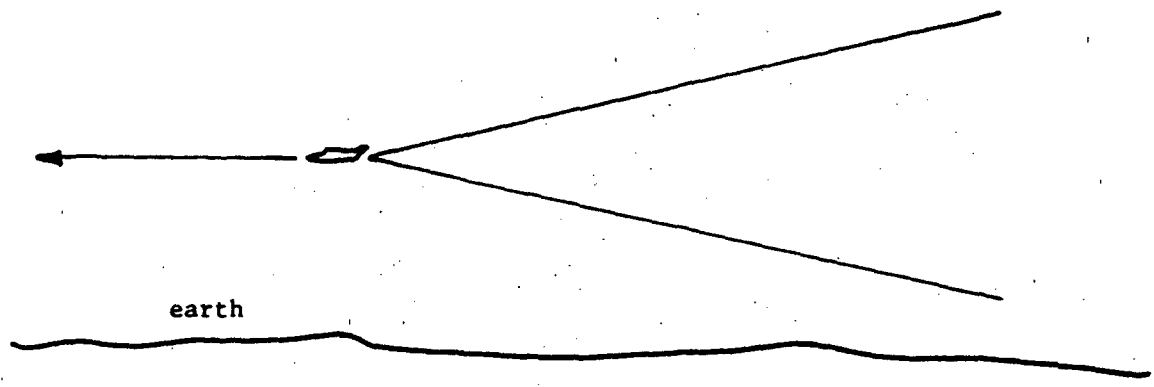
elevation view
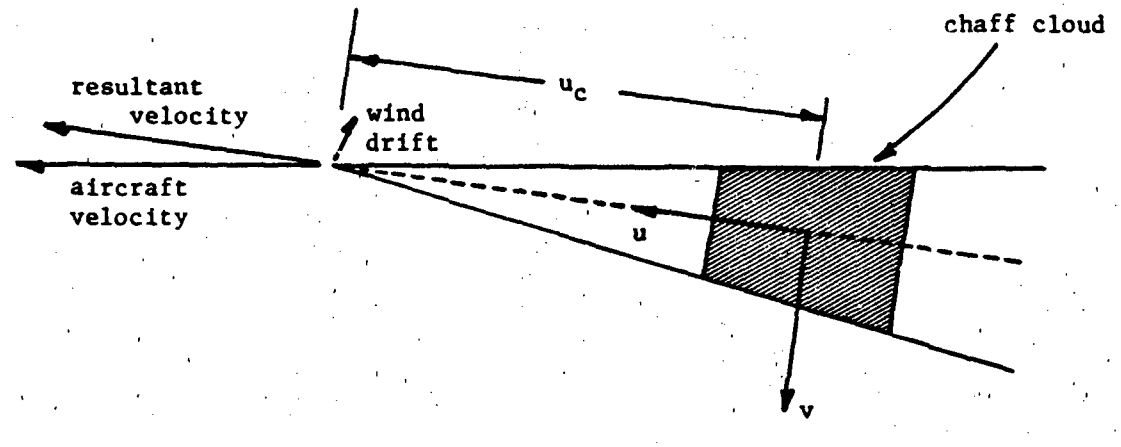
plan view

Figure 19. Chaff plume model and coordinate system.

stream from the cloud centroid and v is measured transverse to this dimension in a horizontal plane. The vertical distance z is measured upward. We assume the transverse dipole density function has the form

$$\rho(v,z) = \rho_0 \exp\left[-1/2 \left\{(\frac{v}{\sigma_v})^2 + \left(\frac{z - z_c}{\sigma_z}\right)^2\right\}\right] \qquad (45)$$

where ρ_0 is a constant related to the dispersal rate (i.e., dipoles per meter or dipoles per second), z_c is the vertical location of the plume axis and σ_v and σ_z are the standard deviations in the transverse plane. These standard deviations obviously increase with time or downstream distance from the plume apex, and we need to establish the expansion rate. We shall ignore for the moment the steady decrease in z_c as the cloud settles vertically to the ground.

Traci, et al., present plots of density contours for several different atmospheric conditions for four elapsed times after dispersal. The expansion rate can be estimated by reading the charts, solving Equation (45) for σ_v or σ_z, and plotting the results. We choose the atmospheric condition labeled Simulation 6 in the Traci report, corresponding to a shear profile with neutral stability. From the Traci figures, Table 3 can be constructed for $\rho_0 = 1000$.

TABLE 3. PLUME PARAMETERS

t,min	ρ	v,m	$z-z_c$,m	σ_v,m	σ_z,m
2	–	–	–	50.0	30.0
12	15	210	150	72.5	51.8
22	5.1	330	210	135.2	86.1
32	2.69	430	250	159.9	93.0

Except for the data at t = 2 minutes, for which Traci, et al., present σ_v and σ_z as an analytical fit, the last two columns were computed assuming the form given by Equation (45), and the data as read from the Traci figures are listed in the first four columns.

The open and closed circles in Figure 20 represent the deduced values listed in Table 3. The curves are approximate fits to those data assuming the form

$$\sigma = (\ell \, \dot{u} \, t)^{1/2} \tag{46}$$

where ℓ is a characteristic "length" determined from the data (i.e., a curve fitting constant), $\dot{u}$ is the speed of the aircraft and t is the elapsed time since dispersal. For a speed of 200 m/s, the characteristic lengths that produce the two curves in Figure 20 are

$$\ell_v = 6.67 \text{ cm}, \qquad \ell_z = 2.6042 \text{ cm} .$$

If we now insert Equation (46) into Equation (45), we have

$$p(\dot{u},v,z,t) = \rho_o \exp\left[-\frac{1}{2\dot{u}t} \left\{ \frac{v^2}{\ell_v} + \frac{(z-z_c)^2}{\ell_c} \right\} \right] \tag{47}$$

The units in Equation (47) must be consistent, of course, so that the exponent remains dimensionless.

If we now assume that, once dispersed, the dipoles have no net motion along the plume axis, then the total number of dipoles in a thin transverse slice through the plume must remain constant. The dipoles may spread out transversely, thereby lowering the concentration, but the total number must not change. In a transverse slice of thickness Δu, therefore, there will be an unvarying number of dipoles, N

51
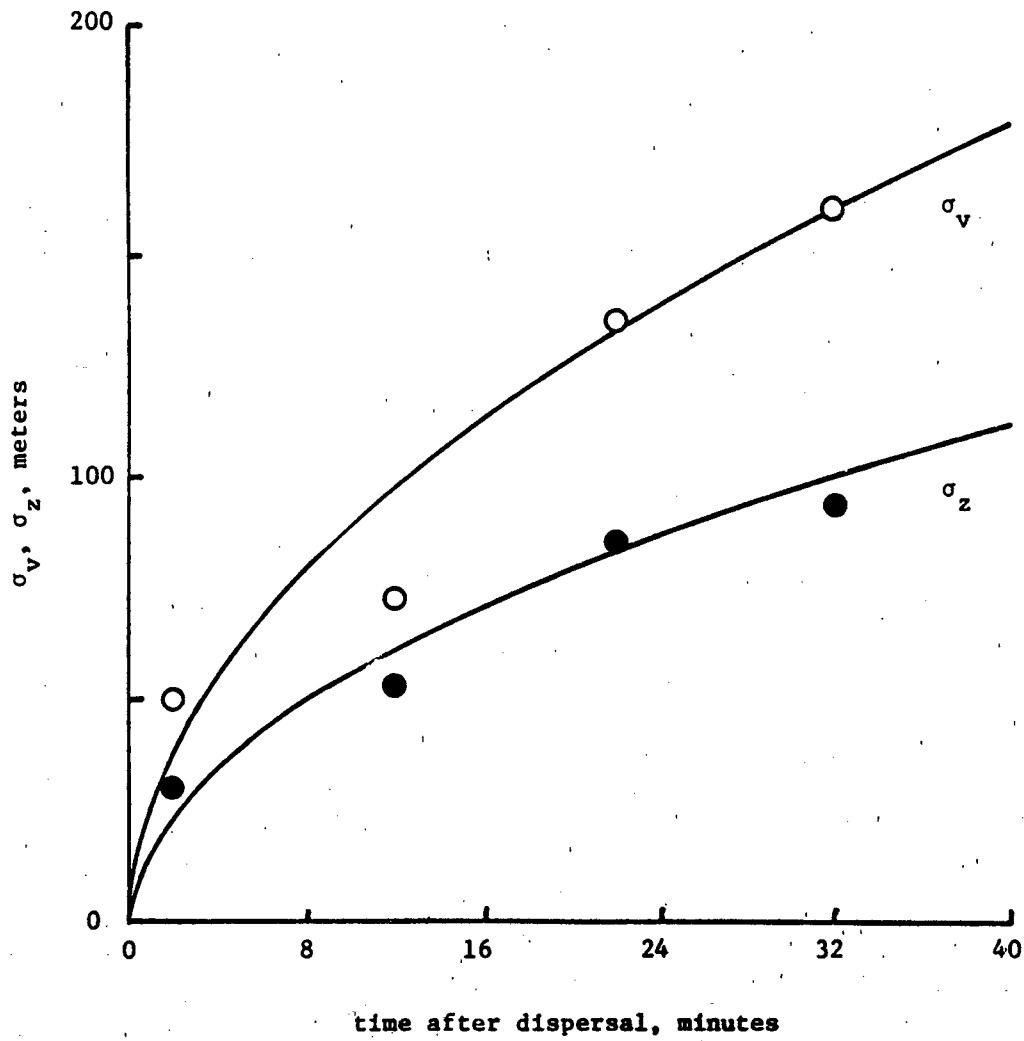
Figure 20. Deduced standard deviations and approximate curves fitted to the deduced values.

$$N = \int_S \Delta u \, \rho(\dot{u}, v, z, t) \, ds$$

$$= \Delta u \, \rho_0 \int_{-\infty}^{\infty} \exp\left(-\frac{v^2}{2\dot{u}t\ell_v}\right) dv \int_{-\infty}^{\infty} \exp\left(-\frac{(z-z_c)^2}{2\dot{u}t\ell_v}\right) dz$$

$$= 2 \, \dot{u}t \, \Delta u \, \rho_0 \sqrt{\pi \, \ell_v \, \ell_z} \quad .$$

Consequently, the concentration ρ_0 is a time dependent quantity,

$$\rho_0(t) = \frac{N}{2\dot{u}t \, \Delta u \, \sqrt{\pi \, \ell_v \, \ell_z}} \tag{48}$$

Note that ρ_0 has the dimensions of $(\text{volume})^{-1}$ and is therefore a dipole number density.

Roll chaff is commonly described by the number of dipoles per inch packed into the roll, and the chaff dispenser ejects the dipoles at rates measured in inches per minute. Let n be the number of dipoles per inch and let d be the dispersing rate in inches per second. The number of dipoles dispensed in an interval of Δt seconds is therefore

$$N = nd\Delta t \quad .$$

The distance Δu traveled by the aircraft during this interval is

$$\Delta u = \dot{u}\Delta t.$$

Hence,

$$\frac{N}{\Delta u} = \frac{nd}{\dot{u}}$$

and

$$\rho_0(t) = \frac{nd}{2(\dot{u})^2 \, t\sqrt{\pi \, \ell_v \, \ell_z}} \quad . \tag{49}$$

53

Therefore, the dipole density distribution is

$$\rho(\overset{\bullet}{u},u,v,z,t) = \frac{nd}{2(u + u_c)\overset{\bullet}{u}\sqrt{\pi}\ \ell_v\ \ell_z} \cdot \exp\left[-\frac{1}{2(u + u_c)}\left\{\frac{v^2}{\ell_v} + \frac{(z - z_c)^2}{\ell_z}\right\}\right] \tag{50}$$

where $u_c = \overset{\bullet}{u}t$ is the separation between the aircraft and the cloud centroid and t is the elapsed time since the aircraft passed the point represented by the centroid.

Recognizing that $u = \overset{\bullet}{u}t$ is the distance along the plume axis at the point where ρ is measured, and accounting for inefficiencies due to "birdnesting," we can express Equation (50) as

$$\rho(u,\overset{\bullet}{u},v,z,t) = \frac{\eta nd}{2(u + u_c)\ \overset{\bullet}{u}\sqrt{\pi}\ \ell_v\ \ell_z} \cdot \exp\left[-\frac{1}{2(u + u_c)}\left\{\frac{v^2}{\ell_v} + \frac{(z - z_c)^2}{\ell_z}\right\}\right] \tag{51}$$

where η is the efficiency. This constitutes a complete description of the dipole number density as a function of position within the cloud.

To gain some idea of what this distribution is, let us assume a roll chaff package having 600,000 dipoles per inch dispensed at a rate of one inch per minute. Hence, the dipoles are dispensed at the rate $nd = 10^4$ dipoles per second. If the efficiency is 30% and if the aircraft travels at 200 m/s, the dipole density along the plume axis is $101.553/(u + u_c)$ dipoles per m^3. Thus, 100 meters from the apex the density is about 1 dipole per cubic meter.

For distributions of the form $\exp(-x^2/2\sigma^2)$, the concentration at $x = 3.035$ is only 1% of the concentration at $x = 0$,

and 99.73% of the dipoles are contained within these boundaries. If we choose $x = 6.07\sigma$ as being representative of the cloud thickness, the growth of the cloud is as shown in Table 4.

TABLE 4. PLUME DIMENSIONS

t, minutes	width, m	depth, m
10	556	348
20	787	491
30	966	602

5.2 VOLUME INTEGRATION

Given the dipole density distribution within the plume, we have the task of finding the net received signal from that distribution. We begin by considering the "conventional" form of the radar range equation,

$$P_r = P_t \; \frac{G_t G_r \sigma \lambda^2}{(4\pi)^3 R^4} \tag{52}$$

where P_r = received power,

P_t = transmitted power,

G_t = gain of the transmitting antenna,

G_r = gain of the receiving antenna,

σ = radar cross section of an isolated target,

λ = radar wavelength,

R = range from radar to target.

In this expression, it should be remembered that G_t and G_r are angle-dependent functions that describe the concentration of energy in a given direction. The two functions are equal for radars employing a common transmit/receive antenna, and we shall assume this to be the case. Since the chaff cloud is an extended scatterer, the return from each dipole must be weighted according to the antenna gain in the particular direction the dipole may be found. Thus, Equation (52) must be applied to each dipole.

This is not possible, of course, since there can be millions of dipoles in the cloud. Instead, we shall assume that the return from an elemental volume of the chaff cloud is directly proportional to the number of dipoles in that volume. If we assume further that the number density varies continuously from point to point in the cloud, Equation (52) can be written as a volume integral,

$$P_r = \frac{P_t \lambda^2}{(4\pi)^3} \int_V \frac{G^2 \sigma}{R^4} \, dV \tag{53}$$

where σ must now be expressed in terms of the scattering cross section per unit volume.

We assume that the scattering cross section per unit volume can be obtained (as described elsewhere in this report) from the tumble average scattering per dipole; when multiplied by the dipole number density ρ, as obtained in Section 5.1, this gives the desired quantity. Since the distance to the elemental volume dV may vary considerably, the range R is retained within the integral of Equation (53).

The antenna power gain function G can be expressed as the product of the boresight gain G_0 and the antenna voltage pattern. The antenna pattern, in turn, can be expressed as the product of a pair of field patterns in orthogonal planes; we allow these two patterns to be different because it is quite common to design radar antennas with fan beams. For simplicity, we assume the antenna to be a paraboloidal reflector illuminated

56

by a feed with a cosine aperture distribution taper in both planes. The field pattern has the form,

$$f(w) = \frac{\cos(\pi w/2)}{1 - w^2} \tag{54}$$

where $w = (2/\pi) kL \sin\phi$,

   L = the length of the aperture in the plane in which ϕ is measured,

   ϕ = the off-boresight angle,

   $k = 2\pi/\lambda$, the free space wave number.

If the gain is sufficiently high, the far sidelobes of the pattern will occur at relatively small angles, whereupon Equation (54) can be approximated by

$$w = 2.37793 \frac{\phi}{\phi_b} \tag{55}$$

where ϕ_b is the half-power beamwidth as measured between the half-power points (not the half beamwidth measured from the boresight axis).

Since there are two patterns measured in orthogonal planes, say in the azimuth and elevation directions, we can allow these patterns to be different. Thus, Equation (53) can be expressed as

$$P_r = \frac{P_t \lambda^2 G_o^2}{(4\pi)^3} \langle\bar{\sigma}\rangle \int_V \left\{\frac{f(p) f(q)}{R}\right\}^4 \rho \, dV \tag{56}$$

where G_o = antenna boresight power gain,

   $\langle\bar{\sigma}\rangle$ = mean radar cross section per dipole,

   $p = 2.37793 \, a/a_b$,

   $q = 2.37793 \, \epsilon/\epsilon_b$,

   a = angular displacement of dV from the antenna boresight in the azimuth direction,

   ϵ = angular displacement in dV from the antenna boresight in the elevation direction,

α_b = half-power antenna beamwidth in the azimuth direction,

ε_b = half-power antenna beamwidth in the elevation direction,

ρ = dipole number density at the location of dV.

The fourth power appears in the integrand because the power gain becomes squared for a common transmitting/receiving antenna, and the power gain is the square of the pattern of Equation (54).

It is desirable to evaluate the integral in Equation (56) so as to display it as a function of range. If we choose a spherical coordinate system centered on the radar, the element of volume is

$$dV = R^2 \cos\varepsilon \, d\varepsilon \, d\alpha \qquad (57)$$

Restricting attention to the contributions from only those dipoles in a thin spherical shell of thickness ΔR, the return from that shell alone reduces to a surface integral,

$$P_r = P_t \frac{\lambda^2 G_o^2 \langle\bar{\sigma}\rangle}{(4\pi)^3} \frac{\Delta R}{R^2} \iint [f(p)f(q)]^4 \, \rho \cos\varepsilon \, d\varepsilon \, d\alpha \qquad (58)$$

where R is the range to the shell. The limits of integration should be set so as to include the contributing portions of the plume intercepted by the spherical shell. A scheme for establishing the limits will be described later in this section. Unfortunately, the integral in Equation (58) cannot be evaluated analytically.

It is instructive to explore Equation (58) for a simple case. To do so, we construct the coordinate system shown in Figure 21. The plume coordinate system (u,v,z) is angled with respect to the (x,y,z) system by an angle β, with the positive u direction being toward the dispensing aircraft. The origin of the plume coordinate system is fixed at the center of the plume. The plume length is designated by L and is determined by
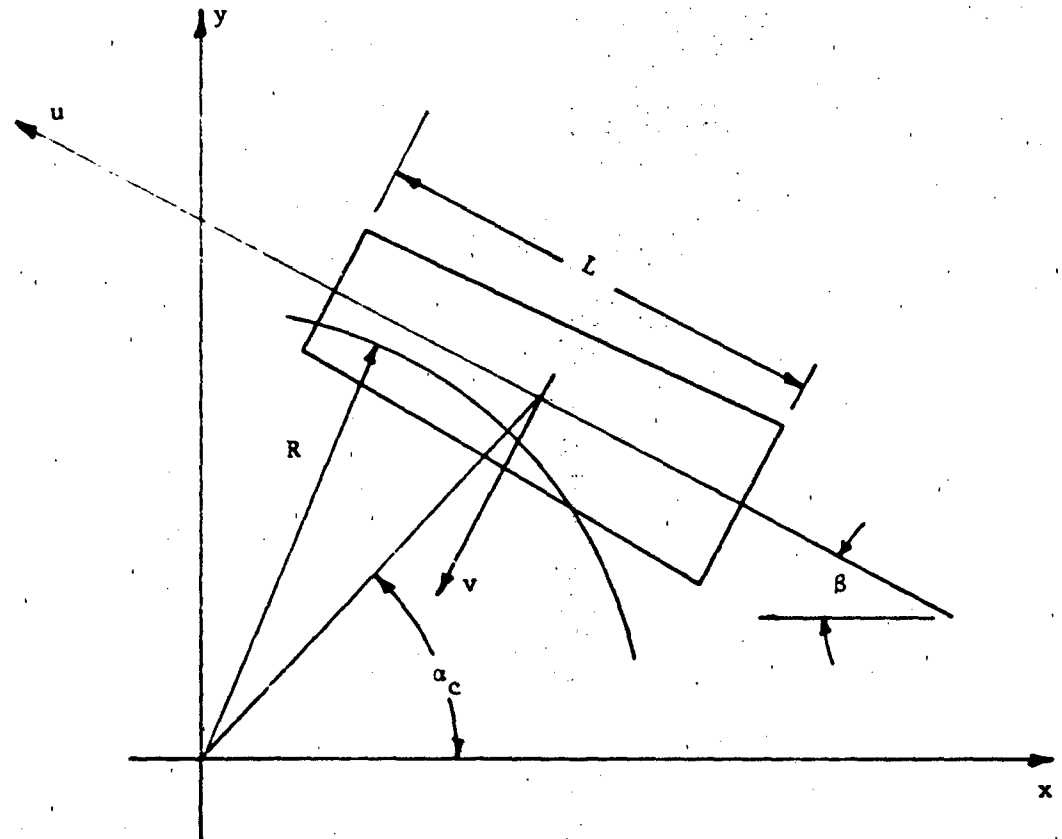
Figure 21. Plume geometry in two coordinate systems. The radar is at $x = y = 0$.

the duration of the seeding operation. For example, if it took one minute for an aircraft moving at 200 m/sec to deploy the chaff, the plume would be 12 km long.

The coordinates of the center of the plume are x_c, y_c, z_c

$$x_c = R_c \cos \epsilon_c \cos \alpha_c$$
$$y_c = R_c \cos \epsilon_c \sin \alpha_c \tag{59}$$
$$z_c = R_c \sin \epsilon_c$$

where R_c, ϵ_c, α_c are the slant range, elevation angle, and azimuth angle to the plume center as seen by the radar located at the origin of the x,y,z, system. The u,v,z system origin is at the plume center and the relationship between these two systems is

$$x = x_c - u \cos\beta - v \sin\beta$$
$$y = y_c + u \sin\beta - v \cos\beta \tag{60}$$

$$u = - (x - x_c) \cos\beta + (y - y_c) \sin\beta$$
$$v = - (x - x_c) \sin\beta - (y - y_c) \cos\beta \tag{61}$$

As viewed in the u,v,z system, the radar lies at u_0, v_0, 0, where

$$u_0 = R_c \cos \epsilon_0 \cos(\alpha_c + \beta)$$
$$v_0 = R_c \cos \epsilon_c \sin(\alpha_c + \beta)$$

Thus, if the slant range, elevation angle and azimuth angle (R,ϵ,α) are known for a point in space, the location of the point in both coordinate systems is

$$x = R \cos\epsilon \cos\alpha \qquad u = u_0 - R \cos(\alpha + \beta)$$
$$y = R \cos\epsilon \sin\alpha \qquad v = v_0 - R \cos\epsilon \sin(\alpha + \beta) \tag{62}$$
$$z = R \sin\epsilon \qquad z = R \sin\epsilon$$

We can calculate the dipole density distribution in a horizontal plane for any time we choose, and it is then a simple matter to plot the density as a function of the azimuth angle. Let us assume, therefore, that the radar is located 5 km to the side of the plume and at the same altitude as the plume axis, perhaps being mounted on a helicopter. Thus, $\epsilon = 0$, and we select $\beta = \pi/2$, $\alpha_c = 0$. Choosing a time $t = 10$ minutes fixes the origin of the (u,v,z) system at a distance $u_o = 120$ km for an aircraft velocity of 200 m/s. For a dispensing rate of 10^4 dipoles per second and an efficiency of 30%, the dipole concentrations along circular arcs in the horizontal plane are as shown in Figure 22.

For ranges less than 5 km, this circular trajectory never touches the plume axis where the density takes on its highest value. The path sweeps in close to the axis, then moves out again; hence, the density profiles exhibit a single peak value (dotted lines). For ranges greater than 5 km, the path crosses the plume axis twice; hence, these profiles have a characteristic double hump (solid lines). The dashed line shows the case when the circular trajectory grazes the plume axis (i.e., $R = v_o$). Note that for this particular time ($t = 10$ minutes), the maximum dipole concentration is slightly less than 10^{-3} dipoles per cubic meter.

As another example, consider a chaff cloud 1.7 km in altitude while the radar is on the ground. Maintaining a cross-track distance of 5 km places the plume axis 5.281 km from the radar as measured along the slant range; see Figure 23. The elevation angle to the plume axis is 18.78°.

Figure 24 is a display of the dipole concentration in a spherical shell 5.4 km in radius and centered on the radar. This shell is slightly larger than the nearest point on the plume axis, hence it intercepts the plume axis at two places. These are clearly visible in the figure. The display itself is of the contours of constant dipole concentration, plotted on a grid of
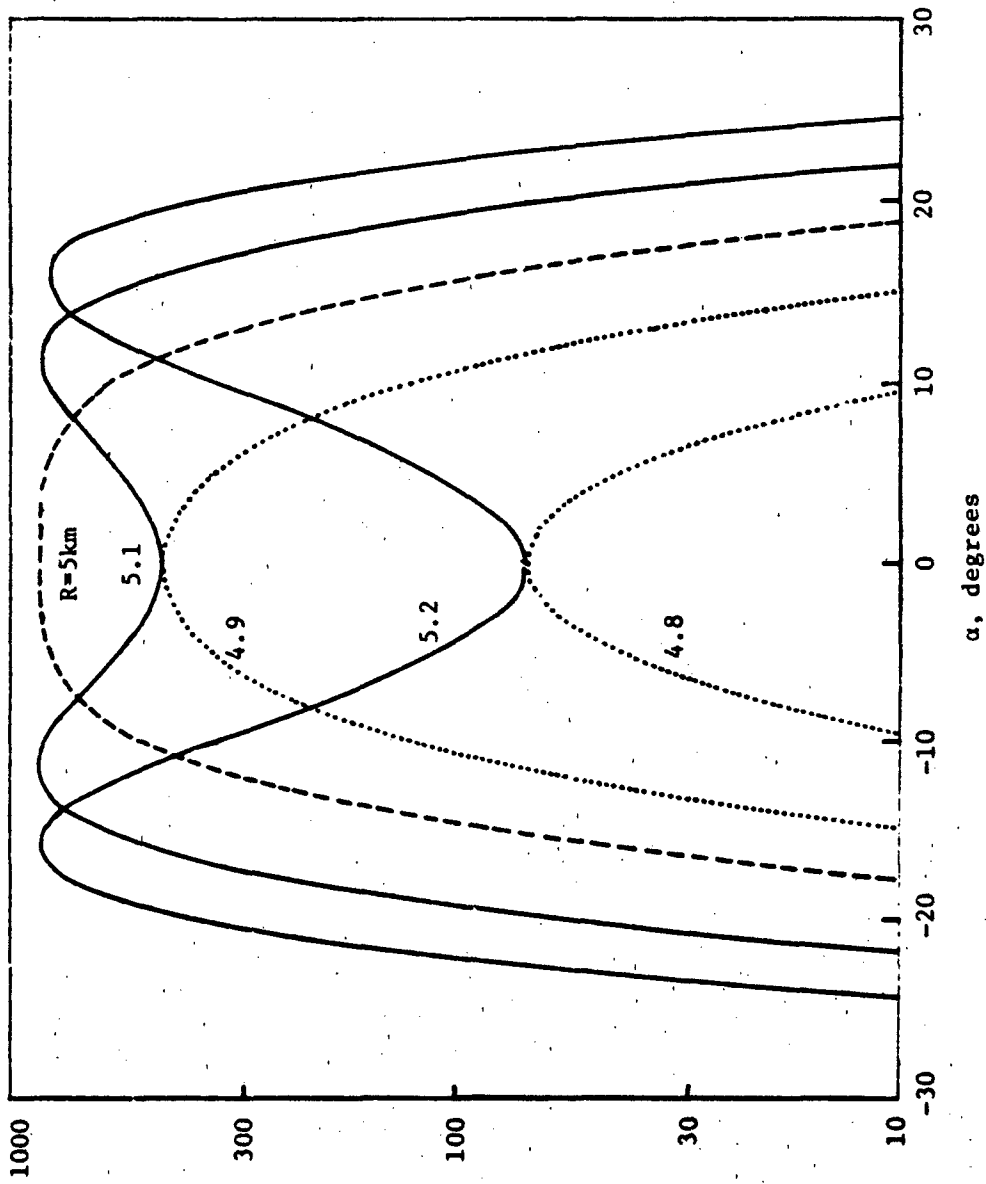
Figure 22. Dipole concentrations along spherical slices in a horizontal plane, with $\beta = \pi/2$.
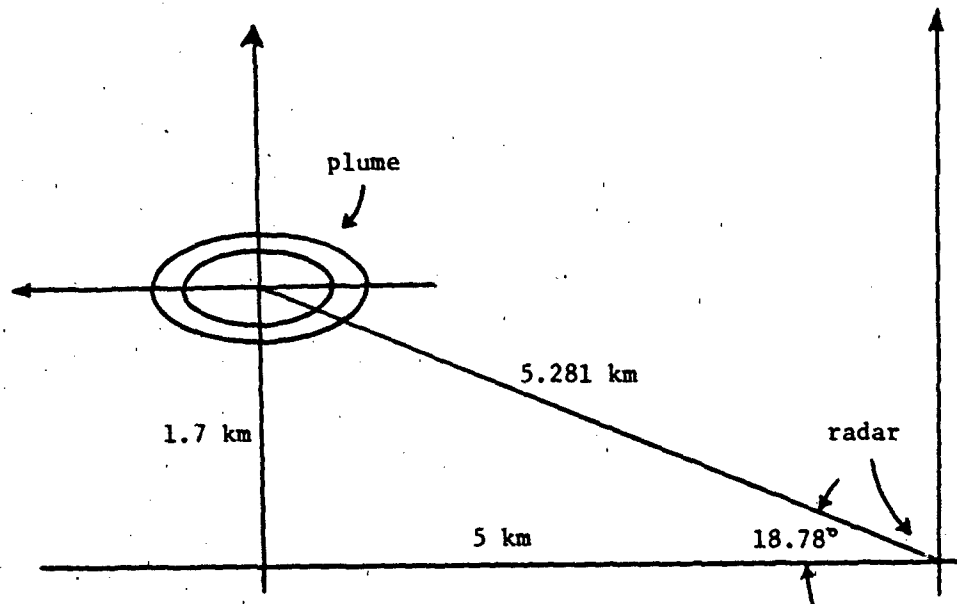
Figure 23. Elevation angle to the plume axis
is 18.78° as seen from the radar.
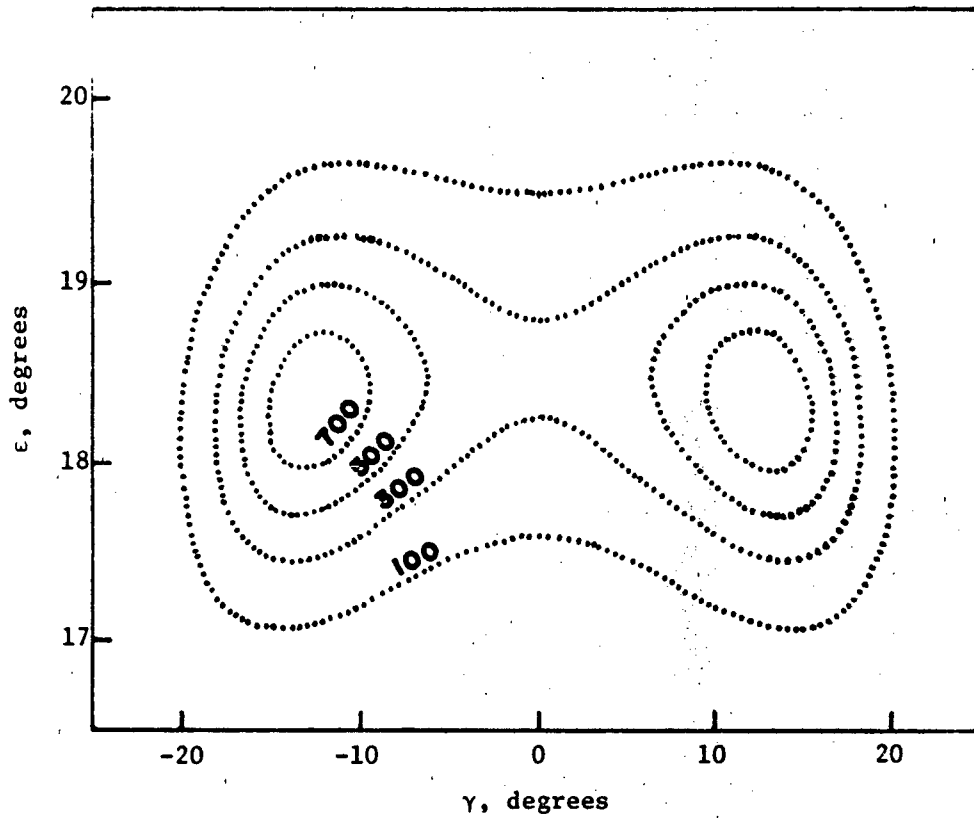
Figure 24. Dipole density distributions for a plume 1.7 km in altitude, taken along a spherical shell 5.4 km in radius. Contour labels are the dipole number density per million cubic meters.

elevation and azimuth angles. Note that the vertical scale has been expanded to a size ten times the horizontal scale, hence the actual distribution is of the order of 40 degrees wide, but only 3 degrees tall. Note that the maximum concentration occurs at an elevation angle near 18.35 degrees, somewhat lower than the 18.78 degrees shown in Figure 23. This is because the 18.78 degree angle is appropriate to a slightly smaller shell radius.

The function depicted by the contours in Figure 24 is the density function ρ in Equation (51). The other functions of importance are the antenna patterns $f(p)$ and $f(q)$. By way of illustration, Figure 25 shows a typical radiation pattern for an antenna with equal beamwidths in the azimuthal and elevation planes of 3 degrees. Shown there are the contours of equal intensity at the half-power level and for the first eight side-lobes. Note that the half-power level is 3 degrees wide in both planes, but that the pattern appears greatly elongated due to the difference between the horizontal and vertical scales. The scales were chosen to match those of Figure 24.

According to the prescription given in Equation (58), the square of the power pattern of Figure 25 must be multiplied by the number density pattern of Figure 24, and that product (when weighted by the cosine of the elevation angle) must be integrated over the solid angle subtended by the chaff cloud. It should be appreciated, however, that the representative patterns may be shifted away from each other by a considerable angle. It should also be appreciated that the pattern of Figure 24 changes its character with range.

Turning now to the limits of integration of Equation (58), we may establish plume boundaries such that the dipole concentration in any transverse plane is some specifiable fraction of the axial density. A convenient boundary is that where the density has dropped to 1% of its axial value, corresponding to 3.035 standard deviations, and within this boundary lie 99.73% of the dipoles. The surface satisfies the equation
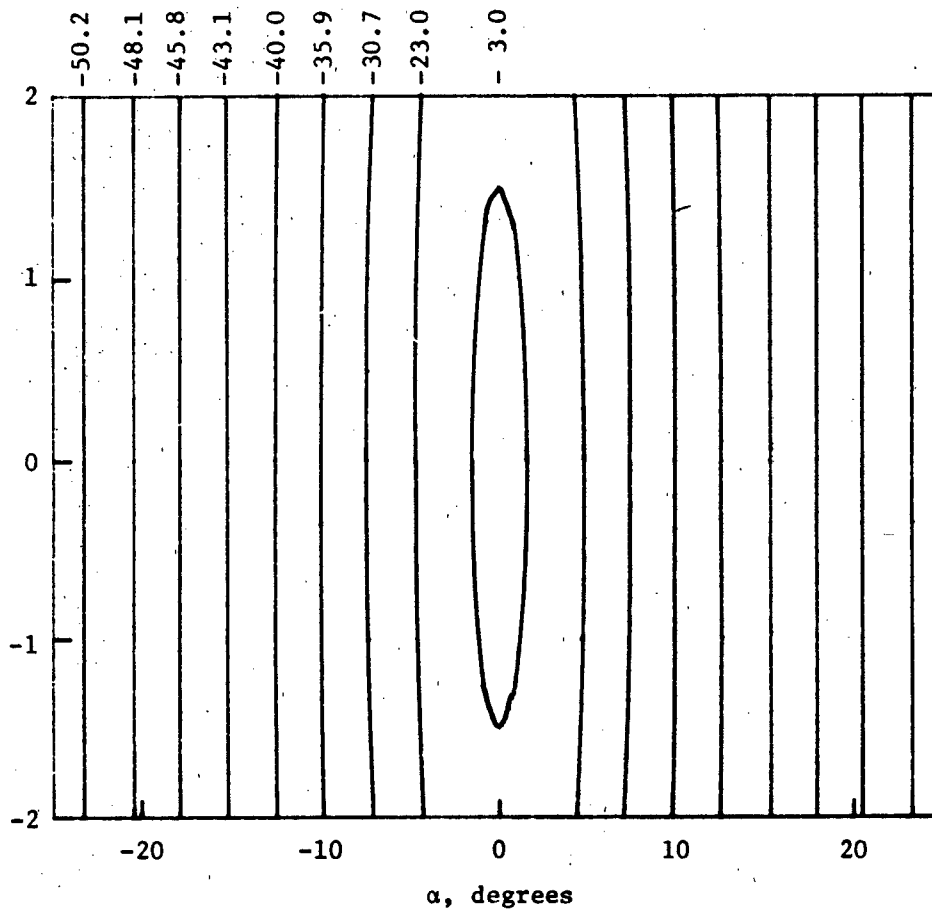
Figure 25.   A representation of the radiation pattern of an antenna with a beamwidth of 3 degrees.   The central ellipse is the contour of the half-power level and the remaining contours are the sidelobe levels.   Nulls in the pattern are not shown.

$$\frac{v^2}{\ell_v} + \frac{(z - z^2)}{\ell_z} = -2u \ \ell n \ .01 \tag{63}$$

which is the equation of an elliptical cone. The limits of integration may be established by finding the intersection of this cone with a sphere of radius R, yielding contours in space which may resemble those of Figure 24. The mathematical description of the contours is couched in a quartic equation which must be expressed in terms of azimuth and elevation. Partial derivatives with respect to azimuth and elevation must be formed and forced to zero, finally leading to the establishment of the limits.

The mathematical complications of such a procedure outstrip, by far, the detail needed for a practical implementation. Thus we will make some simple approximations. First, the elliptical cone axis will be assumed horizontal. The inclination of the cone axis to the horizontal is $\dot{z}/\dot{u}$ (the ratio of the dipole fall rate to the aircraft velocity) and amounts to only a fraction of a degree. Second, the cone is a very slender one and we can approximate it with an elliptic cylinder. The slenderness can be appreciated from inspection of Table 5, which lists the transverse distance from the cone axis to the point where the dipole density has fallen to 1% of its axial value. Over a length of 12 km, the width of the plume changes by scarcely 26 meters from one end to the other, and its thickness changes by barely 16 meters.

TABLE 5. TRANSVERSE PLUME DIMENSIONS
FOR t = 10 minutes

u, k_m	v, m	$z - z_c, m$
-6	271.446	169.655
0	278.149	173.844
6	284.694	177.935

67

Establishing the limits of integration in the elevation plane would require that we find the planes tangent to the elliptic cylinder at its upper and lower surfaces, and containing the radar. The lines of tangency do not, in general, lie at positions where $v = 0$, but for small elevation angles, v is small at the tangent line. Thus, we shall assume that the limits of integration in the elevation angle can be found with acceptable accuracy by setting $z - z_c = \pm 3.035 \, \sigma_z$ and $v = 0$.

Conceptually, therefore, we can imagine four parallel lines in space passing through the top, bottom and sides of the plume at its midpoint, and being parallel to the u-axis. These four lines may or may not pierce a sphere of arbitrary radius. If a line does pierce the sphere, it does so at two points, but the points may not necessarily lie within the finite length of the plume.

Considering first the azimuthal limits, we select the lines at the sides of the cylinder where $z = z_c$ and $v = \pm 3.035 \, \sigma_v$. We may now use the relationships in Equation (62) to find the u coordinates where these two lines pierce the sphere of constant radius. That is, we obtain the quadratic equation

$$R^2 = (u - u_o)^2 + (v - v_o)^2 + z^2 \qquad (64)$$

which can be solved for any of the three variables on the right side, provided the remaining pair are held fixed in value.

The solution of Equation (64) for constant v and z is

$$u = u_o \pm \left[(R^2 - z^2) - (v - v_o)^2 \right]^{1/2} \qquad (65)$$

The two lines $v = v_1$, v_2 (for $z = z_c$) yield four solutions which will be identified with subscripts:

$$u_1 = u_o - \left[(R^2 - z_c{}^2) - (v_1 - v_o)^2 \right]^{1/2}$$

$$u_2 = u_o + \left[(R^2 - z_c{}^2) - (v_1 - v_o)^2 \right]^{1/2} \qquad (66)$$

$$u_3 = u_o - \left[(R^2 - z_c{}^2) - (v_2 - v_o)^2 \right]^{1/2}$$

$$u_4 = u_o + \left[(R^2 - z_c{}^2) - (v_2 - v_o)^2 \right]^{1/2}$$

The solutions Equation (66) may not lie on the finite elliptic cylinder, in which case the sphere intersects one or both ends of the cylinder. It turns out there are 22 possible combinations, including those where there is no intersection at all. The lack of an intersection is signified by a negative number in the radicals of Equation (66).

For those cases where the spherical shell intersects the end of the cylinder, we may insert $u = \pm L/2$ into Equation (64) and solve it for v. The general solution is

$$v = v_o \pm \left[(R^2 - z^2) - (u - u_o)^2 \right]^{1/2} \qquad (67)$$

which gives two roots, of which only one is the required one. One of the roots will be much smaller in absolute value than the other, and this is the desired one. In fact, the desired root must lie in the range $v_1 < v < v_2$, or else the sphere would not have intersected the end of the cylinder. We designate the desired solutions as v_3 for $u = - L/2$, and v_4 for $u = L/2$.

It is possible for the sphere to intercept two separate regions of the plume, as suggested by Figure 24, and the solid angle integral may cover two disjointed patches. This occurs in four of the 22 possible cases. The coordinates of the endpoints of the azimuthal integration are listed in Table 6. Note that there are four cases (#4, #5, #8, #9) for which the integration interval is split into two discrete regions. The coordinates can be used to establish the azimuth angle via the use of Equations (62). That is, if u and v are specific coordinates listed in

TABLE 6. COORDINATES TO BE USED TO DETERMINE LIMITS
IN AZIMUTHAL INTEGRATION

Case	u_1	u_2	u_3	u_4	Intersection Coordinates			
1	1	1	1	1	no integration			
2	1	1	1	2	(u_4,v_2)	$(0,v_3)$		
3	1	2	1	2	(u_4,v_2)	(u_2,v_1)		
4	2	2	1	2	(u_4,v_2)	(u_2,v_1)	(u_1,v_1)	$(0,v_3)$
5	2	2	2	2	(u_4,v_2)	(u_2,v_1)	(u_1,v_1)	$(u_3,v_2)0$
6	1	1	1	3	(L,v_4)	$(0,v_3)$		
7	1	2	1	3	(L,v_4)	(u_2,v_1)		
8	2	2	1	3	(L,v_4)	(u_2,v_1)	(u_1,v_1)	$(0,v_3)$
9	2	2	2	3	(L,v_4)	(u_2,v_1)	(u_1,v_1)	(u_3,v_2)
10	1	3	1	3	no integration			
11	2	3	1	3		(u_1,v_1)		$(0,v_3)$
12	2	3	2	3		(u_1,v_1)		(u_3,v_2)
13	3	3	1	3		(L,v_4)		$(0,v_2)$
14	3	3	2	3		(L,v_4)		(J,v_3)
15	3	3	3	3	no integration			
16	4	4	1	1	no integration			
17	4	4	1	2	(u_4,v_2)	$0,v_3$		
18	4	4	2	2	(u_4,v_2)	(u_3,v_2)		
19	4	4	1	3	(u_4,v_2)	(u_3,v_2)		
20	4	4	2	3	(L,v_4)	$(0,v_3)$		
21	4	4	3	3	no integration			
22	4	4	4	4	no integration			

Test Conditions:

1. $u < -L/2$
2. $-L/2 < u < L/2$
3. $u > L/2$
4. no solution

Table 6, the azimuth angle can be computed from

$$\alpha = \text{arc tan} \left\{ \frac{v_o - v}{u_o - u} \right\} - \beta \qquad (68)$$

The limits of integration in the elevation plane are easy to establish. Given an altitude and a range, the final formats (for z) of Equations (62) can be used. The upper and lower limits are, respectively,

$$\epsilon_2 = \text{arc sin} \frac{z_c + 3.035 \; \sigma}{R}$$

$$\epsilon_1 = \text{arc sin} \frac{z_c - 3.035 \; \sigma_z}{R} \qquad (69)$$

SECTION 6
CHAFF DATA ANALYSIS

As has been seen from the discussion of the dipole concentration variation within the cloud, the net received signal depends not only on the dipole number density, but also upon the radar antenna pattern and how this pattern is oriented with respect to the cloud. Deconvolving the signal in an effort to deduce the dipole distribution is not an easy task, but a limited analysis of one test run was performed with that in mind.

The Office of Missile Electronic Warfare of White Sands Missile Range released the results of a test run for analysis purposes. Designated as Experiment LC-38, which was conducted on 15 April 1980, the test was not primarily for the purpose of cloud mapping, yet the radar operators slewed the antenna at various times in a coarse attempt at cloud mapping. Had the cloud been scanned systematically, and had we had more specific information about the test conditions, the analysis could have been more detailed.

Because the radar return from chaff is a result of a random process (the dipole motion), a sample at any time is a random variable. To estimate the average RCS per resolution cell with moderate error, we need at least eight independent samples. The chaff return decorrelation time -- the time interval between independent samples -- is of the order of 10 to 20 milliseconds at 10 GHz. Thus, typically 1 to 2 seconds' of data should be collected for each data point on the spatial distribution curves. But occasionally there were only two samples of the signal for a fixed range and antenna boresight direction, and a single datum based on the samples is not statistically significant. Nevertheless, such data were included in the analysis, even though they tend to inject irregularities into the plotted distributions.

The relationship between the cloud and the radar is known only in terms of the azimuth and elevation angles off the antenna boresight and the range. For the purpose of analyzing spatial dipole distributions, two of these coordinates should remain fixed while the third varies. In scanning a printout of the measurements, we identified seven data sets in which only the azimuth angle varied, two in which only the elevation angle varied and five in which only the range varied. Using these fourteen data sets, we attempted to determine the spatial distributions in azimuth, elevation, and range.

Prelir ary examination of the measured data revealed a skewness in the distributions, and two generalized forms were postulated that could include or account for the skewness. These are

$$\hat{y}_1(x) = c_{11} \, x^{c_{21}} \, \exp(c_{31}x) \qquad x \geq 0 \tag{70}$$

$$\hat{y}_2(x) = c_{12} \, x^{c_{22}} \, \exp(c_{32}x^2) \qquad x \geq 0 \tag{71}$$

where $\hat{y}_1(x)$ is a generic gamma density function [9] and $\hat{y}_2(x)$ is a generic Nakagami density function [10]. Normalized parametric equations corresponding to $\hat{y}_1$ and $\hat{y}_2$ are

$$\hat{y}_1(x) = \frac{k}{(k-1)!} \, (kx/b)^{k-1} \, \exp(-kx/b) \tag{72}$$

$$\hat{y}_2(x) = \frac{2\sqrt{m}}{(m-1)!} \, (mx^2/a^2)^{m-\frac{1}{2}} \, \exp(-mx^2/a^2) \tag{73}$$

where

b   = expected value of x,

k   = b^2 divided by the variance of x,

a^2 =   expected value of x^2,

Γ =   the gamma function.

Families of plots of these two functions are shown in Figures 26 and 27. The parameters k and m are measures of the skewness of the two families, with progressively smaller values generating progressively larger skewness. To fit the skewness in the negative direction displayed by the measured azimuth and range data, we must reflect the curves about the axis x = 0, which is equivalent to the replacement of the independent variable by its negative. The functions $\hat{y}_1$ and $\hat{y}_2$ will be called the skewed exponential and the skewed normal functions, respectively.

To determine the parameters that best fit the measured distributions, we utilized the generalized linear regression formula

$$\hat{z} = a_0 + a_1 u + a_2 v \tag{74}$$

where $\hat{z}$ is the estimate, u and v are functions of the independent variable, and a_0, a_1, and a_2 are parameters that minimize the mean square error,

$$\overline{\epsilon}^2 = \frac{1}{N} \sum_{i=1}^{N} (z_i - \hat{z}_i)^2 \tag{75}$$

where the sample z_i is a function of the dependent variable (i.e., the received signal or the hCS).

Equation (75) is minimized by the substitution of Equation (74) for z_i and then the formation of the partial derivatives with respect to a_0, a_1, and a_2. Forcing these derivatives to zero generates a system of three equations whose solution gives the relationships needed for the minimization of Equation (75). The relationships are summarized in Table 7.
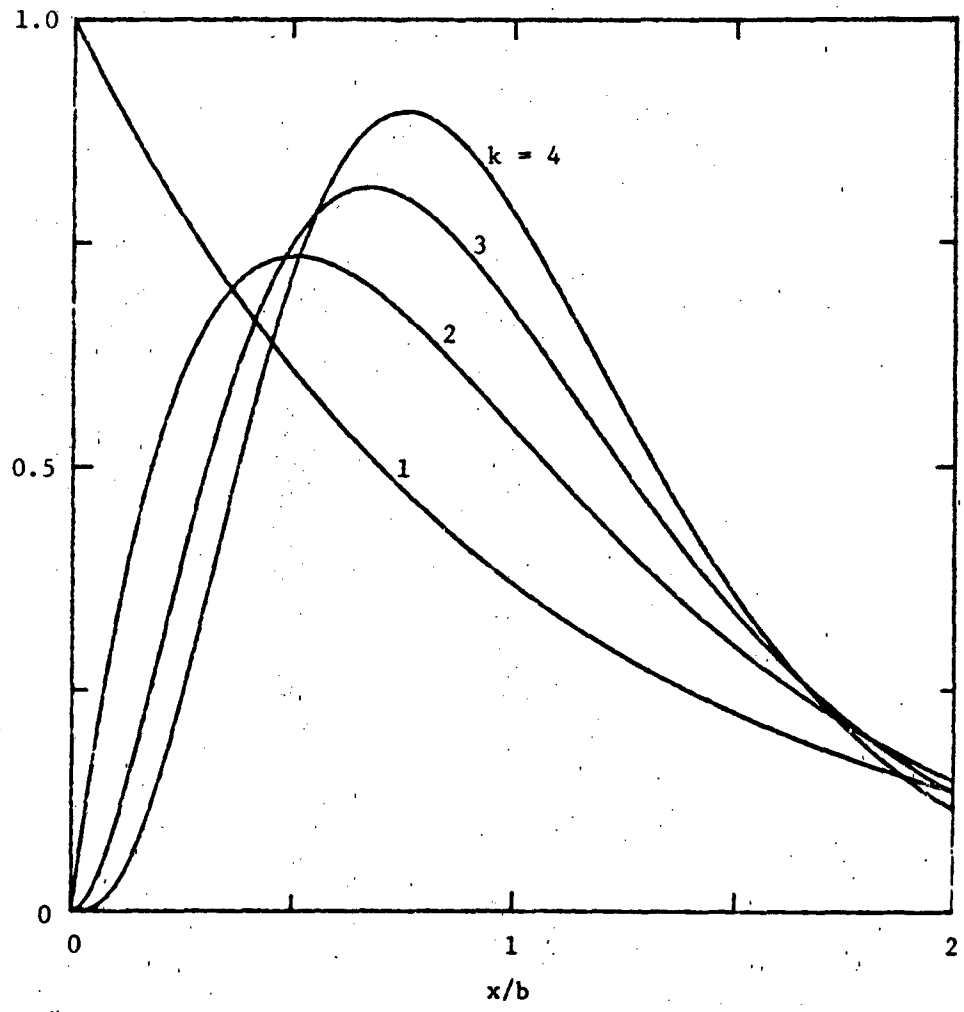
Figure 26. The skewed exponential distribution.
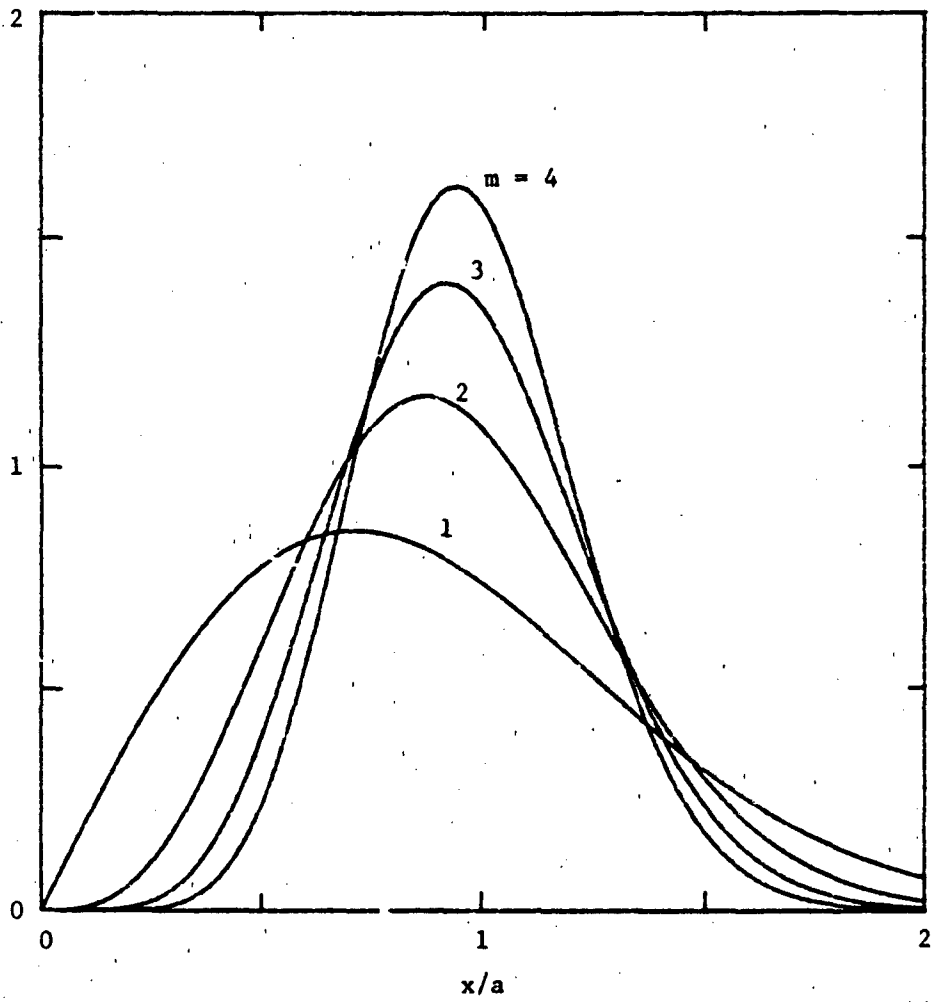
Figure 27. The skewed normal distribution.

TABLE 7.   CURVE FITTING PARAMETERS

Quantity	Skewed Exponential	Skewed Normal
z	$\ln y$	$\ln y$
$\hat{z}$	$\ln \hat{y}$	$\ln \hat{y}$
a_o	$\ln C_{11}$	$\ln C_{12}$
a_1	C_{21}	C_{22}
a_2	C_{31}	C_{32}
u	$\ln x$	$\ln x$
v	x	x^2

Programs that compute the optimum regression coefficients (the C's) for these two kinds of distributions were devised for a programmable hand calculator. The programs also compute a normalized correlation coefficient R^2, which is a measure of the "goodness of fit" between the estimate $\hat{y}$ and the measurement of y. A perfect fit is registered when $R^2 = 1$.

The measurements used by Georgia Tech in the analysis were summarized in a data printout nearly two inches thick. Each record contained a header that listed the azimuth angle, elevation angle, and range, and the returns were given for two different pulses a hundred pulses apart. The returns for these two pulses were split into the contributions from 15 range bins, and the arithmetic sum of the 15 contributions was listed in a final column in the record. For the distribution in azimuth and elevation, it was this "sum" column that was used as the dependent RCS value.

Measured and fitted distributions are shown in Figures 28 through 34 for the azimuthal variation, for which the range and the elevation angle remained fixed. The solid data points represent the average value of the "sum" column for as many pulses as occurred within an azimuth "window" 0.1 degree wide. Occasionally there were only two such pulses (the two in a single record) because the azimuth angle remained within the window only for that record; the circled data points signify this event. The number of pulses used to form the datum points represented by the uncircled points was typically four or more.

These plots show that the signal distributions are skewed, with higher tails in the direction of smaller azimuth angles. The measured data do not always trace out smooth curves, and the irregularity is due, in part, to the sparseness of the sampling represented by the circled data. Had we had access to magnetic tapes containing all the data (instead of every hundredth pulse), the distributions probably would have been smoother. Although such detailed information would have required several orders of magnitude more processing, that effort could have been handled easily by a computer. As it was, the limited data available had to be manually keyed into a hand calculator.

Fitting the distributions given by Equations (72) and (73) required some judgment as to where to set the origin, since these equations require that $x \geq 0$. Apparently this judgment was not quite so good in some cases as it was in others; for example, the representations in Figures 28, 33, and 34 show the peak of the fitted equation shifted somewhat from the peak suggested by the measured data. The amplitudes in these three figures are also somewhat lower than the measured data. On the other hand, Figures 29, 30, 31, and 33 show reasonably good fits. For all figures except Figure 30, the amplitudes of the returns exceed 100 m^2.

Both distributions given by Equations (72) and (73) were used in the linear regression analysis and the one having the
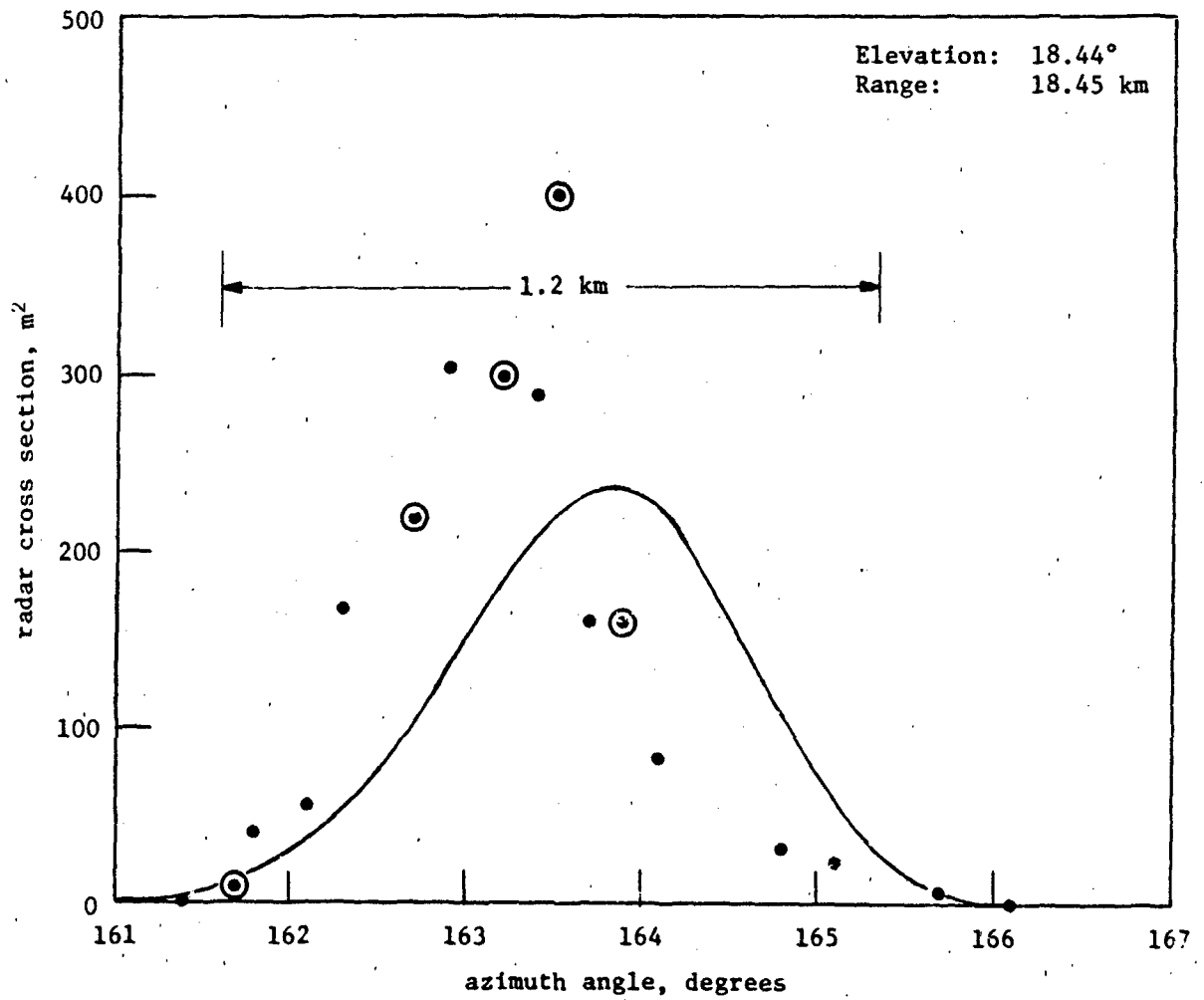
Figure 28. Distribution of radar return in azimuth for records 57-123.
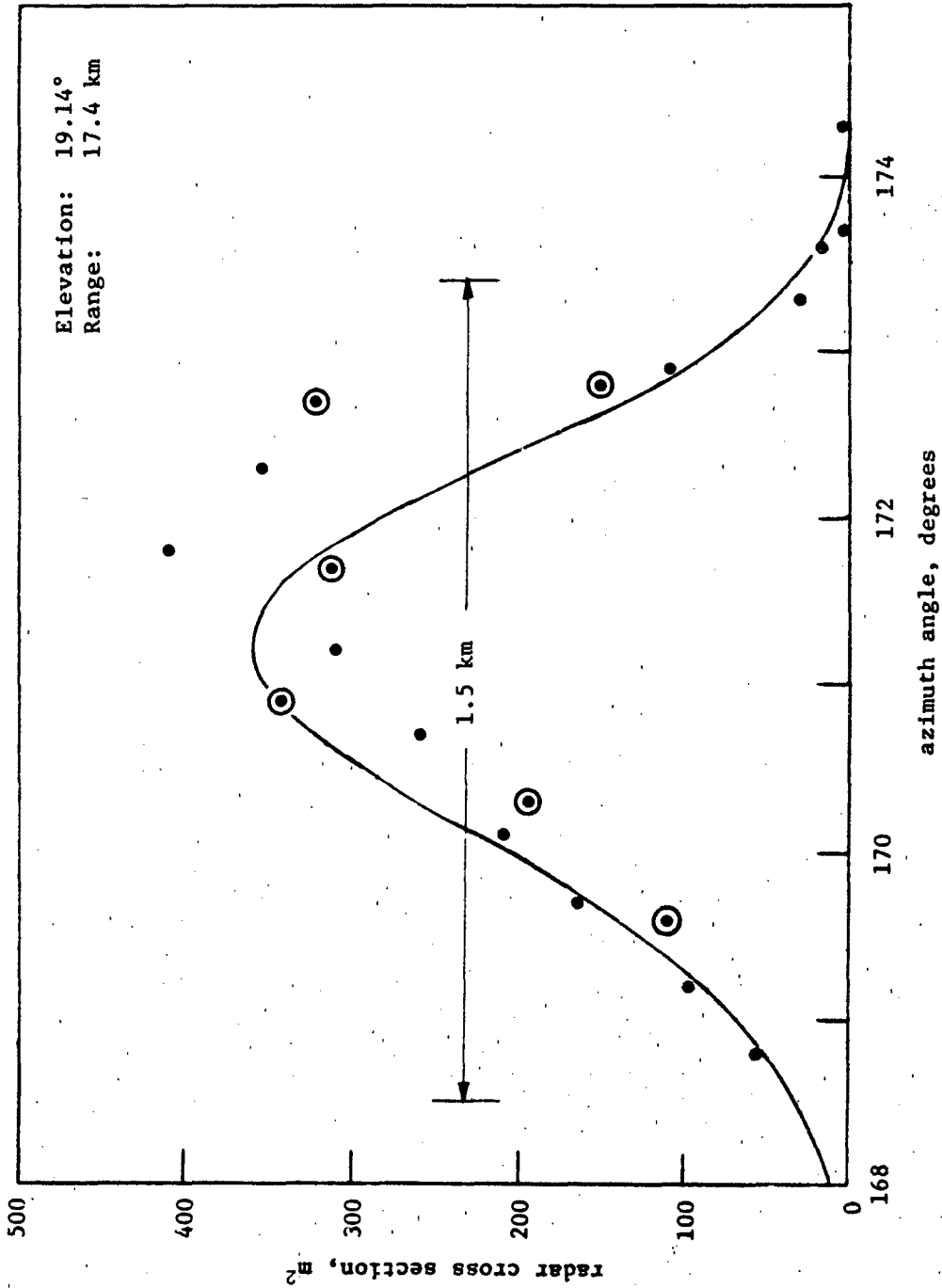
Figure 29. Distribution of radar return in azimuth for records 308-365.
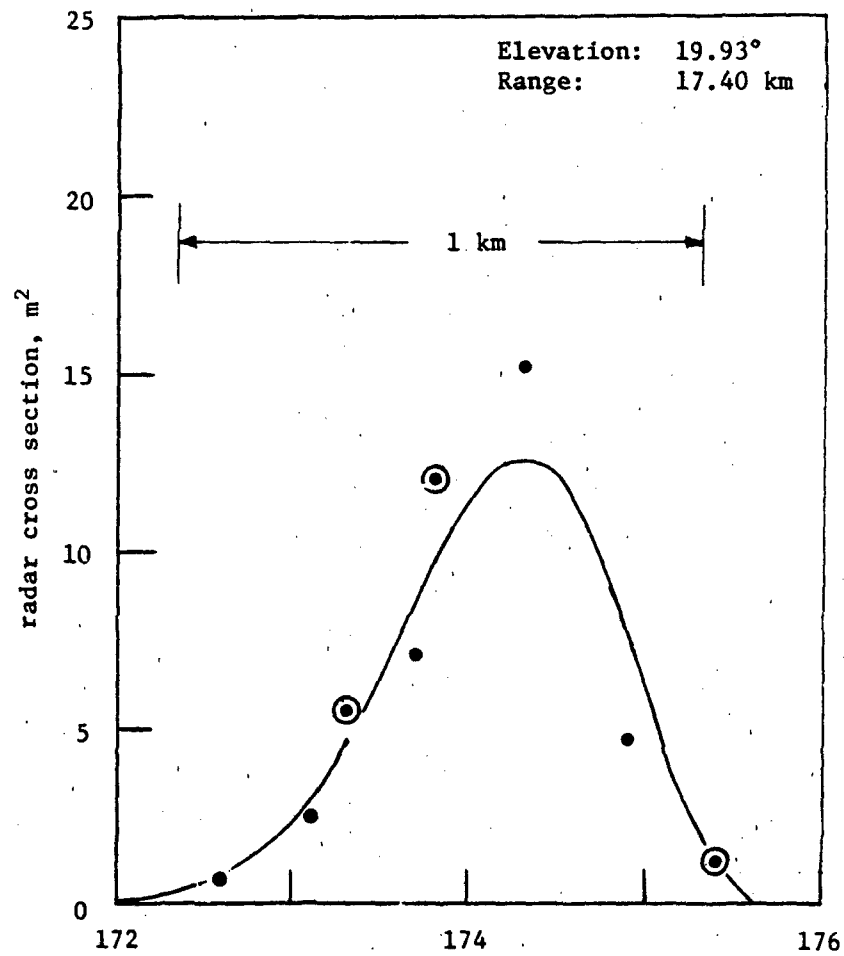
Figure 30. Distribution of radar return in azimuth for records 410-439.
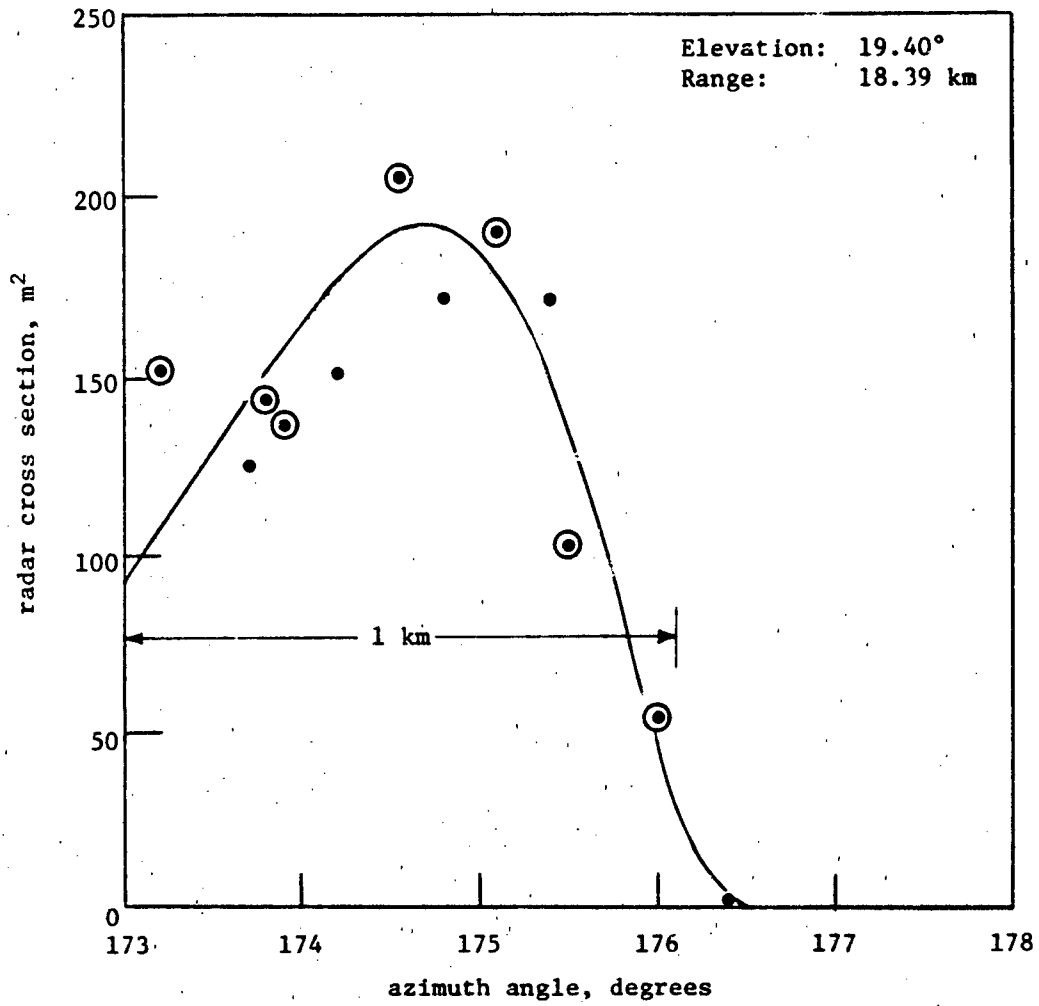
Figure 31. Distribution of radar return in azimuth for records 498-525.
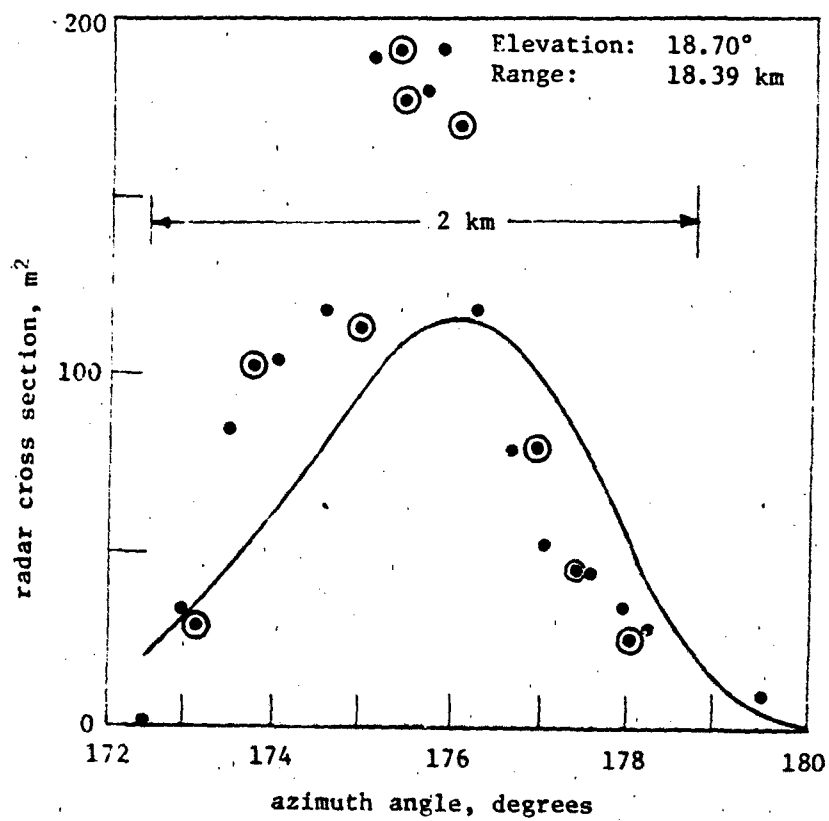
Figure 32. Distribution of radar return in azimuth for records 582-670.
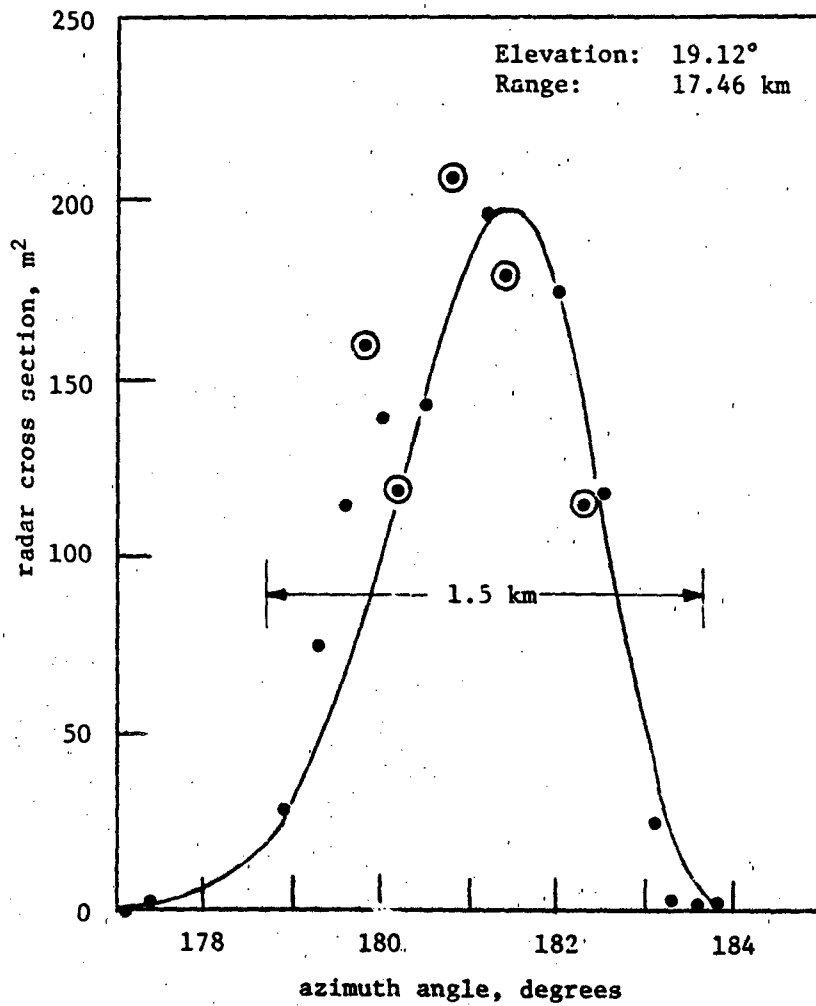
Figure 53. Distribution of radar return in azimuth for records 745-811.
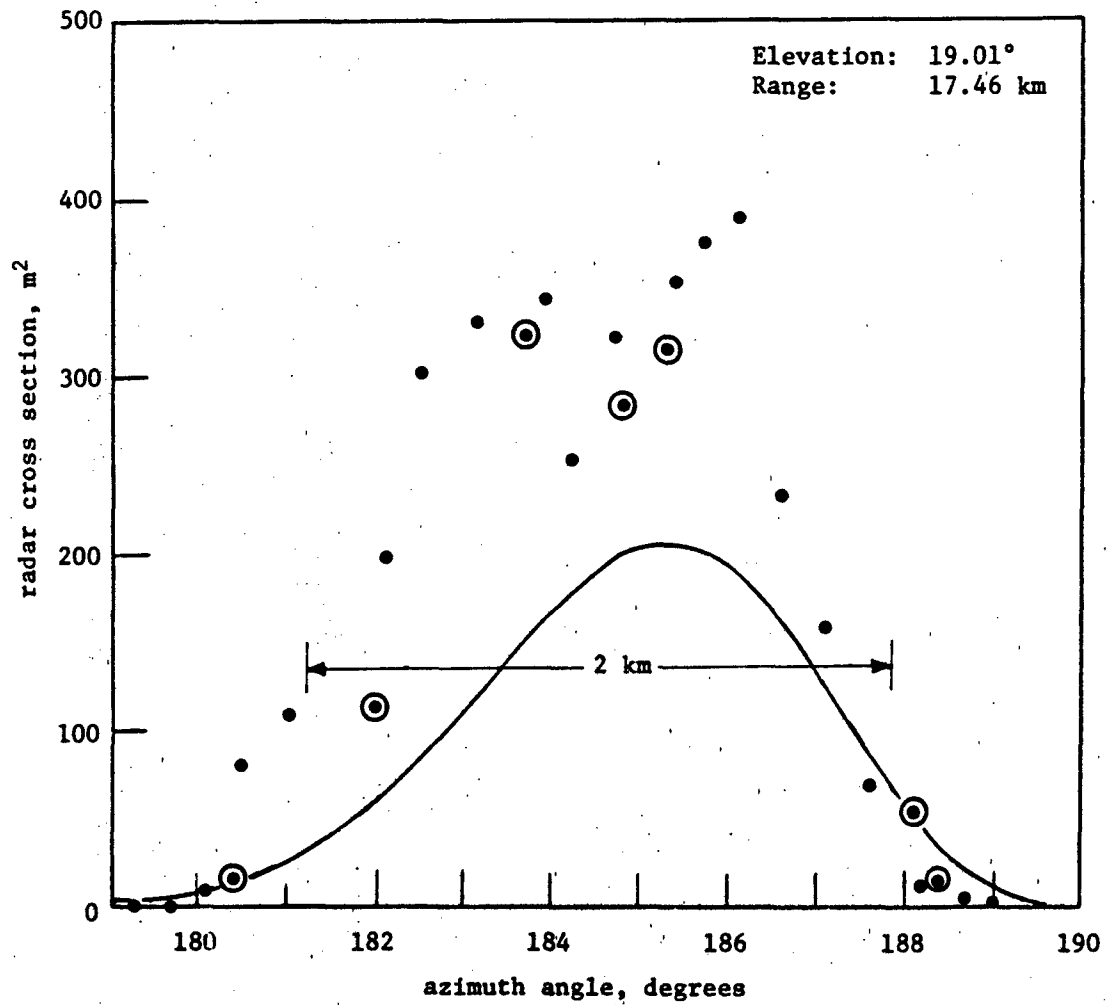
Figure 34. Distribution of radar return in azimuth for records 920-1000.

better fit was chosen and plotted in Figures 28 through 34. The "better" fit was determined by a comparison of the normalized correlation coefficient, which is listed in Table 8 for the azimuth data along with several other statistical values, namely the RMS error of the estimate expressed in square meters and as a percentage. Note that the skewed normal distribution yielded the better correlation for all the azimuth data, except for those in Figure 31, for which the skewed exponential is a better fit.

The spread listed for these data sets indicates the cross range distance covered by that particular set of data; it was computed from the azimuth angle change and the range. Note that the spread ranges from less than a km to more than 3.5 km, but this should not be construed to represent the cloud size in the cross range direction. The actual size is not known because its orientation with respect to the antenna beam is not known.

Very little data were available to conduct this kind of analysis in the elevation plane. Only two sets were found for which the azimuth angle and the range were held fixed while the elevation angle was varied. These data are plotted in Figures 35 and 36, and the information is quite sparse. All of these data points were the averages of only two samples (two pulses) spaced 100 pulses apart. Figures 35 and 36 consist of only 5 and 4 measurements, respectively.

Despite the paucity of elevation plane data, the distributions fit a positive skew, in contrast to the negative skew noted in the azimuth variations. Nevertheless, the sense of direction is unimportant because angular changes can be measured in either direction. As mentioned earlier, the thickness of the cloud is much less in the vertical direction than the horizontal, and Figures 35 and 36 tend to verify this.

The statistical data for the two elevation angle variations are summarized in Table 9. For both runs, the skewed normal distribution represents the better fit. Note for the data in Figure 36 that the correlation coefficient is close to unity,

TABLE 8.   SUMMARY OF STATISTICAL DATA FOR THE
AZIMUTH VARIATIONS

Figure No.	28	29	30	31	32	33	34
Elevation angle	18.44	19.14	19.93	19.40	18.70	19.12	19.01
Range (km)	18.45	17.40	17.40	18.39	18.39	17.46	17.46
Spread (km)	1.67	2.01	0.84	1.02	2.56	2.11	3.52
R_1^2	0.783	0.893	0.896	0.982	0.758	0.772	0.505
RMS error, m	90	59	2	22	49	49	141
% error	49	27	29	15	48	42	71
R_2^2	0.852	0.909	0.957	0.958	0.816	0.911	0.666
RMS error, m	81	62	2	30	42	25	109
% error	44	28	20	21	41	22	55
k	14.3	11.4	5.1	3.5	5.4	5.0	5.2
m	4.6	3.8	1.7	1.5	2.1	1.8	2.2
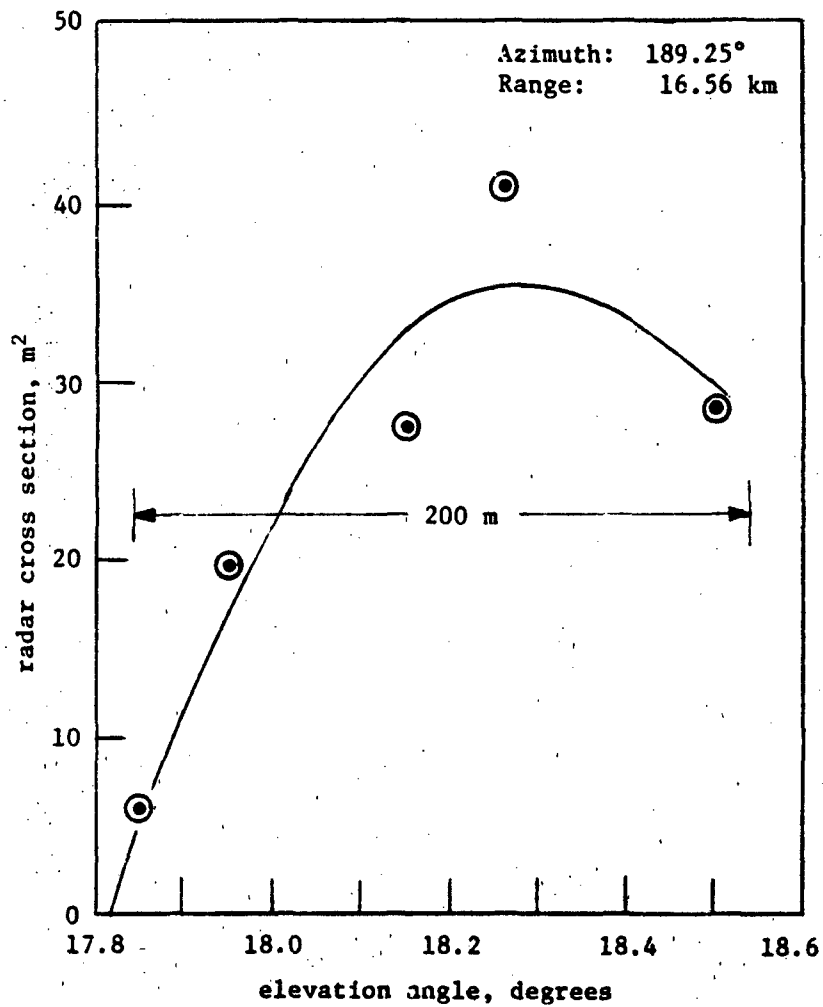
Figure 35. Distribution of radar return in elevation
for records 1188-1203.
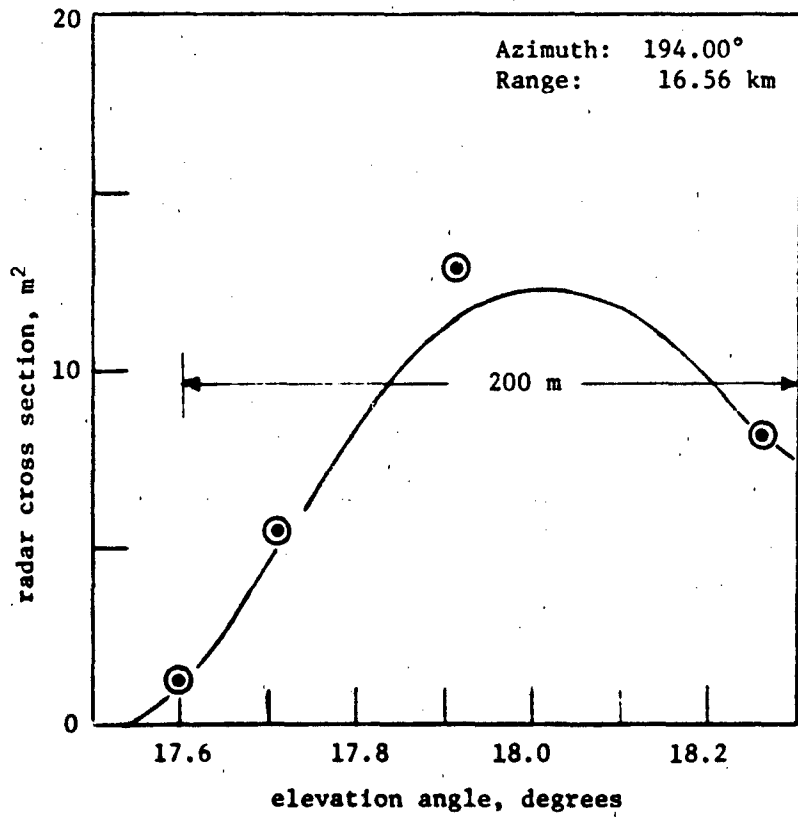
Figure 36. Distribution of radar return in elevation
            for records 1283-1289.

indicating a very good fit. This is due in part to the sparseness of the data, there being only four points to "run the curve" through.

TABLE 9.   SUMMARY OF STATISTICAL DATA FOR
THE ELEVATION VARIATIONS

Figure	35	36
Azimuth angle	189.25	194.00
Range, km	16.56	16.56
Spread, m	184	197
R_1^2	0.972	0.986
RMS, error, m	3.8	1.0
% error	14	12
R_2^2	0.974	0.997
RMS error, m	2.4	0.5
% error	9	6
k	2.15	3.22
m	0.95	1.35

Turning now to the radar returns as functions of range while azimuth and elevation remained fixed, it is convenient to plot the results as a function of the range gate number instead of the actual range. This has been done in Figures 37 through 41 (five data sets); each datum in these plots is an average of 6 samples (2 samples for each of 3 successive records). The gate width is
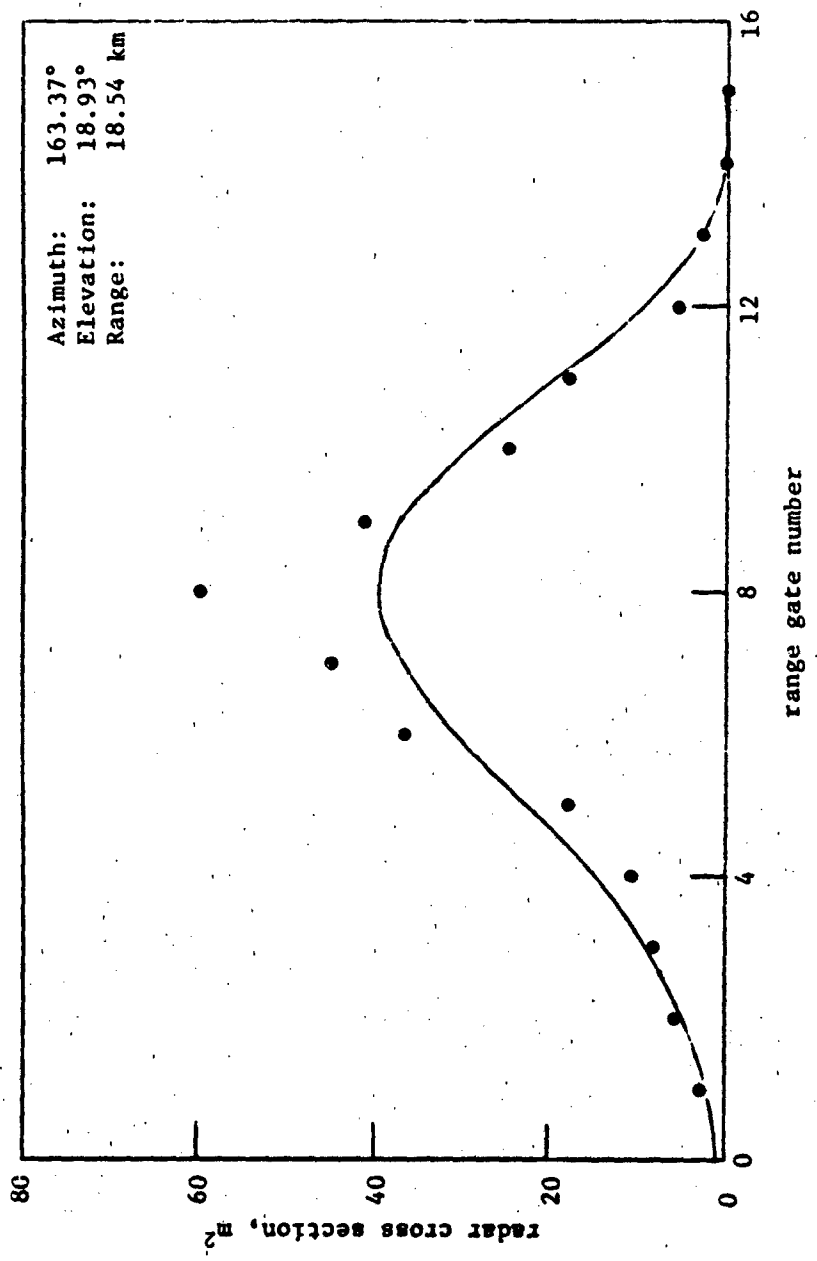
Figure 37. Distribution of radar return in range for records 92-94.
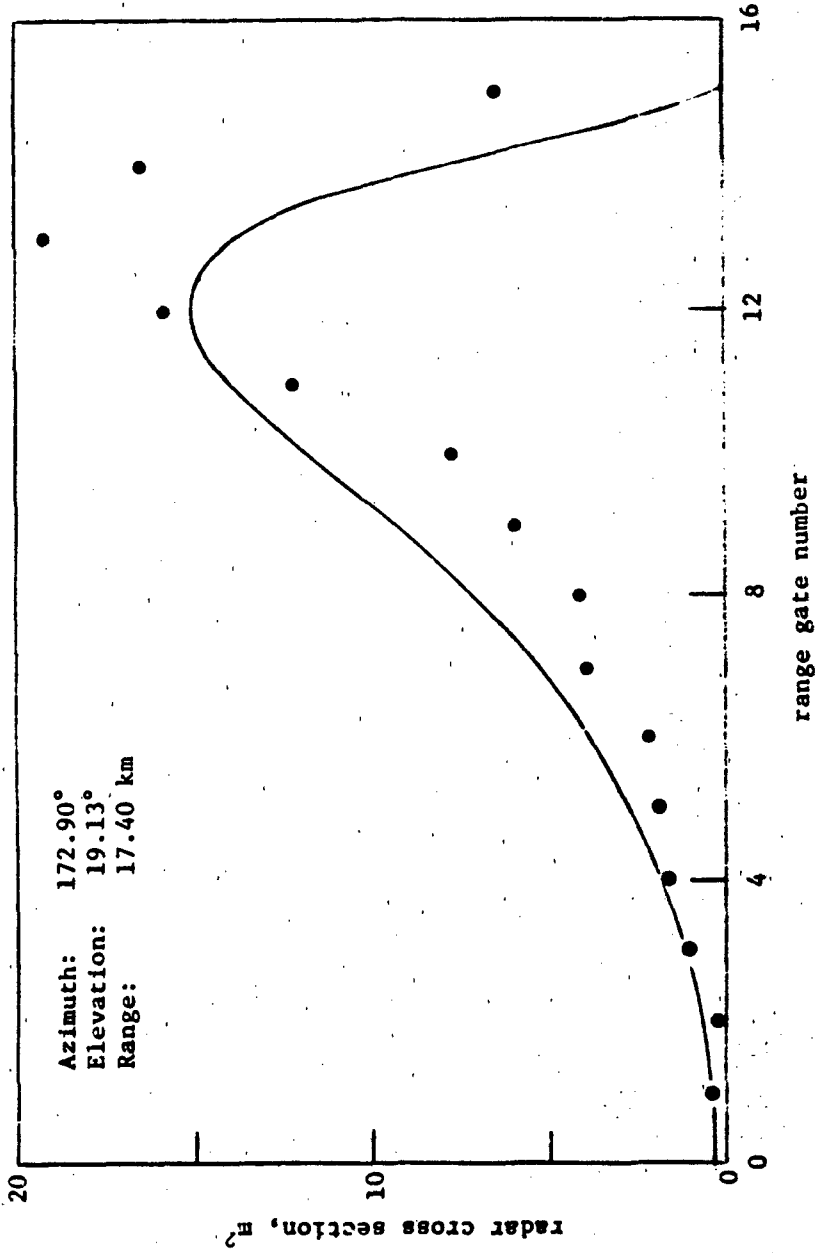
Figure 38. Distribution of radar return in range for records 348-350.
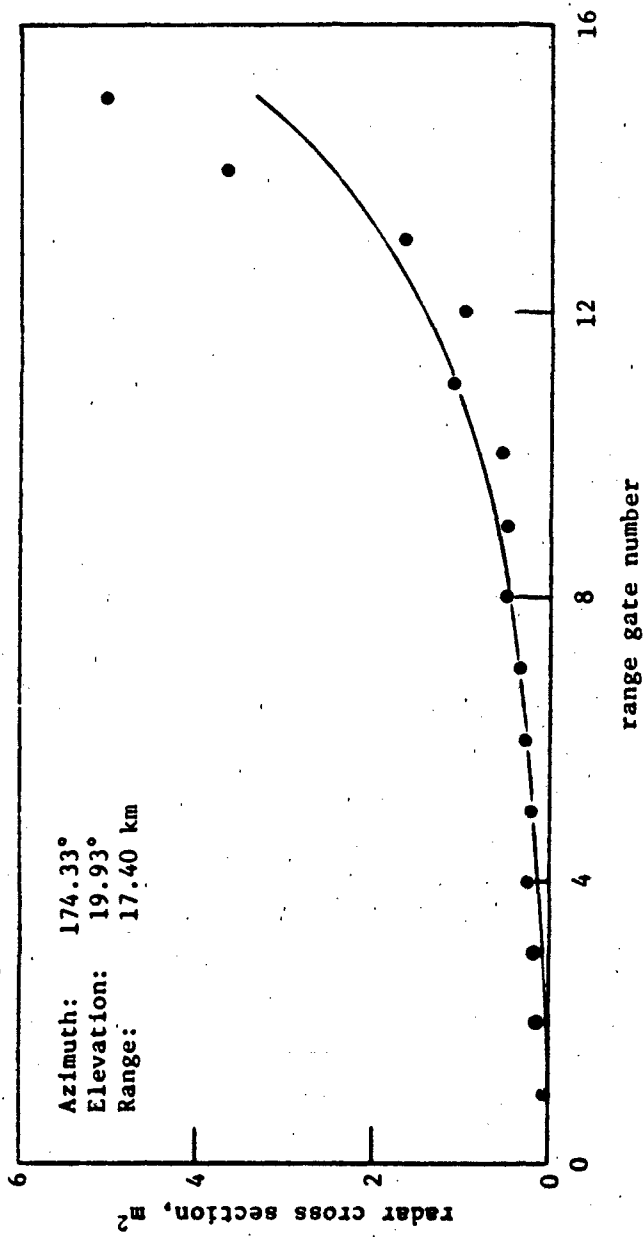
Figure 39. Distribution of radar return in range for records 417-420.

93
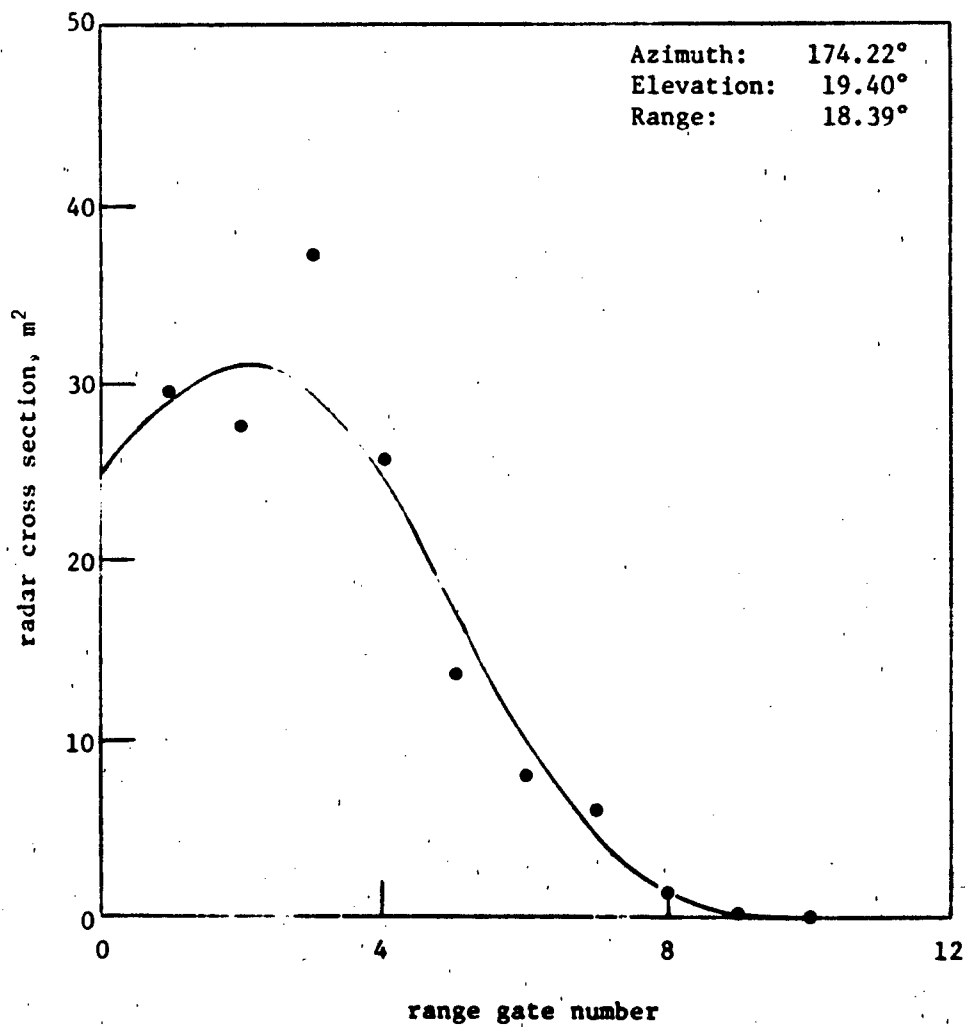
Figure 40. Distribution of radar return in range for records 516-519.
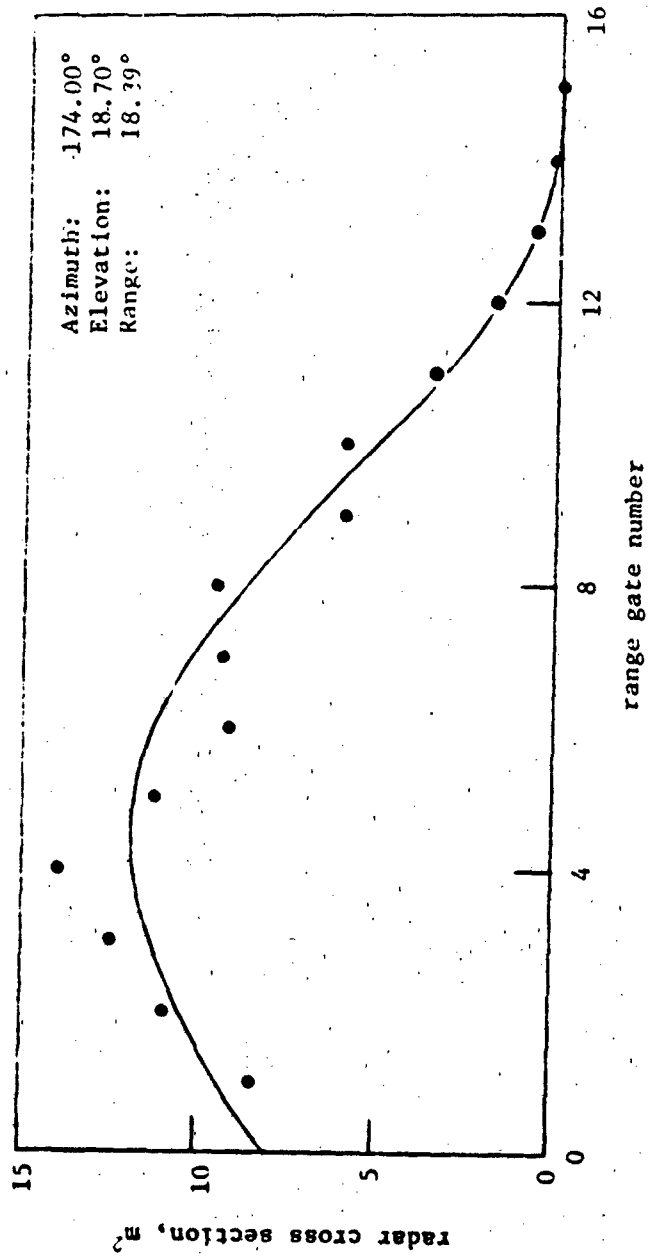
Figure 41. Distribution of radar return in range for records 599-601.

400 ns, hence the plots are of the radar return over successive 60-meter intervals. Except for Figure 40 whose total width is 0.72 km, the total width of each figure is 0.96 km.

Like the azimuth distributions, the distributions in range have a negative skew. Figure 39 is an exceptional case, showing only the tail of the distribution; for this one data set, a simple exponential function was assumed to be a representative fit. The results of the range dependent analysis is summarized in Table 10. The summary shows that the data are quite well fitted, with the largest error being only 9.2 m and the smallest coefficient of determination being 0.93. The skewness varies from small values (k = 6.0, m = 3.9) to large (k = 1.0, m = 0.63), depending on which particular data set one examines.

TABLE 10. SUMMARY OF STATISTICAL DATA FOR THE RANGE VARIATIONS

Figure	37	38	39	40	41
Azimuth angle	163.37	172.90	174.33	174.24	174.00
Elevation angle	18.93	19.13	19.93	19.40	18.70
Range, km	18.54	17.40	17.40	18.39	18.39
R_1^2	0.930	0.977	0.930	0.990	0.991
RMS error, m	9.2	1.6	0.6	3.8	1.2
% error	34	17	31	18	14
R_2^2	0.971	0.947	–	0.990	0.993
RMS error, m	6.8	3.1	–	3.3	1.0
% error	25	33	–	16	12
k	6.0	2.5	1.0	5.4	4.0
m	3.9	0.6	–	2.3	1.7

Most of range, azimuth, and elevation distributions shown in Figures 28 through 41 are approximated better by the skewed

normal distribution than the skewed exponential distribution. The exponential dependence on the square of the independent variable in Equation (73) suggests that the Gaussian (normal) distribution assumed for the chaff cloud represents a natural choice, although we must admit that the cause of the skewness in the measured data is unknown. If the distributions of chaff particles in time and space are to be more deeply explored, experiments need to be devised in which cloud mapping is the prime objective of the test, in contrast to the kind of data analyzed here.

SECTION 7
CHAFF CLUTTER POWER IN PROCESSORS

In general, the processed signal at the radar output caused by chaff scattered returns is a function of the chaff parameters (size, orientation, spatial distribution, velocity distribution), the radar parameters (transmitted power, antenna gain, polarization and pattern) and the radar processor (simple pulse, pulse width with MTI, pulse Doppler, or CW). This section is concerned with developing mathematical expressions for generic radar processors used to process the received power from dynamic chaff clouds. It is assumed that the relative positions and velocities of the chaff dipoles with respect to the subject radar are available from other analyses as given in earlier sections.

7.1 NONCOHERENT PULSE RADAR

Perhaps the simplest radar processor is that associated with a noncoherent pulse radar. In this case, the processor consists of a filter matched to the transmitted pulse and followed by an envelope detector. The processed signal as a function of time has a complex envelope $\tilde{Z}(t)$ and an amplitude envelope $Z(t)$ given by

$$Z(t) = \left| \sum_i a_i(\tau_i, \omega_i) \, e^{j\Psi_i} \, e^{j\omega_i t} \, p(t - \tau_i) \right| = |\tilde{Z}(t)| \qquad (76)$$

where $p(t)$ is the normalized processed pulse, τ_i is the time delay of the ith scatterer (chaff dipole), ω_i is the radian Doppler frequency of the ith scatterer, Ψ_i is the phase shift (reflection and delay components), and a_i is the amplitude of the return for the ith scatterer, which can be expressed as

$$a_i = \left[\frac{P_t G^2(\alpha_i, \epsilon_i) \ \lambda^2 \ \sigma_i}{(4\pi)^3 \ R_i^4 \ L_c} \right]^{1/2} \tag{77}$$

In Equation (77), P_t is the radar transmitted power, $G(\alpha_i, \epsilon_i)$ is the one-way power gain of the antenna as a function of the off boresight angles α_i and ϵ_i, λ is the wavelength, σ_i is the instantaneous RCS of the ith scatterer, R_i is the slant range between the radar and the ith scatterer, and L_c denotes the clutter processing loss.

At any instant $\tau_o = 2R_o/c$ of time delay corresponding to range R_o, the instantaneous amplitude of the return signal from Equation (76) is

$$Z(\tau_o) = \left| \sum_i a_i(\tau_i, \omega_i) \ e^{j\Psi_i} \ e^{j\omega_i \tau_o} \ p(\tau_o - \tau_i) \right| \tag{78}$$

and the instantaneous clutter power is

$$P(\tau_o) = Z^2(\tau_o) \tag{79}$$

For the case of a simple pulse, the radar has no Doppler frequency resolution and the summation is taken over the range resolution cell centered at $\tau_o = 2R_o/c$.

The random variable $Z(\tau_o)$ is generally treated as having a Rayleigh density function which results in an exponential density for $P(\tau_o)$. The average instantaneous clutter power is defined as the expected value of $P(\tau_o)$. If the phase angles Ψ_i are treated as independent random variables uniformly distributed over the interval $(0, 2\pi)$, then the average instantaneous power of the chaff return is

$$C = \overline{P(\tau_0)} = E[Z^2(\tau_0)] = \sum_i a_i^2 \, p^2(\tau_0 - \tau_i) \tag{80}$$

where a_i is the instantaneous amplitude of the ith scatterer as given by Equation (77) and $\rho(\tau_0)$ is the processed pulse shape normalized to a maximum of unity. If the scatterers are sufficiently dense, then the summation can be replaced by the integral $\int \rho(\tau) \, p^2(\tau_0 - \tau) \, d\tau$.

In the chaff clutter program, separate subroutines are used for computing the instantaneous positions and radar cross sections of the dipoles. Radar reference coordinate systems such as those shown in Figures 42 and 43 are required to compute the line of sight angles from radar to the various scatterers (used in the calculations of ω_i and σ_i) and the off-boresight antenna angles of the scatterers $(\alpha_i, \varepsilon_i)$ used in the antenna pattern functions. Figure 42 shows the relationship between the antenna coordinates (x', y', z') and the reference coordinates (x, y, z) for a ground-fixed system. Here ϕ_0 and θ_0 are the azimuth and elevation angles of the antenna boresight direction and it is assumed that the antenna lies in the (x', y') plane. The coordinate transformation equations are

$$x' = x \cos\phi_0 - z \sin\phi_0$$

$$y' = -x \sin\phi_0 \sin\theta_0 + y \cos\theta_0 - z \cos\phi_0 \sin\theta_0 \tag{81}$$

$$z' = x \sin\phi_0 \cos\theta_0 + y \sin\theta_0 + z \cos\phi_0 \cos\theta_0$$

From Figure 43, the off-boresight antenna angles in the horizontal and vertical planes can be determined as

100
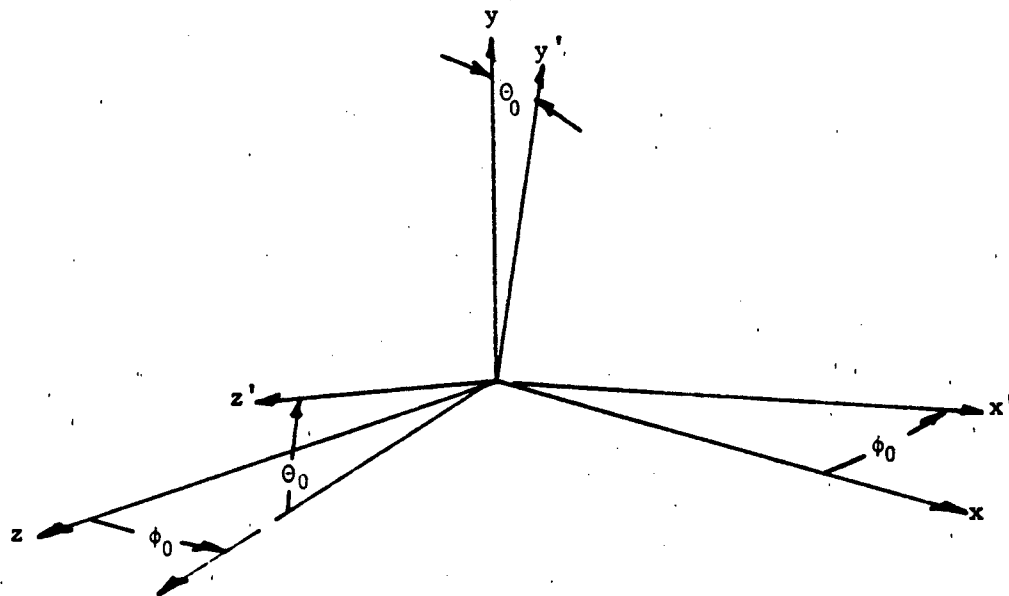
Figure 42. Earth cartesian coordinates (s, y, z)
and antenna coordinates (x', y', z').
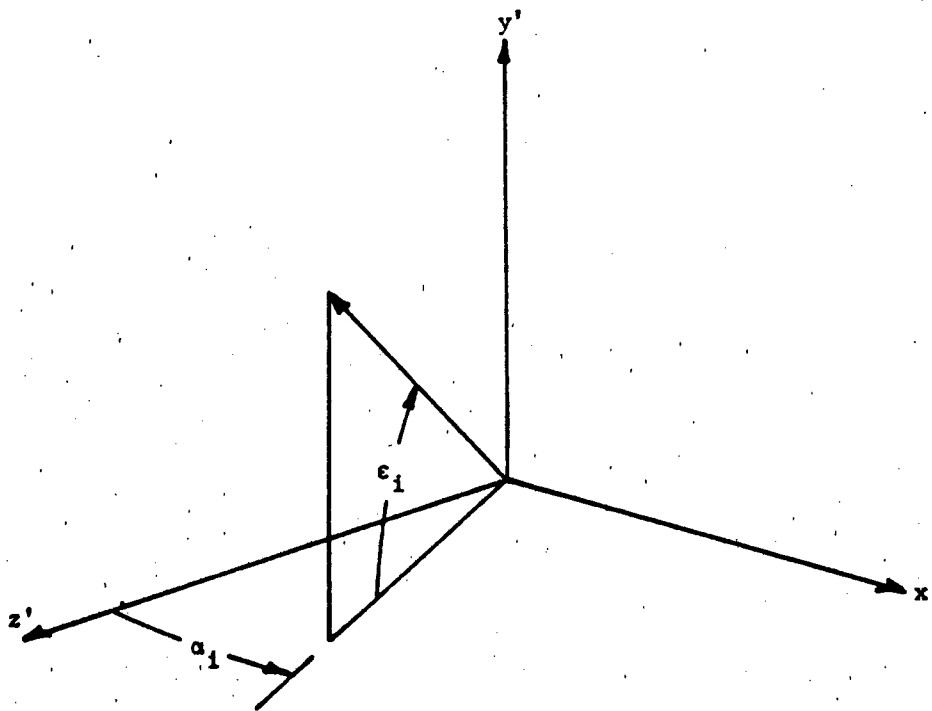
Figure 43. Antenna off-boresight angles α_1 and ε_1.

101

$$\varepsilon_i = \tan^{-1} \frac{y_i{}'}{\left(x'{}_i{}^2 + z'{}_i\right)^{1/2}}$$

$$\alpha_i = \tan^{-1} \frac{x_i{}'}{z_i{}'} \tag{82}$$

The exact computation of the average single pulse clutter power for the noncoherent pulse case requires accurate mathematical representations of the antenna gain function $G(\alpha,\phi)$ and the pulse weighting function $p(\tau)$. In many cases, this functional information is not available and various standard mathematical representations must be used (such as $\sin x/x$, Taylor, Gaussian, and Chebyshev antenna patterns, Gaussian and rectangular pulse shapes). When $G(\alpha,\varepsilon)$ and $p(\tau)$ are known accurately, the computation of Equation (80) may require excessive computer resources for detailed functions and a large number of chaff particles. Thus, relatively simple approximations of the known or postulated antenna pattern and pulse weighting are useful in obtaining first order estimates of of the received clutter power. Given the uncertainties in radar cross section and relative position and velocity of the scatterers, simple approximations for $G(\alpha,\varepsilon)$ and $p(\tau)$ appear to be adequate if chosen judiciously.

Perhaps the simplest approximation of the antenna patterns in α and ε is the rectangular function shown in Figure 44. In this case, the gain function is represented as: $G(\alpha,\varepsilon) = G_O$ for $-\Delta\varepsilon/2 < \varepsilon < \Delta\varepsilon/2$ and $-\Delta\alpha/2 \le \alpha \le \Delta\alpha/2$, and zero otherwise, where G_O is the average gain and $\Delta\varepsilon$ and $\Delta\alpha$ are the equivalent beamwidths in the two orthogonal planes. If the processed pulse is also assumed to be rectangular, then the processed clutter power can be approximated as

$$C = \overline{P(\tau_O)} = \frac{P_t \, G_O{}^2 \, \lambda^2}{(4\pi)^3 \cdot R_O{}^4 L_c} \sum_i \sigma_i \tag{83}$$

where the summation is taken over all scatterers within the range resolution cell and the ε and α beamwidths. This formulation
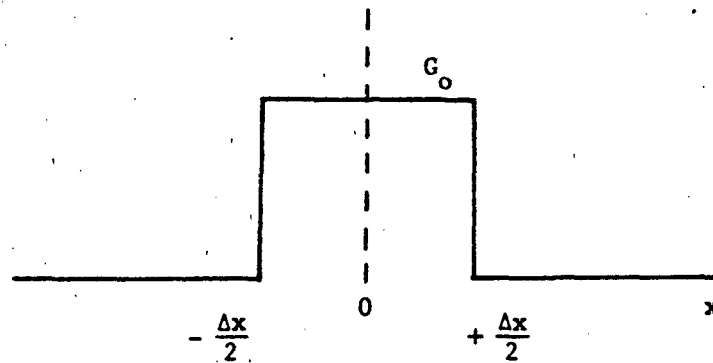
Figure 44. First order approximation of antenna pattern.
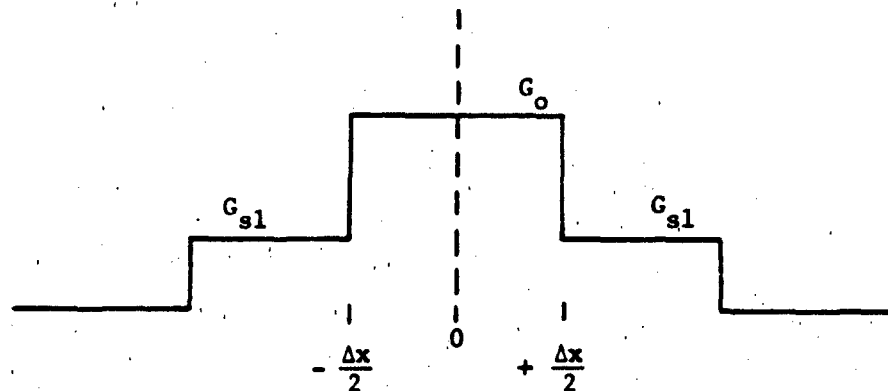
Figure 45. Antenna pattern approximation including sidelobes.

requires a search of the scatterer coordinates to determine those scatterers which are positioned within the appropriate angle and range intervals, a calculation of the RCS of the subject scatterers, a summation of the RCS values, and multiplication by a constant.

If better accuracy requires that the effects of antenna sidelobes be included in the average power computations, then the approximation shown in Figure 45 may be employed. Here G_O is the average main beam antenna gain and $G_{s\ell}$ is the average sidelobe level. For this case, the average chaff clutter return at the range R_O is

$$C = \overline{P(\tau_o)} = \frac{P_t \lambda^2}{(4\pi)^3 R_o^4 L_c} [G_O^2 \sum_i \sigma_i + G_{s\ell}^2 \sum_j \sigma_j] \qquad (84)$$

where the summation i is over the scatterers in the main beam and the summation j is over the scatterers in the sidelobes.

7.2 COHERENT MTI

Pulse radars are frequently equipped with MTI signal processors to reduce the undesired returns from scatterers such as ground, rain, and chaff clutter. The radar must be phase coherent on a pulse to pulse basis, either through the use of a coherent transmitter or by phase locking the receiver to the transmitted pulse. In either case, the MTI processor acts as a periodic narrow band notch filter or a wide bandpass filter, centered at zero Doppler frequency with a period equal to the PRF. If the clutter return has a non-zero center Doppler frequency, it must be shifted to zero before MTI processing is performed, either by manual or automatic frequency tracking. This is required to center the undesired returns in the filter stop band.

MTI filters introduce a weighting of the scatterer return as a function of its doppler frequency. The average clutter power received at the delay time τ_o corresponding to range R_O from the

chaff scatterer, in this case can be written as

$$C = \overline{P(\tau_0)} = \sum_i a_i^2 \, |H(\omega_i)|^2 \, p^2(\tau_0 - \tau_i) \tag{85}$$

where a_i is given by Equation (77), $\rho(\tau_0)$ is the normalized processed pulse and $H(\omega_i)$ is the frequency response of the filter. The Doppler frequency of the scatterer is

$$w_i = -(2\pi) \, \frac{2f_0}{c} \, (\overline{V}_i - \overline{V}_r) \cdot \overline{a}_{ri} \tag{86}$$

where f_0 is radar frequency, c is the speed of light, $\overline{V}_i$ is the scatterer velocity, $\overline{V}_r$ is the radar velocity, and $\overline{a}_{ri}$ is the unit vector from the radar to the ith scatterer.

Various types of MTI filters are possible. They may be analog or digital, with or without feedback paths. The simplest analog form has the functional representation:

$$|H(\omega)|^2 = (2)^{2n} \, (\sin \omega T/2)^{2n} \tag{87}$$

where T is the pulse period and n is the order of the canceller (n = 1 for a single delay canceller, n = 2 for a double delay canceller, etc.). If Equation (77) is used to compute the average clutter power, then the approximations discussed in Section 7.1 for the pulse shape p(τ) and antenna gain function G(α,ϵ) may be used. The calculations for the MTI case require the additional computation of H(ω) and the weighting $|H(\omega)|^2$ of the chaff scatterers. If the scatterers are sufficiently dense in range and Doppler, then the average clutter power as given by Equation (85) can be approximated by the double integral

$$C = \overline{P(\tau_0)} \cong \int \rho_1(\tau) \, p^2(\tau_0 - \tau) d\tau \int \rho_2(\omega) |H(\omega)|^2 \, dw \tag{88}$$

where $\rho_1(\tau)$ the clutter power density in delay (range) and $\rho_2(\omega)$

is the clutter power density in Doppler. Before one can use Equation (88), the densities $\rho_1(\tau)$ and $\rho_2(\omega)$ must be calculated from other subroutines based on the relative position and Doppler frequencies of the scatterers.

7.3 CW DOPPLER RADARS

Another general class of radars is known as CW Doppler radars. These radars transmit a continuous narrow band signal and resolve targets in angle and Doppler frequency. A true CW Doppler radar has no range resolution, because scatterers at all ranges in the antenna main beam and possibly the antenna side-lobes contribute to the return received at a given time. Through the use of signal modulation, for example, frequency modulation, a limited amount of range resolution may be achieved. Two antennas are generally required for signal isolation in CW systems.

For the CW radar with no intentional modulation, the average power return from a set of scatterers can be described by the equation

$$\overline{C} = \sum_i \frac{P_a G^2(\beta_i, \epsilon_i) \, \lambda^2 \, \sigma(\omega i)}{(4\pi)^3 R_i^4 \, L_c} \, |H_c(\omega_i - \omega_c)|^2 \qquad (89)$$

where P_a is the average radar transmitter power and G, λ, σ, R_i, and L_c are as defined in Equation (77). The quantity $H_c(\omega)$ is the frequency response of the Doppler filter normalized to a maximum of unity, ω_c is the center frequency of the filter, and ω_i is the Doppler frequency of the scatterer as given by Equation (86).

If all the scatterers lie in the main beam of the antenna, then a suitable approximation would be to weight the scatterers by an average gain G_0 as discussed in Section 7.1. When a sig-nificant number of scatterers appear in the sidelobes, then the antenna gain function shown in Figure 45 would provide a simple weighting. If the scatterers are spaced sufficiently close in

range so that R_i is approximately the same for all scatterers, then a constant range R_o can be used in (89).

The Doppler filter function $H_c(\omega)$ ideally should be the measured frequency response of the filter. When measured data are not availble, the filter design characteristic (such as Bessel, Chebyshev, etc.) would be applicable. If it is desired to minimize the computations associated with the filter weighting, then a Gaussian filter or other approximation similar to those in Figures 44 and 45 for the antenna patterns could be used.

7.4 PULSE DOPPLER RADARS

Pulse Doppler (PD) radars combine the features of simple pulse and CW radars to obtain resolution in range and Doppler. The transmitted waveform is a periodic series of pulses which are phase coherent on a pulse-to-pulse basis. Processing is accomplished with a comb filter matched to the pulse train or matched to a single line of the spectrum through the use of range gates and a Doppler filter bank. Processing is simplified in the case of high PRF (approximately 50% duty cycle) pulse Doppler radars because only a single range gate is required. Clutter computations are complicated by the presence of range ambiguities due to multiple time around returns in high PRF PD radars, and by Doppler ambiguities due to returns from scatterers whose Doppler frequency differs by multiples of the PRF from the center frequency of the Doppler filter in low PRF PD radars.

The general form for the average backscattered power for a set of discrete scatterers illuminated by a PD radar is

$$\overline{C} = \overline{P(\tau_o)} = \sum_i a_i^2 \left| X(\tau_o - \tau_i, \Delta\omega_i) \right|^2 \tag{90}$$

where the amplitude of the individual scatterers a_i is given by Equation (77) and $X(\tau, \omega)$ is the ambiguity function of the processed signal evaluated at the delay offset $\Delta\tau_i = \tau_o - \tau_i$ and

107

Doppler offset $\Delta\omega_i$. The ambiguity function is defined as the response of the processor to a signal offset in Doppler from the center frequency of the processor and is given by the equation

$$x(t,\Delta\omega) = \frac{1}{2\pi} \int_{-\infty}^{\infty} \tilde{F}(\omega - \Delta\omega_i) H(\omega) e^{j\omega t} d\omega \qquad (91)$$

where $\tilde{F}(\omega)$ is the voltage spectrum of the complex signal and $H(\omega)$ is the frequency response of the filter.

For an unweighted pulse train in which there is no pulse-to-pulse modulation, the signal spectrum for N pulses is

$$\tilde{F}(\omega) = \delta \frac{\sin(\omega\delta/2)}{\omega\delta/2} \cdot \frac{\sin(N\omega T/2)}{N\omega T/2} \qquad (92)$$

where δ is the individual pulse width and T is the period of the pulses. Note that NT is the total duration of the processed signal. The function $\tilde{F}(\omega)$ is sketched in Figure 46 for a typical case; it is characterized by a sequence of strong lobes of magnitude $N\delta$ and width 1/NT, spaced apart by the pulse repetition period 1/T. Between these strong lines, the spectrum is weak and the variation is rapid due to the $\sin(N\omega T/2)$ term. Not shown in the sketch is the slow variation due to the $\sin(\omega\delta/2)$ term.

If the filter function $H(\omega)$ is assumed to be an ideal band-pass filter with a bandwidth B = 1/NT, then $X(t,\Delta\omega)$ as given by Equation (91) can be approximated by

$$X(t,\Delta\omega) = \frac{\delta}{NT} \frac{\sin(N\Delta\omega T/2)}{N\Delta\omega T/2} \qquad (93)$$

for scatterers located in the range gate of width δ centered at delay $\tau_0 = 2R_0/c$, or delays τ_0 plus multiples of T when range ambiguities are present. The number of range ambiguities for high PRF Doppler radars is given by the relationship

$$N_a = 2(R_{max} - R_{min})/cT \qquad (94)$$
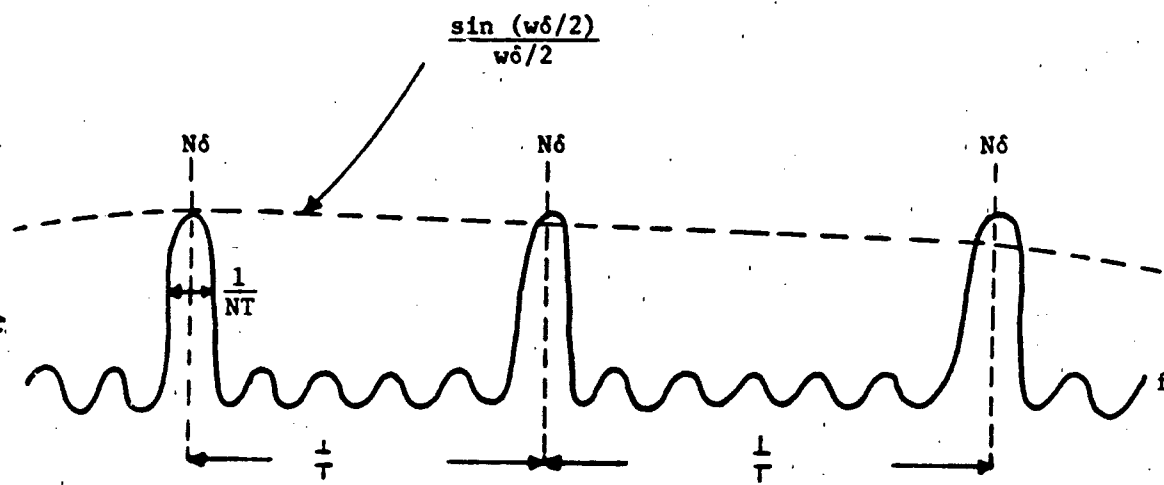
Figure 46. Spectrum of the transmitted signal.

where R_{max} and R_{min} are the maximum and minimum ranges to the scatterer cloud and T is the pulse period of the radar.

If the approximations in the previous paragraph are used in Equation (90), the average clutter power at range delay τ_0 becomes

$$C = \sum_i a_i^2 N_a \frac{\delta}{NT} \left[\frac{\sin(N\Delta\omega_i T/2)}{N\Delta\omega_i T/2} \right]^2 \qquad (95)$$

where $\Delta\omega_i$ is the relative Doppler frequency of the ith scatterer with respect to the center frequency of a particular Doppler filter. If the spread in the Doppler frequencies of the scatterers is small, then it may be possible to replace $\Delta\omega_i$ by $\Delta\omega_{ic}$ for all scatterers, where $\Delta\omega_{ic}$ is the center Doppler frequency of the Doppler spread of the scatterers.

In calculating the average processed clutter from Equation (95), the radar parameters N (number of pulse integrated), T (the radar pulse period), and δ (radar pulse length) are required. The quantity $\Delta\omega_i$ is calculated by assuming the center frequency of the Doppler filter is known. For example, it may be the Doppler frequency of a target or the center Doppler frequency of the chaff. Then it may be offset from the computed scatterer Doppler frequencies ω_i. Equation (94) is used to compute the number of range ambiguities. For the computation of a_i^2 (see Equation (77)), the radar parameters corresponding to peak power P_t, antenna gain pattern $G(\alpha, \epsilon)$, radar wavelength λ, and loss function L_c are required. The radar-to-scatterer slant range R_i and scatterer RCS σ_i are computed in other subroutines. The approximate antenna patterns shown in Figures 44 and 45 may be employed to minimize the computations.

SECTION 8
SUMMARY AND CONCLUSIONS

This report summarizes the work performed on two phases of what was to have been a four-phase program. The principal effort has been to assemble the components of a chaff modeling program, but not all the elements have been completed. The approach has been to characterize the scintillation of the return from a chaff cloud by the modeling of a relatively small number of dipoles, under the assumption that this small number (up to about 1000, and even 1000 dipoles is probably many times more than actually needed) adequately simulates the scintillation due to all dipoles in the cloud.

The electromagnetic scattering from a single dipole and the motion histories of many dipoles are used to generate the scintillation spectrum. Our studies suggest that the total spectrum is less than 150 Hz wide. This part of the model provides only the time varying signals, and the amplitudes are normalized with respect to a single dipole. To scale the amplitude upward to correspond with the contributions of thousands of dipoles within a given range cell, we postulated a dipole concentration function having a bivariate Gaussian distribution in a plane transverse to the plume axis.

This amplitude depends on the product of the antenna radiation pattern and the dipole concentration within a spherical shell of constant radius. Since both functions vary within the shell, an integration is implied. However, the integral cannot be evaluated analytically unless restrictive conditions in symmetry are imposed. And even though numerical integration can indeed be performed, the computer running time for such schemes may discourage the use of the algorithm for routine evaluation of tactical scenarios. Thus, the model in its current configuration is better suited for diagnostic purposes.

An analysis of the results of a single chaff test suggests that the Gaussian distribution is a reasonable approximation of the transverse dipole concentration. The analysis showed that although the density distributions are skewed, they are described better by a skewed normal distribution than by a skewed exponential distribution. Unfortunately, cloud mapping was not the primary objective of the test and the number of segments in the data records useful for analysis was few.

The electromagnetic features of chaff cloud scattering are much easier to account for than the motion of the chaff particles and their distributions in space. The effects of local turbulence were accounted for by the use of a specific turbulence profile. Such profiles change from day to day, season to season and place to place. Hence it is impractical to attempt to generate more general models.

As it stands, the chaff model requires a great deal of computer time to trace the motion histories of even a small collection of dipoles and to carry out the numerical integration of a postulated dipole distribution. Hence, the model may consume large amounts of computer resources for evaluating specific tactical scenarios. The model is incomplete because the radar receiver module originally contemplated was not constructed. However, a study of four classes of receiver processors was undertaken to define the features that need to be included in such a module.

As for future requirements, a receive module should be constructed and techniques should be investigated for reducing the running time. It would be helpful to devise empirical descriptions of the dipole concentration levels based on measured data.

SECTION 9
REFERENCES

1. D-C. Kuo and B. J. Strait, "Improved Programs for Analysis of Radiation and Scattering by Configurations of Arbitrarily Bent Thin Wires," Report No. AFCRL-72-00051, Syracuse University, 15 January 1972.

2. R. M. Traci, G. T. Phillips, P. C. Patniak and P. T. Harsha, "Chaff Dispersion Analysis: Preliminary and Scoping Studies," Report No. SAI 093-81-069LJ, Science Applications, Incorporated, La Jolla, CA, January 1981.

3. R. L. Bogusch, M. R. Frolli, F. W. Guigliano, S. L. Gutsche and B. E. Sawyer, "A Simulation of a Chaff/Aircraft/Radar Encounter (SCARE)," Report No. AFAL-TR-77-270, Mission Research Corporation, Santa Barbara, CA, December 1977.

4. J. Brunk, D. Mihora and P. Jaffe, "Chaff Aerodynamics," Report AFAL-TR-75-81, Alpha Research Incorporated, November 1975 (AD 019 525).

5. Mark D. Tew, "Correction to WIRES Program," IEEE Transactions on Antennas and Propagation, Vol. AP-23, May 1975, pp. 450-451.

6. Roger F. Harrington, Field Computation by Moment Methods, The Macmillan Company, New York, 1968.

7. S. Chang and V. V. Liepa, "Measured Backscattering Cross Section of Thin Wires," University of Michigan, Radiation Laboratory Report 8077-4-T, May 1967.

8. S. L. Borison, "Bistatic Scattering Cross Section of a Randomly Oriented Dipole," IEEE Transactions on Antennas and Propagation, Vol. AP-15, March 1967, pp. 320-321.

9. M. Abramowitz and I. A. Stegun (editors), Handbook of Mathematical Functions, Dover Publications, Inc., New York, 1970, p. 130.

10. M. Nakagami, "The m Distribution – A General Formula of Intensity Distribution of Rapid Fading," in Statistical Methods in Radio Wave Propagation, W. C. Hoffman (editor), Pergammon Press, New York, 1960.